THE UNIVERSITY *of* EDINBURGH

Using DEM-CFD method at colloidal scale

Florian Chaumeil

Institute for Infrastructure and Environment
School of Engineering and Electronics

Thesis submitted for the degree of Doctor of Philosophy
The University of Edinburgh
2013

ABSTRACT

The aim of this work is to look into the applicability of Discrete Element Modelling (DEM) coupled to Computational Fluid Dynamics (CFD) to simulate micro-scale colloidal particles immersed in fluid. Numerical methods were implemented through the commercial framework of EDEM2.3.

As opposed to dissolved matter, which behaves as a continuum within the fluid medium, particulate matter is made of discrete entities that interact amongst themselves, and with the fluid and any physical boundaries. Particulate matter is ubiquitous in many purification processes that would beneficiate from having an easy way to model particle dynamics immersed in water. In an effort to understand better the dynamics of particle deposition under surface forces and hydraulic forces, a micro-scale numerical model was built adopting both a mechanistic and a statistical approach to represent the forces involved in colloidal suspension. The primary aim of the model was to simulate particle aggregation, deposition and cluster re-suspension in real world micro-systems. Case studies include colloidal flocculation in a constricted tube, and colloidal fouling around membrane filtration feed spacers.

This work used a DEM-CFD coupling method that combined the DEM particle flow simulation with hydrodynamics forces from a velocity field computed through CFD. It also implemented boundary-particle and particle-particle interactions by enabling the modelling of surface and interfacial forces. Two kinds of coupling method were considered: two-way and one-way coupling. Two-way coupling is suitable for high particle concentration flow where particle loading affects the hydrodynamics. One-way coupling is suitable for dispersed particle configuration where the flow field is assumed to be undisturbed by the particles. The advantages and drawbacks of both techniques for micron-size particles were investigated.

EDEM 2.3 was customised with plug-ins to implement Van der Waals forces and Brownian forces and its post-processing features offered the ability to investigate easily the micro-particles behaviour under the influence of fluid forces. In this context, DEM-CFD modelling using EDEM 2.3 represents an improvement on previously published works as it enables higher visibility and reproducibility along with increasing the number of potential users of such modelling.

Emphasis was given in presenting original findings and validation results that illustrate DEM-CFD applicability, with respect to modelling of hydraulically mediated colloidal surface

interaction; while highlighting factors that limit the ability of the technique. For instance, the effect of particle disturbance on the surrounding medium currently proves difficult to model.

Keyword: Discrete Element Method, DEM, colloid, agglomeration, deposition

DECLARATION

This thesis and the work described within have been conducted solely by Florian Chaumeil under the supervision of Dr Martin Crapper at the Institute for Infrastructure and Environment in the School of Engineering of the University of Edinburgh. Where others have contributed or other sources are quoted, references are given in full. The work has not been submitted for any other degree or professional qualification.

Florian Chaumeil

Edinburgh, July 2013

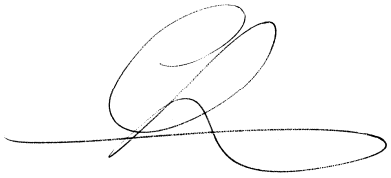

ACKNOWLEDGEMENTS

I wish to thank my supervisor Dr Martin Crapper, for his unerring support, patience and his constant encouragements.

I also wish to thank the people whose technical assistance made this work possible, the IT team of the School of Engineering and the support team from DEM Solutions Ltd.

Above all, I would like to thank my parents for believing in me and always striving to make my life as easy as possible.

TABLE OF CONTENTS

NOMENCLATURE

Roman characters

A	Areas
C_0	Particle concentration
C_C	Cunningham factor
C_D	Drag coefficient
E	Young's modulus
F	Force
k_B	Boltzmann constant
H	Hamaker constant
M	Mass
Re	Reynolds number
T	Temperature
u	Relative displacement
U	Fluid local velocity
v	Relative velocities
$\vec{v}$	Fluid velocity vector
V	Particle velocity

Greek characters

α	Local volume fraction
γ	Damping coefficient
Γ_{in}	Particle creation rate
δ_{ki}	Comparison function
κ_n and κ_t	Normal and tangential stiffness
λ	Characteristic wave length
μ	Water dynamic viscosity
ν	Kinematic viscosity
ξ	Friction coefficient
ρ	Mass density
τ_{ki}	Viscous stress tensor components

CHAPTER 1: Introduction

1. 1 Motivation

This work is a simulation study that consists of using and expanding on a state-of-the-art multiphase simulation method, Discrete Element Method – Computational Fluid Dynamics (DEM-CFD) coupling, to implement numerically theoretical models previously developed. Applying this technique to micron scale particle modelling is a novel and interesting approach from a modelling point of view. The coupling of the two methods represents an improved way of modelling suspensions flowing in complex in geometries. Such a technique has never been implemented as part of the framework of any commercial simulation software, and reported work very often involves "in-house" computational codes, which are only used and often only understood by their authors. Therefore, the implementation of a similar numerical technique can vary a great deal between research groups. However, with ever-increasing technological ability and computational power made accessible more and more easily, DEM's resource intensive way of simulating large numbers of interacting particles is becoming less and less problematic, and the technique is likely to become more widely used, which demands a more unified implementation method. At the same time, the potential of DEM-CFD to model accurately particle-fluid interaction as well as particle-boundary interaction and particle-particle interaction increases, and coupling opportunities of DEM techniques with third party methods is also likely to multiply. Commercial codes such as EDEM 2.3 offer the advantages to provide novice DEM users with an intuitive user interface, flexible and customisable capabilities through the Application Programming Interface (API) and direct technical support, which is very useful for practical implementation. This facilitates spending less time on the secondary issue of knowing "how to" use the code and spending more time on "using and customising" it.

This thesis aims to investigate the use of DEM-CFD for simulating and understanding the accumulation and re-suspension dynamics of colloidal particles. The commercial simulation software EDEM 2.3 was used along with customised physical models to simulate floc and aggregate formation at micron scale and to model deposition dynamics and structure.

This first chapter will demonstrate the relevance of particle simulation at colloidal scale.

1. 2 Colloidal scale particle simulations

1. 2. 1 What are colloids?

Colloids are the smallest finite particle before molecular scale matter and are to that regard at the interface of molecular forces and mechanistic forces [1]. They are very useful to understand and directly observe phenomena related to thermodynamics [2] but they are more commonly known and used for their rheological properties in paints, ink, cosmetics (cream and gels) or more inconspicuously in everyone's life in dairy, mud and syrups. Even blood is considered as a colloidal suspension.

1. 2. 2 Significance of colloids in water treatment

In aquatic systems macromolecules and colloids including microorganisms, are ubiquitous and include toxic compounds that might be harmful to human health. Colloids are associated with a wide range of different environmental topics. However, they have in common phenomena like coagulation and adsorption, which lead to flocculation and deposition. For instance, porous media and membranes are widely used in the separation of these macromolecules and colloids in water treatments (Figure 1.1).

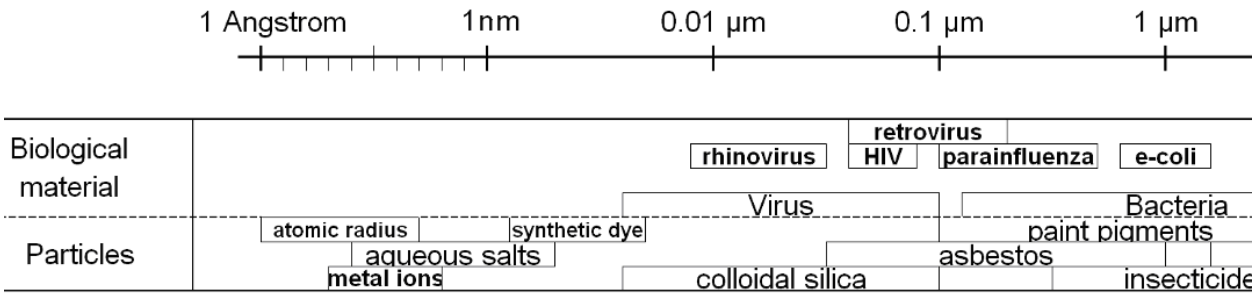

Figure 1.1: relative size of sub-micron and micron scale particles [3]

However, filtration is subject to flux decline [4], which results from pore blocking, adsorption, concentration polarization and cake formation due to the deposition of non-dissolved particles, which is the precipitation of organic matter past the solubility threshold concentration. Therefore, understanding the dynamics of non-dissolved material at the particle level is crucial in getting rid or taking advantage of them, and this has been driving research for decades.

Granular filtration represents a relatively inexpensive separation method for particulate matter removal. Typical particulates in water include clay and silt particles, microorganisms

(bacteria, viruses and protozoa), colloidal and precipitated organic substances [5]. However, granular media filter present different retention characteristics as a function of grain size, surface roughness, shape, density, media porosity, and particle retention at grain scale is still an ongoing subject of research [6, 7].

1. 2. 3 Colloidal physics

For colloidal suspensions, surface interactions, such as attractive and electrostatic interactions, play a very important role in aggregation mechanisms, leading to different deposition and re-suspension behaviours. The accumulation of colloidal particles also depends on particle size, thermodynamic effects and solute chemistry, as defined in the DLVO theory. The original DLVO theory was developed in the 40s by two independent groups: Derjaguin and Landau in the Soviet Union and Verwey and Overbeek in the Netherlands.

Verwey and Overbeek defined colloid science as [8]:
"The study of systems containing kinetic units which are large in comparison with atomic dimensions. Such systems may be particle free to move in all direction, or they may be derived system where the particles have lost their mobility but maintained their individuality (as a coagulum, a gel, etc). It is customary to distinguish two classes of colloids whose behaviour is entirely different. They are called Lyophobic and Lyophilic. Colloids of the second kind have a strong affinity with the molecules of the dispersion medium, while lyophobic colloids have a weak or no affinity"

The kinetic units in lyophobic colloids are rigid particles or small liquid droplets. Lyophilic colloids consist in single large molecule, or clusters of such molecules, for instance gelatine sol, and are subject to solvation (Hydration when solvent is water).

A typical colloidal system shows a large surface-to-volume ratio, whether it is an emulsion or a micellar solution. For that reason, colloidal suspensions are extensively used in pharmacological and cosmetic industry. The rheological properties of certain colloidal system and emulsions are also beneficial for countless applications in food industries.

DLVO theory states that the stability of charged colloidal systems is governed by competition between the London-Van der Waals forces of attraction and the electrostatic double layer forces of repulsion. Both of these forces extend from a few tens of nanometres up to a few microns. They have well defined analytical forms over this separation range. At shorter inter-particle distances (<1 nm) a number of other forces come into play such as electron overlap repulsion (Born repulsion; Pauli exclusion) and a mechanistic approach is

no longer appropriate. The combined potential energy of London-Van der Waals (LVdW) interaction and the electrostatic double layer (EDL) interactions varies as a function of the particle-particle surface separation to give DLVO forces. They control the rate of flocculation and deposition. The DLVO potential curve can feature a primary minimum associated with coagulation, an energy barrier, and a secondary minimum associated with reversible flocculation, as will be discussed in Section 3. 7. In order to achieve virtually irreversible association, the energy barrier must be overcome by sufficient momentum gained from thermal or hydrodynamic forces. For systems that obey the DLVO model, the energy barrier can be removed by adding the right amount of electrolyte to neutralize surface charges. The interaction between the collection surface and colloidal solution also depends on the hydrodynamics of the flowing solution. Fluid/colloid interaction has been the subject of previous simulation and a fair amount of experimental and computational work has already been carried out and will be presented in the next section as a guide for the simulations presented here.

Given the particular physico-chemical characteristics of colloids, the central research questions in this work are:

1. How to implement colloidal interfacial physics in the scope of small scale DEM-CFD simulations?
2. What are the essential numerical and conceptual tools required to implement it?
3. What is the most efficient way to do so?

The next section reviews the past literature that helps partially answering these questions

1. 2. 4 Lessons, clues and warnings from previous work

There have been previous studies, experimental and numerical, relevant to this work that introduced different methods, simplifications and observations. They constitute a very helpful source of knowledge that indicates what could be simulated so far, how and under which limitations; this section describes what could be learned from them in order to address the research questions.

1. 2. 4. i Why particle-orientated modelling?

Continuum Modelling of meso-scale particles (i.e. a few millimetres diameter) immersed in a fluid has been successfully applied in various fields to give predictive results. They are useful in engineering process like fluidised bed [9] or pneumatic conveying [10], where dense particle concentration is involved. However, there are some engineering applications, like granular filtration, that involve very disperse particle phase, where the continuum approach fails to provide enough detail in order to achieve predictive simulation [6]. Very often, particle scale modelling is needed to understand the primary mechanisms involved in a bigger process and that ultimately explains a full-scale behaviour. In filtration applications for instance, the need for small scale modelling of particle deposition and cluster formation dynamics is highlighted by the fact that some phenomena occur at particle scale and therefore can only be explained and modelled through particle scale considerations such as particle-particle interaction, rolling effects, roughness, and particle size segregation. Collision or near-contact relative motion play a key role in particle deposition [11], and particle scale simulations are useful to understand or validate capture mechanisms.

Early theoretical studies of particle collectors used trajectory analysis where the trajectories of particles are estimated from knowledge of the various fluid forces acting on the particle [12, 13], sometimes including Brownian motion using a stochastic simulation [14]. These models assumed that particles stick upon contact on the obstacle or particle cluster. But while it is a reasonable assumption for sufficiently small adhesive particles, as enough particles aggregate, the fluid force on this cluster can eventually become large enough that the aggregate, or part of it breaks off and is advected downstream [15]. Some sort of particle scale modelling is then essential to go further than the stick-upon-contact assumption and take into account re-suspension. Numerical models based on critical deposition velocity were developed to deal with re-suspension separately [16], but mechanistic models that simulate aggregation and break off in the same computational frame would be an improvement.

Experimental observation [17] revealed that particle aggregates adhering to a cylinder for instance, grow to some critical size before experiencing bending, collapsing, or breaking off.

This effect causes the number of deposited particles to oscillate around a mean value after some time. These dynamic mechanisms show the limits of stick upon contact formulation, even when these are enhanced with side models. Particle scale approaches allow investigating the dynamic mechanisms that include cluster formation, re-suspension and breakage mechanisms. It is in many aspects, a more natural, and simpler method, even though more time consuming, it gives results more significant, as it numerically replicates tangible mechanistic interactions, and provides powerful and instinctive ways to post-process simulations.

1. 2. 4. ii What kind of particles?

In the vast range of different processes where particle transport is common, all types of particles can be found. They vary in size, shape, density and material. Most particulate fouling experiments use standard sub-micron or micron scale particles (yeast [18]; latex beads [19, 20], fat globules [21]) in order to investigate the deposition pattern of colloid suspensions as a function of diverse operating conditions (system chemistry [19], hydraulic state). The particles used in this thesis are idealised spherical latex particles, as they are commonly used as model particle in both experimental and simulation studies [6, 7, 16, 19, 22-24], that were used as comparison material.

1. 2. 4. iii Energy Barriers

Assuming a low volume fraction loading of particles, Johnson et al [25] studied the deposition and re-entrainment dynamics of biological (microbial) and non-biological colloids in porous granular media. The porous medium is idealized as a regular packing of spherical grains intended to be representative, for example, of sand filtration. Such a geometrical setup represents a simple porous medium as a volume filled with mono-size spherical beads. This condition does not match the reality of natural or industrial filtration processes, where beds are most likely to be made of randomly distributed non-spherical particles, but the relevance of such research comes from the fact that the vast majority of existing computational and experimental work has been performed in similarly simple porous media. The retention mechanisms are however expected to be the same in complex porous media having a larger distribution of grain and pore sizes, although new mechanisms may emerge due especially to grain surface heterogeneity [6]. Comparison with previously published results demonstrated that hydrodynamic drag mitigates deposition and drives re-entrainment of both biological and non-biological colloids (inert particles) in a similar way, which makes colloidal systems simulations relevant for engineer and microbiologist. Johnson [25] also indicates that even in the presence of an energy barrier to deposition, hydrodynamic drag may influence deposition and re-entrainment of colloids from surface. It was concluded that a colloid transport theory that explicitly accounts for the influence of the hydrodynamic field at the grain surface should be investigated. His results showed that

deposition is governed by fluid velocity, stagnation zones, wedging of colloids within grain-to-grain contacts and variation of ionic strength, but also surface heterogeneity.

Among a wealth of work on DLVO attraction profiles and complex interfacial interaction, Kuznar and Elimelech [19] aimed to provide insight into phenomena such as secondary minimum deposition of particles and microbial pathogens during physicochemical filtration. A flow-cell experiment where micrometer-sized particles flowed through a layer of packed glass beads was set up and the particle deposition observed in real time through a fluorescent microscope. At low ionic strengths (1–3 mMol/L or mM), no deposition was observed on the collector beads. As the monovalent salt concentration was raised to moderate ionic strengths (10–30 mM), the particles became trapped in the secondary minimum and translated along the glass bead surface, accumulating near the rear of the spherical collectors. At high ionic strength (100 mM), no electrostatic energy barrier to deposition exists and particles deposited over the entire surface of the spherical collector. In addition, it was also noted that the outer surface potential of colloids also vary according to Oshshima's theory with respect to ionic strength, which makes electrostatic interactions a complex multi-variable problem. The same team found deviations from the expected DLVO theory for Cryptosporidium particles interacting with quartz surface [26], which they attribute to electro-steric repulsion of the proteins on the cell surface. That indicates that DLVO model might not be sufficient with certain biological cells due to the effects of extra cellular substances

Johnson et al. [22] presented direct experimental observations of the retention of colloids in granular porous media with an energy barrier over a large size range (0.21–9.0 μm). They examined reversibility of attachment with respect to ionic strength reduction and fluid velocity increase. For the entire range of sizes, deposition on the open surface was significant (and dominant for<2.0 μm colloids), and was irreversible with respect to colloid concentration, ionic strength reduction, and fluid velocity increase. This indicates that the mechanism of retention for these colloids was not secondary energy minimum interaction. The mechanism was more likely interaction with surface charge heterogeneity or roughness, sufficient to produce an adhesive force that could not be overcome by the drag force; or alternatively, once contact was established, the colloids were attached via association with the primary energy minimum and hence not affected by increased repulsion from energy barrier increase. For colloids larger than 2.0 μm deposition in grain-to-grain contacts was the dominant form of retention. The colloids associated with grain-to-grain contacts remained in place despite extreme increases in fluid velocity that led to disassembly of the pore structure

From these experiments, it is concluded that deposition in the secondary energy minimum at intermediate ionic strength is an important retention mechanism for micrometer-sized

particles in flow through granular porous media. More importantly, it demonstrated that the electrolytic property of the solute has a great significance with regard to particle deposition and re-suspension. It is a solution property that varies greatly with regard to particle surface charge, solute ionic strength and pH, which is why subsequent computational studies often used a fixed preset interaction profile. In addition, surface charge heterogeneity or roughness appears to have significant impact in randomising deposition mechanisms.

In order to stay away from these problems, Ma et al [7, 24] adopted the point of view of favourable conditions of particle deposition, i.e. in absence of energy barriers. They aimed to take into account grain-to-grain wedging effect in colloidal transport and deposition in saturated porous media. A computational geometry derived from the Happel unit cell [27, 28] description was implemented to predict colloid deposition for a range of porosities. The influence of neighbouring collectors on the fluid flow field was represented by including grain-to-grain contact. Numerical results of the collector efficiencies were derived from a Lagrangian trajectory analysis under a broad range of physical parameter values (e.g. Particle size, fluid velocity, and porosity) under favourable conditions (energy barriers absent.) Predictions agree well with existing experimental data under conditions where energy barriers to deposition were also absent. However, the size of their simulations was not easily achievable in a reasonable computing time with the means available for this work.

Surface charge heterogeneity, roughness and EDL potential morphology issues are specific sources of ongoing research, and this project will endeavour to keep away from speculative assumptions to their regard. It will focus on simpler, well-known and controlled interfacial interaction like Van-der-Waals attraction, the expression of which have been derived, for various interacting objects, in Appendix A. Therefore, simulation reported in this work will only deal with what is called "favourable condition of deposition" where DLVO energy profile only includes the attractive Van-der-Waals component and therefore does not have energy barriers. This allows considering electrostatically inert particles such as latex model particles commonly used in experiments.

1. 2. 4. iv Immersion media

The immersion medium used in this work is chosen to be water for the practical importance of this liquid in colloid suspensions and because the great majority of investigations involving colloids in liquid consider water as immersion media. The study of aerosol dynamics is a fascinating field of work that find applications in many aspects of the real world like medical engineering or industrial gas filtration [15], but it was considered to be a less suitable choice, because mainly of the particle-turbulence interaction modelling that is still a challenge. Shams et al. [29] studied the deposition of aerosol particles of size ranging

from 10nm to 50µm in turbulent channel flow. Effects of gravity, Brownian excitation, Stokes drag and Saffman lift were considered through an extended sub-layer model for turbulent deposition. Particle paths were computed through the equation of motion in a near wall turbulence eddy structure assumed to be coherent (as opposed to chaotic) using Lagrangian simulation, inter-particle interactions being neglected and particles considered to stick to the wall after collision. The limiting trajectory was defined as the path followed by the particles that avoid being swept back into the bulk flow by turbulent eddies. Particles that originated within the region between the limiting trajectory and stagnant flow regions deposit on the wall. Trajectories of particles bigger than 1µm were smooth curves whilst those of particle smaller than 0.1µm had a random course due to Brownian motion. This indicates that Brownian dispersion plays an important role on sub-micrometre trajectories and therefore on deposition. Increasing the particle diameter extends the deposition region and the capture distance decreases. Shams' results show that turbulent boundary layer flows play an important role in the particle deposition process. Shams et al. [29] work shows the kind of very restrictive assumptions that are required when dealing with turbulence effect on particle deposition (idealised as a static eddy velocity field) which can be avoided by considering a liquid immersion fluid. It also introduce the concept of limiting trajectory outside which introduced particle cannot deposit, and shows the importance of Brownian motion on interception. Shams research shows that aerosol modelling is an on-going subject of research that involves extensive knowledge in turbulence modelling and particle/turbulence interaction. The DEM-CFD technique involved in such research is often referred to as extended four-way coupling. It requires computational method like Direct Numerical Simulations (DNS) that is outside both the means and the scope of this work. Regardless, in order to keep scientific coherence, such work would have to indulge in a lot of restrictive hypotheses and idealisation, which restrain its scope; it would also have to overlook the mitigation influence of the particles on the turbulent intensity, which is currently under research.

1. 3 Presentation of study cases

After a brief description of the numerical tools used for this work in CHAPTER 2:, where DEM, CFD and DEM-CFD are presented, physicochemical models and the near-contact hydraulic retardation are discussed in CHAPTER 3:. The implementation of which is described and annotated in CHAPTER 4: along with the C++ code used to customise the simulation platform.

In order to investigate if colloidal particles immersed in water can efficiently be modelled using the DEM-CFD technique, this work includes two numerical studies, presented in CHAPTER 6: and CHAPTER 7:, that derive from previous flowing colloidal suspension

investigations that will be used as validation and comparison material. The specific implementation of the numerical methods for each case study is described in their respective chapters, and a substantive literature review relative to each case study is included with each such description.

CHAPTER 6: reports a study of a colloidal suspension flowing through a microscopic constricted tube. It demonstrates the relevance of particle scale modelling at microscopic scale when cluster formation and particle re-suspension mechanisms are involved. Particle scale point of view is used to examine the dynamics of cluster formation, and particle deposition on the tube wall. It discusses the relevance of including Brownian forces for the particle size over a micron and compares the efficiency and applicability of one-way DEM-CFD coupling against two way coupling. The content of CHAPTER 6: has been accepted for publication in the peer review journal *Particuology* under the title "*Using the DEM-CFD method to predict Brownian particle deposition in a constricted tube"*

The conclusions of the constricted tube study are used in CHAPTER 7: to investigate how particles deposit around the filaments of the spacers commonly used in membrane filtration systems. Particulate fouling of membrane spacers is a critical issue in the field of water filtration and allows investigating the limitations of the described model with a bigger size computational domain and its efficiency in modelling colloidal processes at bigger scale. The content of CHAPTER 7: has been published in the peer review *Journal of Membrane Science* under the title "*DEM simulations of initial deposition of colloidal particles around non-woven membrane spacers"* (Appendix B)

CHAPTER 2: Numerical methods

This work takes advantages of two powerful numerical methods developed in the last decades that, when coupled, offer the possibility to simulate the behaviour of particles immersed in liquid. This chapter describes each one separately at first and then discusses the method used to combine them.

2. 1 DEM implementation description

Discrete Element Method (DEM) originated in 1979 as a numerical tool to model failure phenomena of granular materials in geo-mechanics, in a famous paper by Cundall & Strack named *A discrete numerical model for granular assemblies* [30]. Here, a granular medium is modelled in a discrete fashion as a set of colliding circular rigid particles with translational and rotational degrees of freedom, exerting forces on one another, while being governed by Newton's laws of dynamic equilibrium; particle motion is derived from the force balance integration using an explicit scheme, proceeding by a given Δt at each step. The DEM method is a numerical mechanistic description based on force balance, of what happens in reality, therefore particle scale effects on macroscopic properties can be simulated in a very natural way. This makes this method reliable to describe phenomena that are hard to investigate experimentally. This section describes the specifics of DEM simulation.

Since its inception, the method has been used to investigate and optimise engineering processes and even to create computer animations of artistic value [31]. Either the data can be processed during the simulation or it can be stored for later evaluation. Regarding their approach, discrete element simulations are very close to simulations based on Molecular Dynamics (MD) [32], and despite numerous differences, discrete element simulations of granular materials are still sometimes called MD simulations [33, 34]. MD deals with particles at atomic level and time scales of nano and microseconds. However, in MD, external factors such as constant pressure and constant temperature are important and the particles usually follow the gradient of a complex potential (Lennard-Jones interaction) depending on the relative position of many other particles. Unlike molecular systems, ordinary granular materials evolve on time scales of milliseconds (or larger) and they are usually free of thermodynamic effects.

The interaction of particles may be modelled by either "hard-spheres" or as "soft-spheres" contact models [9]. In a hard-sphere system, the trajectories of particles are determined by

momentum conserving binary collisions. The interactions between particles are assumed to be instantaneous and therefore occur by pairing of particle only and multiple collisions at the same instant cannot be considered. In these simulations, the collisions are processed one by one according to the order in which the events occur. For not too dense systems where collisions do not involve high numbers of neighbouring particles, the hard-sphere models are considerably faster than the soft-sphere models.

In this thesis we use what is known as the "soft-body" method [30, 33, 35], where particles may interact via short or long-range forces and the trajectories are determined by integrating Newtonian equations of motion. This model uses particle overlaps to calculate contact forces based on the extent of the overlaps and the relative velocity of particles contact. The relations between the amount of overlap and the resulting contact force are called elastic models; there are several of them [36], like the linear Contact model or the Hertz Contact model. The main advantage of soft-body models over other approaches is that they can in a natural way be adapted to incorporate long range interactions, contacts, hydrodynamic (section 3. 3), electric, and magnetic (section 3. 7) interactions.

2. 1. 1 Contact detection

Handling the high level of discreteness of granular systems makes discrete element simulations algorithmically complex. Finding the element pairs that are "close" to each other is computationally the most challenging part. Indeed, the overall performance of a discrete element simulation program depends very much on how efficiently this purely geometrical problem is solved, and especially that collision detection must be run at every time-step, since particles change their mutual position from one time-step to another. For that reason, the smaller the time-step, the more often the contact detection and forces updates are needed and the slower the simulation. The most computationally expensive part of DEM algorithm is to create a sufficiently tight set of possibly interacting element pairs and applying the interaction model only to them.

Naïve checking of all possible couples soon leads to performance issues with increasing number of particles, having $O(n^2)$ complexity where n is the number of particles (each particle being checked against each other particle). The method used here to cut on computational cost is to split the domain in a number of cubic elements each of size between 3 and 4 times bigger than a single particle radius, thus reducing the complexity to a few particles in each of these cubes. The space is divided into cells of a given size and each particle assigned to the cell in which its centre point is located. Then, finding the possibly interacting particles is done by checking the neighbouring cells.

Because of its simplicity, this method is widely used in discrete element simulations. If the particles and the cells have more or less the same size and thus in average each cell contains one single particle, this lookup grid gives a solution close to optimum. However, if there are both very small and very large particles in the simulated system, then this becomes less efficient. In case of a fine grid, having a cell size close to the size of the smallest particle, for cells containing a bigger particle, not only the adjacent cells but also second or higher order neighbours are to be considered. If we have a coarse grid, having a cell size close to the size of the largest particle, then a grid cell can contain many small particles. The above problems can be solved by using an adaptive cell size [37]. Starting from a sufficiently large box, containing all the particles, the space is divided into smaller boxes. Each box, which contains more than one particle, is further divided into even smaller boxes. The procedure is repeated until each box contains no more than one particle.

2. 1. 2 Particle interactions

Soft-body discrete element simulations use models that define the contact interaction of the participating objects, from the geometrical overlaps and the relative velocity of colliding elements.

The first introduced contact model is the so called linear spring-dashpot model [30]. When an overlap is established between two bodies, relative to the surface orientation of the objects, a normal and a tangential spring is created at the initial contact point. The motion of the bodies is governed by the compression and elongation of these imaginary springs.

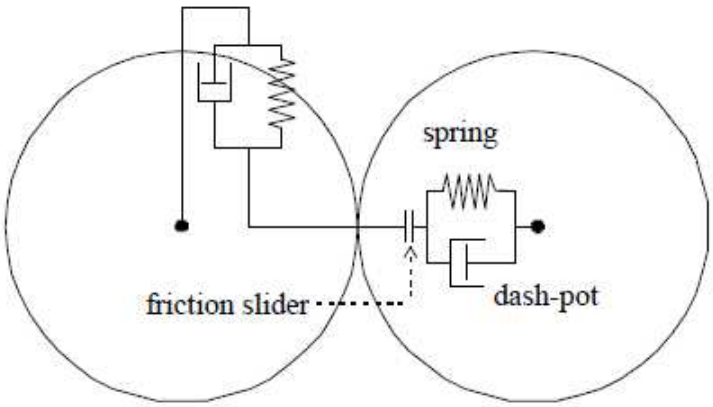

Figure 2.1: Diagram of the linear spring-dashpot soft-sphere model [38]

The normal and tangential components of the force, which the objects in contact exert on each other, is

$$\overrightarrow{F_n} = -\kappa_n \overrightarrow{\delta_n} - \gamma_n \overrightarrow{v_n}$$
$$\overrightarrow{F_t} = -\kappa_t \overrightarrow{\delta_t} - \gamma_t \overrightarrow{v_t}$$

Eq. 2.1

Where κ_n and κ_t are normal and tangential stiffness and $\gamma_{n,t}$ are damping coefficients, to the initial contact point and at contact point.

$$\delta_n = R_1 + R_2 - \left\| \overrightarrow{r_1} - \overrightarrow{r_2} \right\|, \ \delta_t = \int_t^{t+\Delta t} v_t dt$$

Eq. 2.2

DEM interaction defines two stiffnesses, normal stiffness κ_n and shear (tangent) stiffness κ_t which are functions of the Young's modulus and Poisson's ratio of the particle material; however, in practice, their value is often chosen for computing efficiency [39] as they are strongly related to the integration time-step, and their relation to the solid material property disregarded. κ_t is usually taken as a fraction of κ_n, we will use $\kappa_t = \kappa_n$ as it is implemented that way in the EDEM software [40], which would induce stiffer behaviour in densely packed simulations but, is of less importance in our dilute simulations.

A more sophisticated approach to calculate contact forces between two objects is given by the non linear Hertz model [41, 42], where

$$\overrightarrow{F_n} = -\kappa_n \delta_n^{1/2} \overrightarrow{\delta_n} - \gamma_n \delta_n^{1/2} \overrightarrow{v_n}$$

Eq. 2.3

The non-linear Hertz contact model, Eq. 2.3, was used in this work, in order to make sure that particles do not inter-penetrate each other, and that contact forces are transmitted properly between the different geometrical elements of the simulation.

However these considerations have little impact for the present work as collision and elastic contact parameters are less relevant for colloidal particles immersed in water as the relative motion of interacting particles is small, and although mechanical properties of fine particles have been investigated [43], the influence of a surrounding liquid has been shown to alter contact properties [44].

2. 1. 3 Time-step for DEM integration

Integrating the equations of motion in DEM is done through explicit methods. This integration scheme is conditionally stable, meaning that errors due to discrimination are not

magnified provided that $\Delta t<\Delta t_{cr}$ where Δt_{cr} is the critical time-step, above which the integration is unstable.

For a purely translational single mass–spring system with no rotational stiffness (i.e. with a single degree-of-freedom system), where κ is the spring and m the mass of the single particle, the critical time-step is given by [45]:

$$\Delta t_{cr} = 2\sqrt{\frac{m}{\kappa}}$$

Similarly, estimating the time-step in discrete element integration is based on the connection between interaction stiffness and the particle properties.

$$\Delta t_{cr} = l_{\min}\sqrt{\frac{\rho}{\mathrm{E}}}$$

Eq. 2.4

The physical meaning of this equation is that the elastic wave whose velocity is $\sqrt{(\mathrm{E}/\rho)}$, must not propagate farther than the minimum distance ($l_{\min}$) of integration during one time-step. The limiting distance of elastic wave propagation within a step is taken as a fraction of the smallest particle radius. In the present work, such calculation have been used to evaluate the order of magnitude of the DEM time-step. for spherical latex particle with a Young modulus of $\mathrm{E}=10^{-2}$Gpa, a density similar to water and a radius of one micron, the DEM time-step to be used in the simulations has been computed being of the magnitude of $\Delta t_{cr} = 10^{-8} s$.

2. 1. 4 Motion integration

Particles involved in contacts receive forces and torques that are integrated in order to resolve and update their position. These forces define the current acceleration on a particle. The motion integration is the mathematical process by which the acceleration is used to update the particles' position from the current to the next time-step. Updating particle orientation proceeds in an analogous manner, the angular acceleration being computed from torque, although it is slightly more complex as it involved the use of rotation matrices [46], also called quaternion, to compute rotations movements.

2. 1. 5 Particle creation

During simulations, particles can be generated in a number of ways, anytime, anywhere; the most representative way to simulate the particle dispersion in a suspension is to create particles following a uniform distribution within the inlet window. Particle concentration can be tuned through the particle creation rate (Γ_{in}). This easily relates to the inlet bulk suspension's particle concentration [13] by:

$$C_0 = \frac{\Gamma_{in}}{A_w.V_{in}}$$

Eq. 2.5

2. 2 CFD method description

Some exotic, but increasingly popular, numerical methods adopt Lagrangian approaches to model fluids numerically, meaning that they consider the bulk flow as constituted of particle-like fluid parcel, like for instance the Lattice-Boltzmann method (LBM) or Smoothed Particle Hydrodynamics (SPH) [47]. However, the overwhelming majority of CFD studies, and the present work, consider the fluid as continuous and use an Eulerian approach to model it. The following paragraph presents the first principles of fluid mechanics relevant to this work, and briefly describes the discretization technique used.

2. 2. 1 Principles of fluid dynamics:

In Cartesian coordinates, the continuity equation for fluid is written as follow:

$$\frac{\partial \rho}{\partial t} + div\left(\rho.\vec{v}\right) = 0$$

Eq. 2.6

For incompressible flow this becomes

$$div(\vec{v}) = 0$$

Eq. 2.7

The momentum conservation equation for fluids can be written as:

$$\rho \frac{D\vec{v}}{Dt} = -\vec{\nabla} p + \rho \vec{f} + \vec{\nabla}.\mathrm{T}$$

Eq. 2.8

Where: $\left(\frac{D}{Dt} = \frac{d}{dt} + \vec{v}.\overrightarrow{grad} \quad and \quad \vec{v}(x,y,z) = v_x(x,y,z).\vec{i} + v_y(x,y,z).\vec{j} + v_z(x,y,z).\vec{k} \right)$

For an incompressible Newtonian fluid, the closure model for the viscous stress tensor conforms to:

$$\tau_{ki} = \mu.\left(\frac{\partial v_k}{\partial x_i} + \frac{\partial v_i}{\partial x_k} \right)$$

Eq. 2.9

For simplification's sake, the momentum conservation equation is often rewritten as:

$$\rho \frac{D\vec{v}}{Dt} = -\vec{\nabla} p + div\left(\mu.\overrightarrow{grad}\left(\vec{v}\right)\right) + S$$

Eq. 2.10

In which the term *S* is a momentum source term that includes external forces and the smaller contribution term from viscous stresses.

2. 2. 2 Particles in fluid

The characteristics of a fluid flow interacting with immersed particles can be evaluated in terms of dimensionless numbers, which are widely used in fluid mechanics and engineering to define the relative importance of relevant forces acting on the immersed particles. The dimensions and properties of the system are included into calculations of dimensionless numbers so that they give direct information on the effect of scale. The Particle Reynolds number (Re_P) measures of the ratio of inertial forces to viscous forces, and is an indicator of the flow regime around the particles. The Particle Reynolds number influences the choice of the drag coefficient in Stoke's Law equation as explained in section 3. 3. 1. The Peclet number (*Pe*) value indicates the relative importance of convection over diffusion in the particle motion; their expressions are given in the following equations:

$$Re_P = a(u\text{-}v)\rho/\mu$$

$$Pe = av/D_0$$

Eq. 2.11

Where a is the particle characteristic length, u is the fluid velocity, v is the particle velocity, ρ is the fluid density and μ is the fluid viscosity. The term D_0 is the diffusion coefficient given by the Stokes-Einstein relation for a single spherical particle in a liquid with low Reynolds number [48] as $D_0=k_b.T/(6.\pi.\mu.r)$, k_b is the Boltzmann's constant, T is temperature, r is the particle radius,

2. 2. 3 CFD discretization

The equations of fluid motion are numerically integrated in the commercial CFD Package Fluent 12.0 using the SIMPLE algorithm [49, 50] which is a discretization technique based on the finite difference method and, a detailed description of which is given by Versteeg, H.K. and W. Malalasekera [49, 50]. The SIMPLE algorithm uses a staggered grid to reduce numerical instability, and it can also be applied to most multiphase models provided a sufficiently small marching time-step is used [39].

2. 3 Fluid/particle interaction

The main difficulty of modelling two-phase flow is representing the mutual effects between the fluid flow and the solids motion through coupling between phases. Fluid/particle flows can be described by two different numerical models. These are the Euler-Euler approach and the Euler-Lagrange approach. The names of these models refer to the approach used to model the fluid and granular flow respectively. Both models treat the fluid phase as a continuum and some authors refer to them directly as Lagrangian or Eulerian model, the Eulerian nature of the fluid modelling being implied.

In the Euler-Euler model, both the fluid and the disperse phase are considered to be interpenetrating continua and are solved by a generalization of the Navier-Stokes equations [9]. Mass and momentum equations are a generalisation of the fluid mechanics first principles described previously, by introducing the local volume fraction of each phase, α^f and α^s. The mass conservation equations for the fluid phase and the solid phase become respectively [9, 51]:

$$\frac{\partial}{\partial t}\left(\alpha^f \rho^f\right)+\frac{\partial}{\partial x_i}\left(\alpha^f \rho^f u_i^f\right)=0$$

$$\frac{\partial}{\partial t}\left(\alpha^s \rho^s\right)+\frac{\partial}{\partial x_i}\left(\alpha^s \rho^s u_i^s\right)=0$$

Eq. 2.12

In which the volume fractions of each phases are constrained to be supplementary, i.e. $\alpha^f+\alpha^s=1$.

The momentum conservation equation for the fluid phase and the solid phase are respectively:

$$\frac{\partial}{\partial t}\left(\alpha^f \rho^f u_j^f\right)+\frac{\partial}{\partial x_i}\left(\alpha^f \rho^f u_i^f u_j^f\right)=-\alpha^f \frac{\partial p}{\partial x_j}+\frac{\partial \tau_{ij}^f}{\partial x_j}+\alpha^f \rho^f g_j+\overline{S}^{sf}$$

$$\frac{\partial}{\partial t}\left(\alpha^s \rho^s u_j^s\right)+\frac{\partial}{\partial x_i}\left(\alpha^s \rho^s u_i^s u_j^s\right)=-\alpha^s \frac{\partial p}{\partial x_j}+\frac{\partial \tau_{ij}^s}{\partial x_j}+\alpha^s \rho^s g_j-\overline{S}^{sf}$$

Where the source term $\overline{S}^{sf}$ is defined as $\overline{S}^{sf}=K^{sf}\left(u_j^s-v_i^f\right)$ when the disperse phase is made of solid particles [52], and $K^{sf}=K^{fs}$ is the drag coefficient between the phases.

Meanwhile, in the Euler-Lagrange model, the dispersed phase is solved by tracking and solving the Newtonian equations of motion for each individual particle.

The two approaches are suited for different type of flows. The Euler-Lagrange approach is suitable for dilute flows, where the particle concentration is low, although this approach has also been used to model fluid-gas system through Discrete-Bubble modelling [53, 54]. Alternatively the Eulerian method is applied to larger scale simulations where continuum description is more computationally efficient [55]. The continuous approach is especially useful when the volume fractions of the phases are comparable, or when the interaction between the phases plays a significant role in determining the hydrodynamics of the system.

Choosing the most representative model for multiphase flow depends on the volume faction characteristics of the mixture, which is the ratio of the dispersed phase volume with respect to the main phase volume. A classification for multi-phase suspensions based on the order of magnitude of the secondary phase volume fraction α, was given by Elghobashi [56]. At very low solid volume fraction, α<1e-6, the dispersed phase has an insignificant effect on the main flow; the inter-phase exchange of momentum only goes from the main phase to the disperse phase with small inertia. In this case, the flow is modelled as a single-phase fluid and the motion of particle phase is dictated by the hydro-dynamical forces (e.g. drag force, lift force, buoyancy force).This is called one-way coupling.

One-way coupling will be the method implemented the most in this thesis, however it thought that particle aggregates have a local volume fraction that can potentially disturb the fluid flow therefore Euler-Euler method will also be investigated and compared to one-way coupling, the model used for specific simulations of later chapters will be made clear in the relevant had-hoc discussion. Indeed, with increasing volume fraction up to α< 1e-3, the effect of the particle phase on the fluid flow pattern becomes more important. Localised turbulent manifestation in the main fluid can be affected by the dispersed phase, and even the macroscopic flow pattern can be modified. The inter-phase exchange of momentum

goes from the main phase to the disperse phase and reciprocally. This is called two way coupling.

In modelling fluid-particle systems, the Eulerian approach compels the erasure of details of particle flow since it involves an averaging process at the mesh cell level [39]. Additionally, the averaging region should be much smaller than the scale of the flow structure in, but much bigger than the particle size, which can be an issue especially for simulation that require particle scale resolution (e.g. porous media simulations, micro-fluidic modelling).

The alternative is to adopt a coupled DEM-CFD approach where the fluid phase is solved using CFD and the particle motion in a Lagrangian manner using DEM. The two phases then require to be coupled, which can be done in either one or two way coupling. One-way coupling only requires a mono-directional coupling procedure, particle trajectories can be integrated from a previously CFD computed steady velocity field, considering collisions and fluid drag interactions. This makes it dynamic for one phase only and it is therefore relatively straightforward to setup.

Two-way DEM-CFD coupling, however, as described by Tsuji, Kawaguchi and Tanaka [57], is unsteady by nature for both phases and needs to allow communication between CFD and DEM, for the mutual influence of the fluid and the particles to be considered, including the volume fraction taken up by the particles. To achieve two way coupling, computation goes back and forth between DEM and CFD processes as described in Figure 2.2 [58]. However, the fluid meshing process depends on the particle size since it requires the size of the averaging region (i.e. a mesh cell) to be larger than the particle size, in other words, the CFD mesh size limits the particle size of the disperse phase, which prevents fine meshing of the fluid phase.

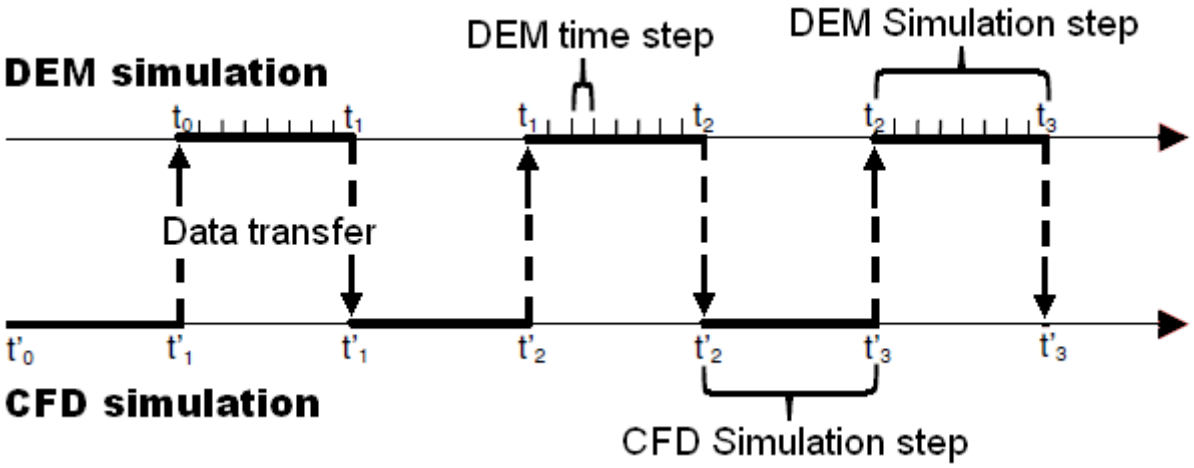

Figure 2.2: Alternating sequence of CFD/DEM coupled simulation

CHAPTER 3: Physicochemical models

The set of forces involved in colloidal suspensions is quite specific to colloidal science. As described by the DLVO theory [1, 8], it may involve chemical effects like the charge properties of colloids surface and the immersion medium, steric forces and hydrophobic force [59], alongside physical effects like dispersion induced Van-der-Waals force and mechanistic forces like drag, lift and buoyancy forces. This work eliminates the complexity associated with chemical specificity by considering only favourable conditions as stated in section 1. 2. 4. iii. However, the remaining forces have to be examined to establish if they are relevant in the scope of this work or not.

This chapter describes the force models relevant to implement colloidal interfacial physics that apply to micro-particles and colloids immersed in flowing water.

3. 1 Fluid flow characteristics

First, let us consider the characteristics of the immersion fluid and establish the state of the flow involved in this work. Colloidal suspensions are usually of interest in processes that typically involve low Reynolds numbers, like flow in low permeability porous media [60].

$$\mathrm{Re}_p = \frac{L\rho U}{\mu}$$

Eq. 3.1

The term *U* is the fluid velocity, L the characteristic length of the geometry, ρ the density of fluid and μ the viscosity of fluid.

Table 3.3 gives an idea of the Reynolds numbers associated with typical flow conditions and geometrical characteristics used in this work. The characteristic length correspond to the order of magnitude of the typical geometrical dimensions used in this work.

Reynolds number			
inlet velocity (m/s)	Characteristic length (micron)		
	10	100	1000
1.00E-03	1.00E-02	1.00E-01	1.00E+00
1.00E-02	1.00E-01	1.00E+00	1.00E+01

Table 3.1: Typical Reynolds numbers involved in this present

It can be seen that the higher Reynolds number presented here is 10, which indicates that only laminar flow was involved in the simulations. Therefore, no turbulence closure model was needed.

Table 3.2 gives an idea of the Peclet numbers associated with this work with typical flow conditions and model particle characteristics. Even for the case of submicron particles at the lowest flow rate, the Peclet number is higher than 1000, which indicates that convection is more than one thousand times more important than diffusion.

Peclet number	$Pe=\frac{uD_p}{D_0};\quad D_0=\frac{k_BT}{3\pi\mu D_p}$		
inlet velocity (m/s)	Diameter (micron)		
	0.1	1	10
	Diffusivity		
	4.29E-13	4.29E-14	4.29E-15
1.00E-03	1.16E+03	2.33E+04	2.33E+06
1.00E-02	1.16E+04	2.33E+05	2.33E+07

Table 3.2: Typical Peclet numbers in idealised granular media

3. 2 Mechanistic force model

Both the shape of the computational domain and the fluid inlet condition (flow rate, inlet velocity) define the characteristics of the velocity field; along with the particle size, distribution, inlet particle concentration and material properties, they define the characteristics of the flowing suspension. The trajectories of the immersed particles within the flow field depend on all of these parameters. The DEM approach takes advantage of the fact that these parameters exert their influence through quantifiable forces in order to compute the particles interactions within the fluid. It is then very natural to use the Lagrangian approach to compute the particle motion. It means that the forces exerted on each particle are integrated; they include colloidal interfacial forces, hydraulic forces, and general body forces. For submicron particles, the governing equation of transport is the stochastic Langevin equation that includes particle Brownian motion. Particle trajectory and particle deposition are controlled by the combined influence of these interactions that is described by the force balance equation (1) [7].

$$m\frac{du_p}{dt}=F_D+F_G+F_L+F_{EDL}+F_{LVdW}+F_B$$

Eq. 3.2

Where m is the particle mass and u_p is the particle velocity vector. F_D is the fluid drag, F_G the gravity force, F_L the shear lift, F_{EDL} the electrostatic repulsion, F_{LVdW} the Van der Waals attraction, and F_B the Brownian forces.

This chapter will define each of these forces, as they are all required to model the flow of a dilute colloidal suspension. It is to be noted, however, that DEM is not commonly used to simulate processes involving very small finite particles, like colloids, so the models and equations presented are implemented through custom made plug-ins, the coding of which is described in CHAPTER 4:. It will also be discussed why some forces commonly used in multi-phase simulations, like added mass (also known as virtual mass force), or basset history force, will not be included.

3. 3 Hydraulic forces

The most basic interaction between an object and the surrounding fluid was enunciated in the 3rd century BC by Archimedes; it is the principle dictating that an object immersed in water will experience an upward force equal to the weight of the displaced volume of water. The original Archimedes scrolls are lost and the oldest written reference of it lies in what is known as the Archimedes Palimpsest [61, 62]. The force associated with the Archimedes' principle is called buoyancy force; it is relevant in both static and moving fluid, and is relatively straightforward to implement knowing the geometry of particles. There are forces that only act dynamically, their dynamic nature makes them slightly more complex to implement, as they require knowing the velocity around the particle for the drag force and even the velocity gradient for the lift force. All of these forces apply to colloidal suspensions [7] and are defined in the following subsections.

3. 3. 1 Drag model

Every object surrounded by fluid with relative motion between object and fluid is subjected to a force that applies in the direction of the fluid velocity; it is called drag force and is proportional to the relative velocity of the object and the fluid. There are different drag models that describe the proportionality coefficient as a function of the object size, shape and characteristics of the surrounding medium. Simple drag models apply only under restricted conditions; the particle must be a solid sphere, the particle must be far from other particles and the vessel wall, so that the flow pattern around the particle is not distorted.

Isolated particles in a fluid are said to be in a free-stream situation, and the so-called free-stream drag model can be applied. In that model, the equation to determine the drag coefficient is a function of Particle Reynolds number (Re_P) (Figure 3.1). There are three regions to be distinguished, the Stoke's Law region, where Re<0.5, the transition region, where 0.5< Re_P <1000, and Newton's law region for Re_P >1000. Table 3.3 gives the Typical Particle Reynolds numbers involved in this work, the maximum particle Reynolds number is lower than 0.1, which defines Stokes' law drag coefficient as:

$$C_D = \frac{24}{R.e_P}$$

Eq. 3.3

particle reynolds number $$Re_p = \frac{vD_p}{\nu} = \frac{vD_p\rho}{\mu}$$

inlet velocity (m/s)	Diameter (micron)		
	0.5	1	10
1.00E-03	5.00E-04	1.00E-03	1.00E-02
1.00E-02	5.00E-03	1.00E-02	1.00E-01

Table 3.3: Typical Particle Reynolds numbers involved in this work

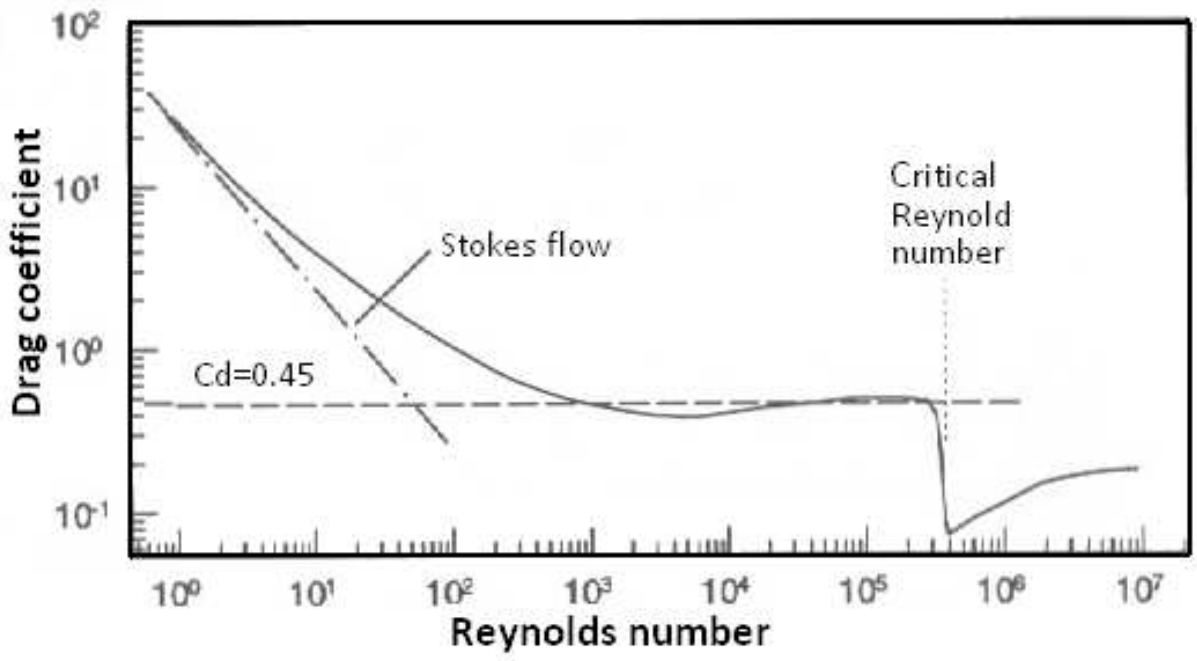

Figure 3.1: Variation of free-stream drag coefficient with Particle Reynolds number [63]

The drag force is expressed as:

$$F_D = \frac{C_D v^2 \rho A_p}{2}$$

Eq. 3.4

Where A_p is the projected area of the particle in the plane perpendicular to the flow direction, and v is the relative velocity of the particle with regard to the surrounding fluid. By substituting Eq. 3.2 into Eq. 3.4, it can be said that:

$$F_D = \frac{12.v^2 \rho.A_p}{\mathrm{Re}_p} = \frac{12.v.A_p \mu}{D_p} = 6.r_p \pi.\mu.v = 3.v.\pi.D_p \mu$$

Eq. 3.5

During the course of a simulation, the conditions under which this drag model applies are not always met. Particles are assumed to remain spherical under all circumstances; however, the proximity to obstacles such as other particles and walls has to be taken into account. The procedure to deal with the presence of walls for the one-way coupling simulations performed for this work is explained in section 3. 4 entitled Near the wall hydraulic retardation.

The influence of surrounding particles is usually taken into account by adapting the drag model to the particle loading characteristics [51]. Several models requiring the local volume fraction around the particle to be known have been proposed, the Ergun Equation [64, 65] being one derived for a dense bed of granular material and relates the drag to the pressure drop through the particle bed [66]. This is not suitable to apply to dilute systems. The Di Felice model [51, 67] is more applicable to dilute suspensions, and corrects the free-stream equation (Eq. 3.4) for the presence of other particles by including a multiplying term ($f(\alpha_f)$), called voidage function (Eq. 3.6), to the drag coefficient that depends on the local fluid volume fraction and flow regimes (i.e. Reynolds number).

$$f(\alpha_f) = \alpha_f^{-(\chi+1)}$$

$$\chi = 3{,}7 - 0{,}65 \cdot \exp\left[-\frac{\left(1.5 - \log R\ e_p\right)^2}{2} \right]$$

Eq. 3.6

The Di Felice model (Eq. 3.6) was therefore used in the two-way coupling simulations performed for this work.

3. 3. 2 Lift model

It is very difficult to study lift forces experimentally because they are governed by the instantaneous and local flow structures as well as the boundary properties of the immersed object [68] and interface characteristics such as surface tension and shape. For that reason, there are more than twenty equations of lift forces, developed over the past six decades of extensive studies as list by Hibiki and Ishii [69]. This is the reason why many ad-hoc expressions of the lift force are used in computational processes.

As a simplifying assumption, it is customary to consider colloidal particles as perfectly spherical, and the vast majority of both experimental and modelling work considers spherical particles for which lift forces have been well studied. For spherical particles, droplets and bubbles [70], there are two sources of lift forces, according to the mechanism producing them. One is the Magnus force produced by a rotating particle (particle spin), which mostly applies in fluids of low viscosity that do not prevent particle spinning freely, typically gases. The other is the Saffman force that occurs when the particle is placed in a flow with local shear and when the Particle Reynolds number is smaller than unity, which generally applies to micron-size particles [71]. It has been demonstrated [72, 73] that wall effects on the Saffman lift are significant in aerosols where turbulent shear stresses are modulated near a boundary [74] , however it is not a concern in this work as for hydraulic suspensions, the wall effect on lift is negligible [75].

In this work, it is assumed that the individual particles have negligible spin due to the surrounding fluid high viscosity. Therefore, only the Saffman lift force is expected to play a role. The velocity gradient normal to a wall $d\mathbf{U}/d\mathbf{n}$, gives rise to a lift force in the direction normal to the wall

$$F_{SL} = 0.25.C.D_p^2.\rho_f\left(U-V\right)\sqrt{\nu\frac{\partial\vec{U}}{\partial\vec{n}}}\ with \quad C = 6.46 \quad \mathrm{Re}_p << \mathrm{Re}_G^{1/2} \quad \mathrm{Re}_G = \frac{GD_p^2}{\nu}$$

Where in Cartesian coordinates

$$G = \sqrt{\left(\frac{\partial u}{\partial z}\right)^2 + \left(\frac{\partial v}{\partial z}\right)^2}$$

Eq. 3.7

The term *z* representing the orthogonal distance from the wall

3. 4 Near the wall hydraulic retardation

Near a wall, the displacement of the fluid between a particle in the flow and the wall becomes increasingly difficult because of the fluid between the particle and the wall needing to be accelerated (Figure 3.2). This causes the particle to bear an additional hydrodynamic drag over and above the free-stream drag on the particle. Hence, near a wall, particle motion is retarded due to the cushioning effect of the wall. Similarly, the presence of neighbouring particles causes the mutual retardation of the particles, however the physical model used in this work do not consider inter-particles retardation effects as it is a very a very complex subject [76] that would require its own research project to be incorporated into DEM framework. In colloidal deposition studies, it is usually assumed that the presence of colloidal particles does not disturb the flow field of the suspending fluid [48] so a fluid dynamic computation of the undisturbed flow field is used to calculate the near-the-wall velocity of the suspended particles.

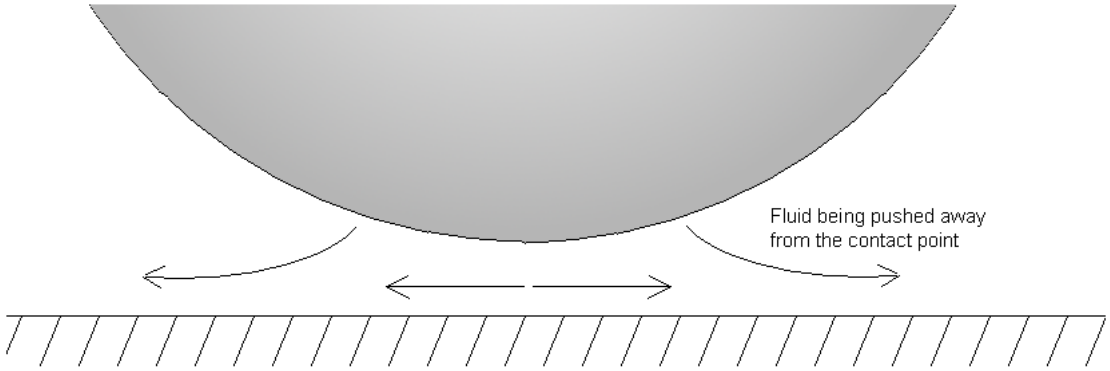

Figure 3.2: Fluid behaviour between a wall and an approaching particle [77]

Particles can approach the wall from any direction so it is useful to consider separately their parallel and normal components with respect to the wall reference frame. The decomposition of the 3D-vector of the particle velocity into the wall's local reference frame is defined by its projection on the vector normal to the surface and its projection on the plane tangential to the surface, as illustrated in Figure 3.3.

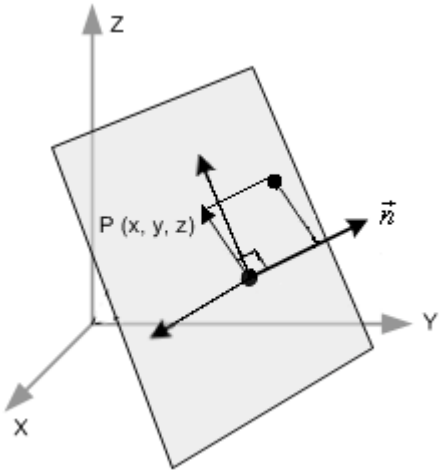

Figure 3.3: Principles of 3D projection

Any motion of the particle relative to the wall can therefore be expressed as the sum of a velocity vector orthogonal to the wall and a velocity vector parallel to the wall.

3. 4. 1 Superposition property of Stokes equation solutions

In the previous section, it was explained that particle movement with respect to a wall can be set in a wall local frame of reference. This section explains how the linear nature of the Stokes' equation allows the drag forces arising from various velocity components to be superimposed.

The drag force acting on a sphere of radius r_p can be described by Eq. 3.5:

$$F_D = 6r_p \pi \mu . u$$

This relation derives from the early work of Stokes on fluid dynamics. Therefore, it is often referred to as Stokes' law. It applies at small Reynolds numbers, Re < 1. In this condition, the inertia of the fluid is neglected and the momentum conservation equation of the Navier-Stokes system, assuming negligible external forces, becomes:

$$\vec{\nabla} p = \vec{\nabla} . \vec{\tau} = \mu \nabla^2 \vec{v}$$

Eq. 3.8

This relation is known as the Stokes equation and is the principle equation of colloidal hydrodynamics. It applies considering all of the above restrictions, meaning for steady state laminar flows with inertial effects being neglected. The Stokes equation has the very useful property of being linear, which means that any linear combination of solutions to this equation will still be a solution. This property can then be used to decompose complex flow fields into adequately simple ones, the solutions of which can be added to obtain solutions for the complex flow field.

The cushioning effect (also called retardation) described in Figure 3.2 has been studied and Stokes law correction factors for particle motion near a wall were derived [48, 78-82] in the mid twentieth century taking advantage of the linear superposition property of the Stokes equation, and have been used ever since. The following section describes the treatment of the wall's presence through these retardation models, which apply to the different components of particle velocity.

3. 4. 2 Particle impinging orthogonally on a rigid wall

Regarding the retarding drag for the velocity component orthogonal to the wall, the linearity of the Stokes equation will be used to decompose the motion of the particle in a moving fluid toward a wall as the sum of the moving particle in a static flow and the drag felt by a static particle in a moving fluid. The associated drag coefficients will be taken respectively from Brenner's work [78, 81], who proposed a solution when the fluid is bounded longitudinally, meaning perpendicularly to the direction of motion of the particle, and Nguyen and Evans [83], who derived drag coefficients for a motionless particle immersed in a flowing liquid near a wall.

Such decomposition leads to a modified Stokes law [7] where the short-range hydrodynamic force applied to a sphere with radius a can be described by:

$$F_{D\perp} = F_1 + F_2 = -6\pi\mu.aV.\lambda_{\perp} + 6\pi\mu.aU.f_2$$

Eq. 3.9

In the modified Stokes law, Eq. 3.9, the drag force is composed of the sum of two terms. The first term, F_1, corresponds to the case where the particle with velocity V normal to the wall moves in a zero velocity field and therefore experiences a drag in the opposite direction of its velocity. The second term, F_2 corresponds to the case of a motionless particle within a liquid flow field with velocity U at the centre of the particle. The particle therefore experiences a drag in the same direction of the liquid velocity. In each term of the modified Stokes law, the retardation effect from the presence of a nearby wall is accounted for by the introduction of retardation factors $\lambda_{\perp}$ and f_2. They are functions of the inter-surface separation distance $\delta=h-a$, Figure 3.4, assuming a non-slip boundary condition that applies to both the particle and the wall surfaces.

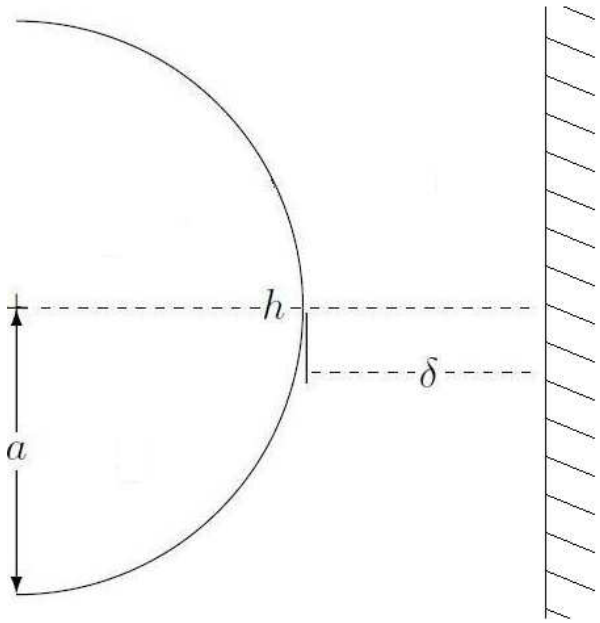

Figure 3.4: Parameter definition of wall/particle interaction model

The introduction of such correction factors dates back to the work of Lorentz (1907), who deduced an approximate equation, Eq. 3.10, of the effect of a sphere falling towards an infinite rigid plane [84], which is only valid when the sphere radius is small compared to the separation distance. Typically, when the sphere is more than twenty times its radius from the plane [85, 86] Lorentz found that the resistance of the particle is greater than predicted by Stokes' law by a factor $\lambda_{\perp}$.

$$\lambda_{\perp} = 1 + \frac{9}{8}\left(\frac{a}{h}\right) + o\left(\frac{a^2}{h^2}\right)$$

Eq. 3.10

Independently of the ratio of radius to distance, Brenner [78] calculated the general analytical expression for $\lambda_{\perp}$ as the following Taylor expansion:

$$\lambda_{\perp} = \frac{4}{3}\sinh(\alpha)\sum_{n=1}^{\infty}\frac{n(n+1)}{(2n-1)(2n+3)}\left(\frac{2\sinh\left((2n+1)\alpha\right)+(2n+1)\sinh(2\alpha)}{4\sinh^2\left((n+1/2)\alpha\right)-(2n+1)^2\sinh^2\alpha}-1\right)$$

With

$$\alpha = \cosh^{-1}\frac{h}{a} = \ln\left(\frac{h}{a}+\sqrt{\frac{h^2}{a^2}-1}\right) = \ln\left(\frac{\delta}{a}+1+\sqrt{\frac{\delta^2}{a^2}+2\frac{\delta}{a}}\right)$$

Eq. 3.11

The first two terms of Brenner's equation, Eq. 3.11 , are the Lorentz formula, Eq. 3.10.

Nguyen and Evans [83] derived the expressions for the retardation coefficients, f_2, of a motionless colloidal sphere approaching a solid surface, which correspond to the second

term of the modified Stokes law, Eq. 3.9. It also takes the form of Taylor expansion and applies to a spherical particle approaching a much larger solid surface with non-slip boundary conditions at low Reynolds number.

$$f_2 = \frac{4\sinh^5\alpha}{9\cosh^2\alpha}\sum_{m=1}^{\infty}\frac{m(m+1)(m+1/2)^2}{\sinh^2(m\alpha+\alpha/2)-(m+1/2)^2\sinh^2\alpha}$$

Eq. 3.12

In order not to hinder computation efficiency, by the computation of an infinite series, Nguyen and Evans [83] also gave accurate approximate expressions for the analytical retardation coefficients $\lambda_{\perp}$ and $f_{2,}$ Eq. 3.13. For a solid particle approaching a much larger solid surface with non-slip boundary conditions at low Reynolds numbers, the approximate solutions used in this work are [83]:

$$f_2 = \frac{2.022+h/a}{0.626+h/a}$$

And

$$\lambda_{\perp} = \left[1+(a/h)^p\right]^{1/p}$$

With p=0.89

Eq. 3.13

It is now clearer that the retardation factors tend to unity at a large enough distance from the wall, which makes the modified Stokes law consistent with the original.

3. 4. 3 Translational motion of a sphere parallel to a rigid wall

Thanks to the linearity of the Stokes equations, the motion of a spherical particle flowing past an obstacle can be seen as the combination of a particle translating in a non-moving fluid and a fixed particle immobile in linear shearing flow. The linear shearing flow hypothesis is a local simplification of the flow condition, where the local shear rate is assumed to change very little over the particles dimension [48]. Therefore, the drag force retarded by a longitudinal wall can also be expressed as the sum of these two contributions:

$$F_{D//} = F_{1//} + F_{2//} = -6\pi\mu.aV.\lambda_{//} + 6\pi\mu.aU.f_3$$

Goldman et al [79, 80] developed asymptotic solutions for both terms of the modified Stokes' law for a particle flowing past an obstacle. For a non-rotating sphere near a plane in a quiescent fluid, Goldman et al computed the asymptotic drag retardation function:

$$\lambda_{//} \approx \frac{8}{15}\ln(\delta / a) - 0.9588$$

Eq. 3.14

It is important to observe that Goldman's asymptotic drag retardation function is asymptotic means that it approximates the retardation function, at small distances and does not apply to distances larger than a few radii.

To this should be superimposed, considering the linearity of the Stokes equation, the force induced by a linear shearing flow past an immobilized sphere near a rigid wall, where the retardation factor is approximated by:

$$f_3 = 1 + \frac{9}{16}\frac{a}{h}$$

Eq. 3.15

The resulting drag force, $F_{D//}$, combining the two components, then corresponds to a non-rotating solid particle flowing along a much larger solid surface with non-slip boundary conditions at low Reynolds numbers.

3. 5 Other hydraulic forces

A thorough description of the forces used to described micro-particles immersed in water requires comments on two forces are sometimes used [87] or omitted in various works depending on the study parameters.

The first one is the virtual mass force that relates to the force required to move, or accelerate, the surrounding fluid, when the relative velocity changes. It is also called apparent mass force because it is equivalent to adding a mass to a particle [69].

$$F_{virt} = C\frac{\pi D_p^3}{6}\frac{\rho_f}{2}\frac{d(U-V)}{dt}$$

Eq. 3.16

Where C is an added-mass coefficient that is to be determined by experiments [88]. The added mass effect has not been considered in this work as changes in relative velocity between particles and fluid are assumed to remain small.

The second one is the Basset force [89] that describes the effect of the changing relative velocity on the viscous drag and the boundary-layer development. It addresses the temporal delay in boundary layer development when the relative velocity changes with time, and is sometimes called the "history" term as its expression involves the integration over time of the relative acceleration of the particle with respect to fluid [90].

$$F_{Bass} = 6r_p^2 \sqrt{\pi \mu_f \rho_f} \int_0^t \frac{1}{\sqrt{t-\tau}} . \frac{d(U-V)}{d\tau} d\tau$$

Eq. 3.17

The Basset term and virtual mass term can be neglected under conditions of small density ratio [91, 92], when particle acceleration with regard to surrounding fluid is small, again, this force will be neglected in this work as changes in relative velocity between particles and fluid are assumed to remain small. In other conditions, the Basset force is very often disregarded, as the conditions of its numerical implementation are not always clear.

3. 6 Brownian motion and diffusion

Sub-micron sized particles are subject to forces arising from Brownian motion, and the local Stokes' drag force must be corrected for this by a Cunningham factor [93], regardless of near the wall hydraulic retardation on the Stokes' drag. The drag force expression is then given by:

$$F_D^{sub} = F_D^{ret} / C_C \text{ where } C_C = 1 + \frac{2\lambda}{d}\left(1.2571 + 0.4e^{-0.55d/\lambda}\right)$$

Eq. 3.18

F_D^{ret} Is the usual drag force including the hydraulic retardation and λ is the molecular mean free path of the surrounding medium.

$$\lambda = \frac{\sqrt{mk_BT}}{\xi} \text{ in a fluid [7] and } \lambda = \frac{\mu}{\sqrt{2P\rho/\pi}} \text{ in a gas [13]}$$

Eq. 3.19

Where ξ is the drag or friction coefficient ($\xi = 6.\pi.\mu.r_p$), k_B is the Boltzmann constant and T is the temperature in Kelvin.

Following the method used by Ounis et al. (1991) [93], the Brownian force components are independent white noise processes. Three independent Gaussian random numbers (Gi) of zero mean and unit variances are generated, Figure 3.5, each corresponding to one component of the random force. These relate to the Brownian force (F_B), to be implemented in the momentum conservation equation (Eq. 3.2), by:

$$\overrightarrow{F_B} = \sum_{i=1}^{3} N_i \vec{e_i}$$

Eq. 3.20

Where N_i is the amplitude of the i[th] component of the Brownian force and is expressed as:

$$N_i = G_i \sqrt{\frac{\pi S}{\Delta t}} \quad \text{where} \quad S = \frac{2 k_B T f}{\pi}; \qquad f = \frac{6\pi\mu r_p}{C_c} \quad \text{so} \quad N_i = G_i \sqrt{\frac{6\pi\mu r_p . 2 k_B T}{\Delta t . C_C}}$$

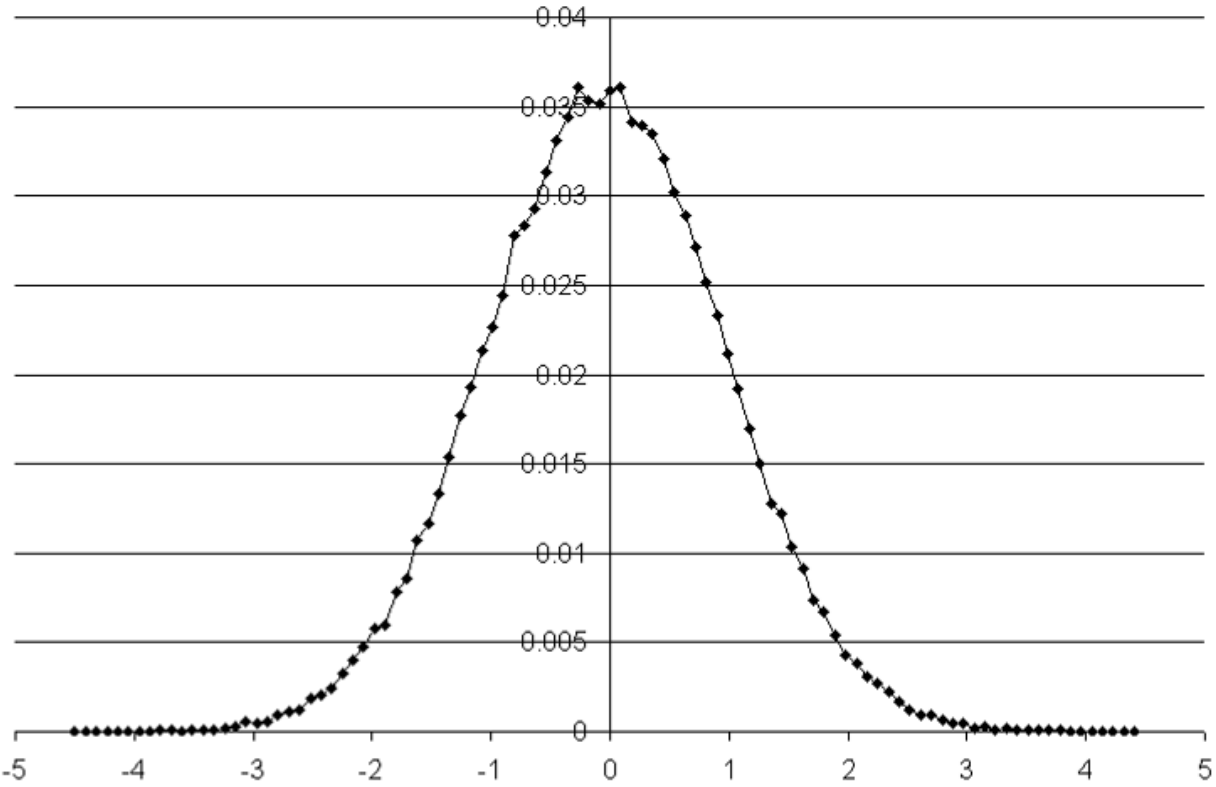

Figure 3.5: Example of a randomly generated Gaussian distribution with zero mean and unit variances

The probabilistic nature of Brownian forces, the components of which being three independent white noises of amplitude defined in Eq. 3.20, requires that a sufficiently large population of particle trajectories be simulated, in this work at least one thousand, in order to achieve robust results.

3. 7 DLVO forces

In fine particle suspensions, the interaction force between particles can be understood as a superposition of three main components: London-Van der Waals, electrostatic double layer and forces mediated by polymer chains. They form the core of the so-called DLVO theory in the colloidal domain, ranging from the nano-meter scale to the micrometre scale, depending on the considered definition, particles can already be considered as subject to mechanistic

forces (as opposed to relativistic or statistical forces). The way in which colloidal particles behave when immersed in a solution is constrained by surface forces and surface fluid interaction that are described by the DLVO potentials.

The combined effect of London-Van der Waals (LVdW) interaction and the electrostatic double layer (EDL) interactions can be summarized on a plot of total potential energy as a function of the particle-particle surface separation. The potential energy of interaction controls the rate of coagulation or flocculation. The DLVO potential curve can feature a primary minimum associated with coagulation, an energy barrier, and a secondary minimum associated with reversible flocculation. Figure 3.6 shows typical profiles of DLVO energy surface interaction. (from Kuznar and Elimelech 2007 [19]). Figure 3.6.a shows the general profile, featuring a peak that represents an energy barrier between the primary energy minimum and the secondary energy minimum.

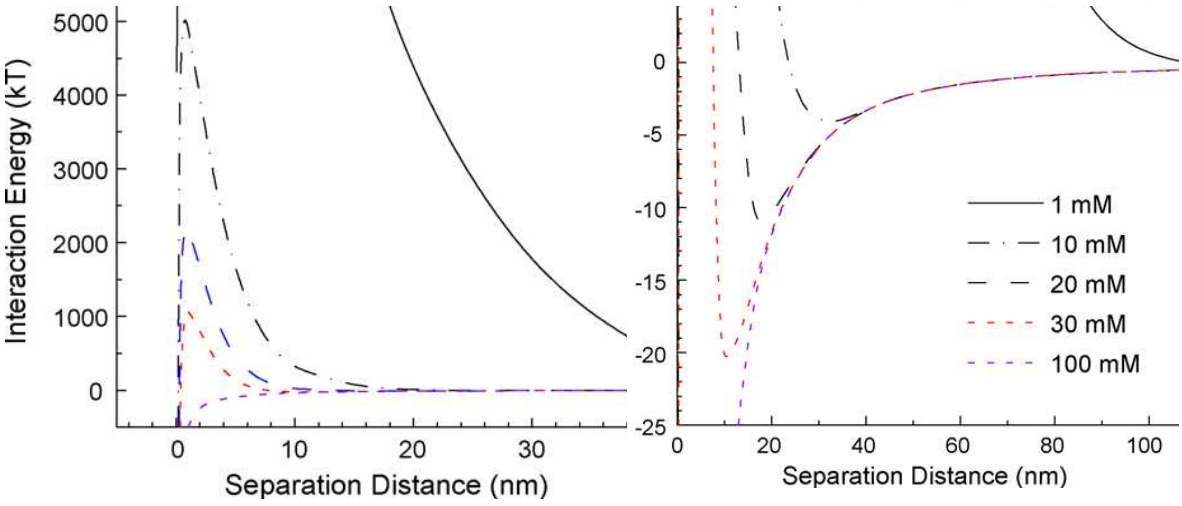

a. b.

Figure 3.6: energy profiles of DLVO surface interaction

The primary energy minimum is associated with virtually irreversible association, which is achieved when sufficient momentum from thermal, hydrodynamic forces or inertial forces overcome the energy barrier. For systems that obey the DLVO model, the barrier can be removed by adding the right amount of electrolyte (in Figure 3.6, this is achieved for a solution of 100mMol/L of KCl). In that case, the DLVO potential would be only attractive. The secondary energy minimum is shallower for bigger energy barriers, which induces less attachment, for that reason, the secondary energy barrier, is also called the repulsive barrier. Figure 3.6.b presents a close up of the secondary energy minimum.

Due to the consequent amount of work involving DLVO forces, a lot side theories and expansions have been developed to match specific studies and it is very easy to get bogged

down in new development and assumptions. This section aims to clarify the concepts of the DLVO theory and explains the equations applied in the scope of this thesis.

3. 7. 1 The thermo-dynamical meaning of forces

From a mechanistic point of view, it is relevant to express interactions between mesoscopic and macroscopic bodies in term of force balance. However, most published works on colloid science and surface chemistry deal with interaction energies rather than forces. However, DEM-CFD modelling requires forces, so it is of great importance to understand how to link previous work with the relevant forces.

The work on a system is equal and opposite to the resulting difference in its internal energy. On the other hand, the work received by a system (which is the stored energy or "potential" energy E_{pot}) is defined as a force multiplied by a distance. Indeed, there is a simple relation between the energy stored in a system and the resulting force associated with that work, which defines the thermo-dynamical meaning of the force F. in Eq. 3.21.

$$F = -\frac{dE_{pot}}{dl}$$

Eq. 3.21

The same principle stands for various different systems of forces and energies (e.g. spring force, gravitation, magnetism etc).

3. 7. 2 Van-der-Waals forces

Van-der-Waals interactions (sometimes refereed to as London-Van-der-Waals) are nearly always attractive and ubiquitous between all matter [94] that supports electromagnetic fluctuations (i.e. polarisable). They can be calculated for simple geometries using the Hamaker theory [95], as described in the Appendix A. The attractive force between two identical spheres of radius a, interaction at a short distance ($l<<a$) has the following expression:

$$F_{lvdw} = -\frac{a}{12}.\frac{H\left(particle\ 1,\ medium,\ particle\ 2\right)}{l}$$

Eq. 3.22

Attractive interaction between any pair of molecules arises from the correlation between the electron motions in the two molecules [1]. While electrons circle the nuclei, they create

instantaneous dipoles that generate fields on the other molecule, whose electrons are then affected. This phenomenon is the London dispersion interaction (after Fritz London who first described that phenomenon) [95, 96]. The dispersion interaction can be described by a relevant quantum mechanical formalism of only formal interest and outside the scope of this work. It is therefore appropriate to jump directly to the derivation of mesoscopic equations.

In 1932, Fritz London gave a quantum mechanical explanation of non-polar Van-der-Waals forces that are weak attracting forces acting between molecules. These universal forces originate in the polarization of an atom due to the fluctuation of the charge distribution of another nearby atom. It is assumed that these forces are purely additive and not affected by the presence of other atoms (therefore by the immersion medium). According to London's theory, the universal Van-der-Waals forces between two atoms will be proportional to r^{-7}. The corresponding attractive potential therefore varies as

$$E_{pot} = -\frac{\lambda}{l^6}$$

Eq. 3.23

In which the term λ, is proportional to the polarizability, α, of each atoms. This should lead to a very short-range force, but the additive collaboration of all atoms of one assembly (like colloids) makes the total force decrease much more slowly with particle distance, making the resulting total force act as a long-range force.

The choice in this thesis is to restrict the focus to the simulation of favourable conditions, as explained in 1. 2. 4, meaning that only the Van-der-Waals force between two spherical surfaces immersed in a fluid medium is considered of Eq. 3.24, along with the interaction between a spherical particle and a flat plate. The derivation of this can be found in the Appendix A.

$$F_{spheres} = \frac{32}{3} n^2 \lambda \pi^2 R \frac{b^3 a^3}{\left(\left((R+a)^2 - b^2\right)\left((R-a)^2 - b^2\right)\right)^2}$$

Eq. 3.24

$$f_{plate}^{sphere} = \frac{2.n^2.\lambda.a^3.\pi^2}{3.\left(R^2 - a^2\right)^2}$$

Eq. 3.25

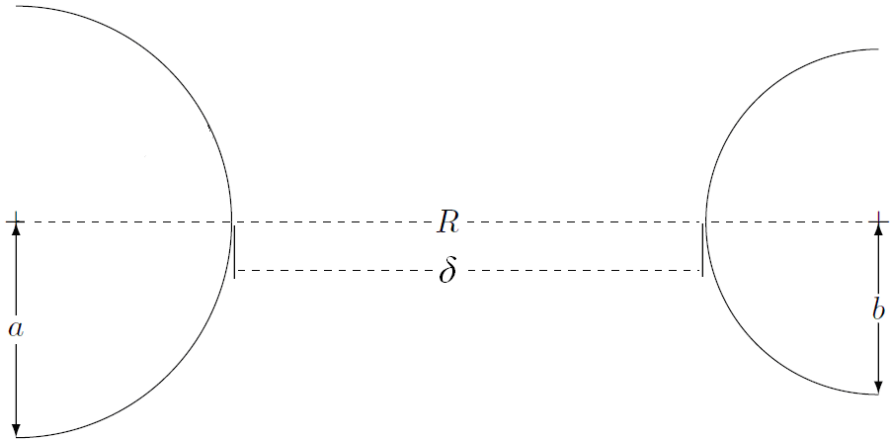

Figure 3.7: Interaction between two spherical particles

For two spheres of same radius and $\delta << a$:

$$F_{lvdw} = \frac{Ha}{12.\delta^2}$$

With $R = 2a + \delta$

It can be seen that the Van-der-Waals interaction tends to infinity when δ tends to zero so for numerical calculations, this forces has to be restricted to a maximum. In addition, the way Van-der-Waals force is implemented in combination with contact forces from DEM technique; it is the case that δ can be negative when the particles overlap during collision. The force therefore has to be minimise to zero for the it not to turn repulsive.

$$0 < F_{lvdw} < F_{MAX}$$

Hamaker studied the interaction of two spherical particles in terms of curves, giving the potential energy of two particles as a function of their distance. He also investigated the LVdW potential of such particles immersed in a medium and introduced the coefficient $H=\pi^2.n^2.\lambda$ known as the Hamaker constant. It depends on the material of each particle and on the material of the dispersion medium. However, the λ coefficient in the Hamaker constant does not have an explicit formal expression so Hamaker had to determine it from experiment for a wide range of materials.

A widely accepted alternative to Hamaker Theory was given in the 50's by a group of physicists led by Eugene Lifshitz [1, 97], They solved the LVdW interaction as an electrostatic problem by adopting a continuum electrodynamics point of view in which each medium is characterized by its dielectric permittivity ε_r. Surprisingly they yield similar results in terms of distance dependence, with the advantage of giving a formal expression for the Hamaker constant, namely:

$$H_{121} = \frac{3}{4} k_B T \left[\frac{\epsilon_1(0) - \epsilon_2(2)}{\epsilon_1(0) + \epsilon_2(0)} \right]^2 + \frac{3\hbar}{4\pi} \int_{k_B T/\hbar}^{\infty} \left[\frac{\epsilon_1(i\omega) - \epsilon_2(i\omega)}{\epsilon_1(i\omega) + \epsilon_2(i\omega)} \right]^2 d\omega$$

Eq. 3.26

However Hamaker constants are mostly taken from experimentation, referring to Johnson et al [98], and are of the order of 10^{-21} J to 10^{-20} J. The magnitude of the Hamaker constant might seem to make the VdW force negligible however, that would be forgetting that δ^2 is of the order of 10^{-16} m^2 which balance the magnitude of the force to a non negligible amount for micron size particles.

Magnetic retardation effects should also be included as a multiplying factor in the Van der Waals force expression [99]:

$$f_m = \frac{\lambda(\lambda + 22.24.\delta)}{(\lambda + 11.12.\delta)^2}$$

Eq. 3.27

The term λ is the characteristic wavelength of interaction, which is taken to be 10^{-7} m.

3. 7. 3 EDL forces

Many particles immersed in a fluid have their surface charge modified. In water, surface charges arise from the ionization of the surface group adsorption/desorption of ions (Figure 3.8). Such particles are then surrounded by a diffuse cloud of ionic species. In this layer, the charges become balanced in an equal but opposite atmosphere of counter-ions close to the surface. Because of the charges present at the solid surface of objects and the charges present in the ionic cloud, the electrostatic shell around particles is referred to as the electrical double layer (EDL).

$$R - H \xrightarrow{ionization} R^- + H^+$$

Figure 3.8: Ionisation of surface group

When the electrical double layers of like-charged particles overlap, it results in a repulsive potential that acts to stabilize the suspension. The EDL potential (E_{pot}) between two charged particles, surrounded by such an ionic cloud, is a function of the separation distance, the surface potential and the ionic property of the medium. For example, to control the flocculation process, the EDL can be modified by chemically modifying the medium in order to alter the electrical double layer.

Electrostatic force between two spherical surfaces with interacting double layers is given by [100, 101]:

$$F_{edl} = \varepsilon_r \varepsilon_0 \pi \kappa \frac{ab}{a+b}\left[\frac{2\Phi_{01}\Phi_{02} - \left(\Phi_{01}^2 + \Phi_{02}^2\right)\exp(-\kappa D)}{\exp(\kappa D) - \exp(-\kappa D)}\right]$$

Eq. 3.28

With

$$\kappa = \left(\sum_i \frac{e^2 z_i^2 c_{i0}}{\varepsilon_r \varepsilon_0 k_B T}\right)^{1/2} = \sqrt{\frac{2.e^2 N_a}{\varepsilon_r \varepsilon_0 k_B T}}.\sqrt{I}$$

Eq. 3.29

Where c_{i0} is the bulk number concentration of specie and $I = \frac{1}{2}\sum_i z_i^2 c_{i0}$, for a 1:1 electrolyte, I is the electrolyte concentration. Table 3.4 summarises typical values of surface interaction parameters and useful universal constants necessary to implement the DLVO physics.

Parameter	Value
Surface potential Φ_{01}, Φ_{02}	Usually Between -80 and 80 mV
Dielectric constant of the solvent ε_r	78.54
Hamaker constant $n^2\lambda\pi^2$	Between 1e-21 1e-20 J
Universal constant	**Value**
Boltzmann constant k_B	1.381e-23 J/K
Charge of the electron e	1.6e-19 C
Permittivity of vacuum ε_0	8.85e-12 C/Vm (V=J/C)
Water dynamic viscosity μ	1e-3 Pa.s
Permittivity of water $\varepsilon_r\varepsilon_0$	7.083e-10 C^2/Jm

Table 3.4: Typical values for surface interaction parameters and useful universal constants

As previously stated, predicting colloidal deposition and agglomeration remains a major challenge [102], because of complex mechanisms of colloid-obstacle interactions. Mainly because of the particularity of EDLs to each system, the choice of surface potentials and ionic cloud morphology [19] would restrict the scope of this work. The EDL model will therefore not be implemented in this work

Given knowledge of all the electrical properties of a suspension, as listed in Table 3.4, one could however apply the method described in this work to ideal EDL systems, as suggested by the work of Johnson and Ma [6, 7, 22, 102]. This would be done by including the resulting EDL model, Eq. 3.28, in the force balance. Care should however be taken in presence of a narrow energy barrier as the simulation time-step would need to be small enough so that particles do not move across from one time-step to the next one, being falsely allowed through it without being affected by it [103].

3. 8 Summary of model forces

In this chapter, the forces relevant to implementing colloidal interfacial physics in the modelling of aggregation and deposition of colloids immersed in water have been described.

It has been explained that the EDL force was not considered as it would narrow the scope of the work to a more chemically specialized study. Moreover, other forces like the Basset force or the added mass force have not been included as they were assumed to have negligible influence on the outcome of the simulations.

The forces that will be considered are the buoyancy force, the drag and lift forces, the Van-der-Waals force, the near the-wall hydraulic retardation and the Brownian force. These are the forces considered to have an influence on the dynamics of colloidal particles in favourable deposition and agglomeration conditions. Therefore, they need to be incorporated in the momentum conservation equation (Eq. 3.2) of the discrete element modelling.

Table 3.5 summarises which forces are considered and numerically implemented in the DEM-CFD simulations relevant to this thesis, and which one were not considered and why.

The next chapter describes the C++ coding used to implement the considered forces in the EDEM software API

Included Force models	Expression	Ref	Use
Van der Waals	$F_{lvdw} = \frac{32}{3} n^2 \lambda \pi^2 R \frac{b^3 a^3}{\left(\left((R+a)^2 - b^2\right)\left((R-a)^2 - b^2\right)\right)^2}$	[7, 8]	Sum over interacting pairs of induced dipoles.
Drag	$F_{D\perp} = -6\pi\mu RV.\lambda_{\perp} + 6\pi\mu RU.f_2$ $F_{D\perp} = -6\pi.\mu.a.V.\lambda_{\perp} + 6.\pi.\mu.aU.f_2$	[79, 80]	Fluid drag on particle considering planar wall retardation.
Brownian	$\overrightarrow{F_B} = \sum_{i=1}^{3} N_i \vec{e_i}$ with $N_i = G_i \sqrt{\frac{\pi S}{\Delta t}}$	[93]	Thermal motion for sub-micron particle.
Gravitational	$F_G = \frac{4}{3} \pi R^3 \left(\rho_p - \rho_f\right) g$		Buoyancy force on immersed particles.
Shear Lift	$F_{SL} = 0.25.C.D_p^2.\rho_f \left(u_f - u_p\right) \sqrt{\nu \frac{\partial u_f}{\partial n}}$	[104]	Lift induced by flow assumed to present linear shear across particles

Ignored Force models	Expression	Ref	
Electrostatic double layer	$F_{edl} = \varepsilon_r \varepsilon_0 \pi\kappa \frac{ab}{a+b} \left[\frac{2\Phi_{01}\Phi_{02} - \left(\Phi_{01}^2 + \Phi_{02}^2\right)\exp(-\kappa D)}{\exp(\kappa D) - \exp(-\kappa D)} \right]$	[100, 101]	Solute/solid pair specific that did not fit the general scope of the study. Ongoing research challenge.
Added mass	$F_{virt} = C \frac{\pi D_p^3}{6} \frac{\rho_f}{2} \frac{d(U-V)}{dt}$	[69]	Neglected because of small density ratio conditions [91, 92]. Small relative acceleration.
Basset Force	$F_{Bass} = 6r_p^2 \sqrt{\pi\mu_f \rho_f} \int_0^t \frac{1}{\sqrt{t-\tau}} . \frac{d(U-V)}{d\tau} d\tau$	[89]	

Table 3.5: Summary of forces models

CHAPTER 4: Implementation

4. 1 Introduction

This chapter describes how relevant physical models described in the previous chapter were implemented into EDEM 3.2. Relevant figures and equations from CHAPTER 3: are repeated for comprehension sake, together with examples of C++ code written by the author, or where stated, provided by the Edinburgh based company DEM Solutions. The code presented here fits in the API framework and object classes provided by DEM Solutions, which includes header files, macro functions, and file managing and vector arithmetic routines, which will not be described as they are documented in the EDEM 3.2 support files [105]. The contextual coding like global variables initialisation and branching structures was provided by DEM Solutions and customised by the author. Specific explanation of the code will be given as C++ comments (i.e. after //) of the code.

4. 2 The EDEM platform

Mechanistic principles and numerical methods [106, 107] were implemented via the EDEM™ 2.3 software [35, 58]. The DEM computation process is described in Figure 4.1. Physicochemical models were implemented via API programming, through custom contact model plug-ins at step 4 that includes interfacial DLVO forces, and near the wall hydraulics. The one way coupling was implemented at step 5 with drag force custom plug-ins, through the EDEM Field Data Coupling Module that allows to import CFD velocity field data. The commercial CFD software Fluent was used to compute numerically the velocity field by solving numerically the steady state Navier-Stokes equations. The two-way coupling uses a coupling module added to Fluent, provided by DEM Solution Ltd, which allows the communication between the EDEM platform and the CFD calculations at step 5.

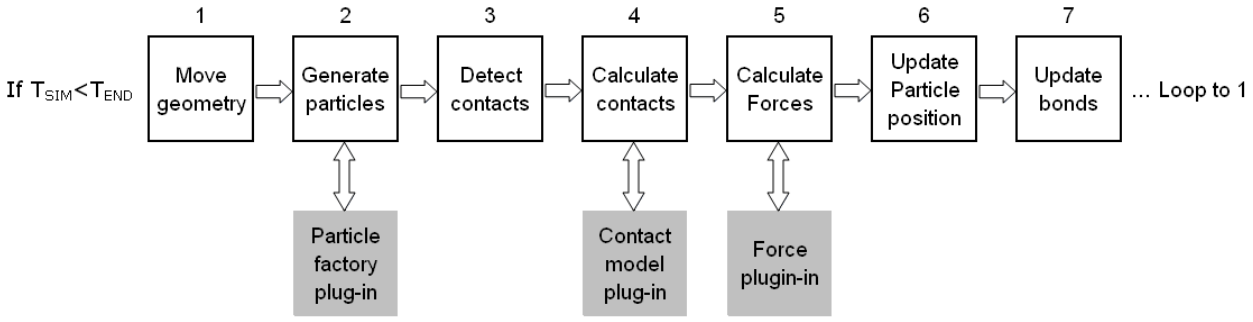

Figure 4.1: DEM computation flow chart

This chapter describes the coding associated with the physicochemical models described in chapter 3. The first section describes how the contact detection model is used to detect when particles are in near collision situation or when they are in an actual contact. The two following sections show the code for the one-coupling simulations only as they deal with implementing custom hydraulics forces from a steady CFD velocity field. For the two-way coupling, these are not implemented as calculations are performed through the DEM-CFD coupling module. The last two sections apply to both one way and two-way coupling as they deal with hydraulic independent models.

4. 3 Distinguish physical contact and near contact situations

The EDEM platform has the very useful capability to trigger the contact plug-in for distances bigger than the particle radius. In fact, this specific capability allows implementing interfacial forces and near the wall hydraulics in highly dynamic particulate systems. Having a contact detection radius bigger than the physical radius allows actually detecting near collision situations where interfacial forces are significant.

This option was used to implement the DLVO model and drag retardation. The near collision radius was set to be 3 times bigger than the actual radius of the particles, as equations show that it is the distance where retardation factors become significant [48, 83], noting that the bigger the collision detection radius, the more time consuming the simulations.

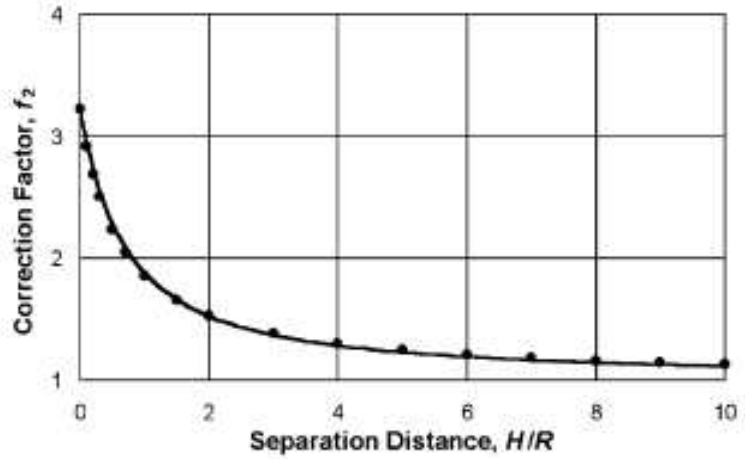

Figure 4.2: Significance of parallel retardation coefficient [83]

The contact model triggers when a particle approaches another object within a distance of less than two times its radius from its surface; it is evaluated whether it is an actual contact or a near contact case, and physical models are applied accordingly.

```
// initialise components of the fluid velocity where the particle stands
      double cfdFieldX, cfdFieldY, cfdFieldZ;

// compute the depth of the near contact shell (in this work 0.5)
      double InteractionShelldepth=elem1ContactCurvature-
elem1PhysicalCurvature;


// will store the physical particle overlap if necessary
      double ContactOverlap;


//initialise the distance between objects surface
      double distance;
      double p=PI;


//edem returns contactPointX, contactPointY, contactPointZ when the plugin is
called
//let's define the associated 3D point for further vector calculations
      CSimple3DPoint  contactPoint(contactPointX, contactPointY,
contactPointZ);

// Defines the unit vector from element 1 to the contact point
      CSimple3DVector unitCPVect = CSimple3DPoint(elem1PosX, elem1PosY,
elem1PosZ)- contactPoint ;
      unitCPVect.normalise();

// Put the values into a more useful form
      CSimple3DVector angVel1(elem1AngVelX, elem1AngVelY, elem1AngVelZ);
      CSimple3DVector angVel2(elem2AngVelX, elem2AngVelY, elem2AngVelZ);


// Clear return values
```

```
      calculatedNormalForceX = 0.0;
      calculatedNormalForceY = 0.0;
      calculatedNormalForceZ = 0.0;
      calculatedUnsymNormalForceX = 0.0;
      calculatedUnsymNormalForceY = 0.0;
      calculatedUnsymNormalForceZ = 0.0;
      calculatedTangentialForceX = 0.0;
      calculatedTangentialForceY = 0.0;
      calculatedTangentialForceZ = 0.0;
      calculatedUnsymTangentialForceX = 0.0;
      calculatedUnsymTangentialForceY = 0.0;
      calculatedUnsymTangentialForceZ = 0.0;
      calculatedElem1AdditionalTorqueX = 0.0;
      calculatedElem1AdditionalTorqueY = 0.0;
      calculatedElem1AdditionalTorqueZ = 0.0;
      calculatedElem1UnsymAdditionalTorqueX = 0.0;
      calculatedElem1UnsymAdditionalTorqueY = 0.0;
      calculatedElem1UnsymAdditionalTorqueZ = 0.0;
      calculatedElem2AdditionalTorqueX = 0.0;
      calculatedElem2AdditionalTorqueY = 0.0;
      calculatedElem2AdditionalTorqueZ = 0.0;
      calculatedElem2UnsymAdditionalTorqueX = 0.0;
      calculatedElem2UnsymAdditionalTorqueY = 0.0;
      calculatedElem2UnsymAdditionalTorqueZ = 0.0;
      calculatedChargeMovedToElem1 = 0.0;


      if (normalOverlap>= InteractionShelldepth){
//normalOverlap is given by edem when the plugin is called
//and is used to compute the contact overlap necessary for the hertz mindlin
model
            ContactOverlap=normalOverlap-InteractionShelldepth;
```

If the overlap that triggers the call of the contact plug-in is bigger than the depth of the near collision shell, set to two radii, it means that there is an overlap between a particle and another object, so the simple Hertz-Mindlin contact model is used. The implementation of this was coded by the DEM-Solutions team.

However, when a near contact situation is detected, the author's alternative plug-ins are called whether there are contact between particles, or between a particle and a wall. The near the wall plug-in adds the retardation associated with wall effect and particle-wall Van-der-Waals interaction. The particle-to-particle contact plug-in will only add particle-particle Van-der-Waals interactions.

4. 4 Hydraulic forces calculated from the steady CFD velocity field

If the overlap that triggers the call of the contact plug-in is such that objects are not physically in contact but at a distance of less than two radii from each other, the hydraulic retardation and DLVO model is implemented.

4. 4. 1 Initializations

In the Lagrangian simulation, a previously computed CFD field is imported to EDEM 3.2 using the field manager add-on, and velocities can be retrieved thanks to:

```
//Get the Fluid Velocity vector for the particle centre
                  if(m_field->queryVectorField(elem1PosX, elem1PosY,
elem1PosZ,8,eIdw,cfdFieldX,cfdFieldY,cfdFieldZ)==false)
                  {
                        cfdFieldX = 0;
                        cfdFieldY = 0;
                        cfdFieldZ = 0;
                  }
```

Then basic operations of the fluid velocity can be done, like computing magnitude, relative velocities and particle Reynolds number.

```
//Fluid Velocity Vector length
      CSimple3DVector cfdField(cfdFieldX,cfdFieldY,cfdFieldZ);
      double Vmag=cfdField.length();

//Relative velocity between the particle and the fluid
      CSimple3DVector particleVelocity(elem1VelX, elem1VelY, elem1VelZ);
      double Umag=particleVelocity.length();
      CSimple3DVector relativeVelocity = cfdField - particleVelocity;

//Equivalent radius of particle (assuming spherical)
      double nRadius = elem1PhysicalCurvature;
      double radius=nRadius;
      double rp=radius;

//cross sectional area of particle
      double ProjArea =  PI * radius * radius;

//Local Reynolds number
      double re = m_density_fluid * relativeVelocity.length() * 2.0 * radius
/ m_viscosity;
```

4. 4. 2 Near wall hydraulic retardation

In order to compute the near the wall hydraulic retardation, a description of the system in the local geometry coordinates is needed. This part implements the decomposition of the 3D-vector of the particle velocity into the wall's local reference frame. The vector normal to the surface at the contact point is already known. Therefore, we can define an orthogonal base by choosing any pair of vectors orthogonal with each other and the normal one. The coordinate of the velocity vector in this new base is then defined by its projection on the vector normal to the surface and its projection on the plane tangential to the surface, as illustrated in Figure 3.3 (reproduced here from the previous chapter for clarity).

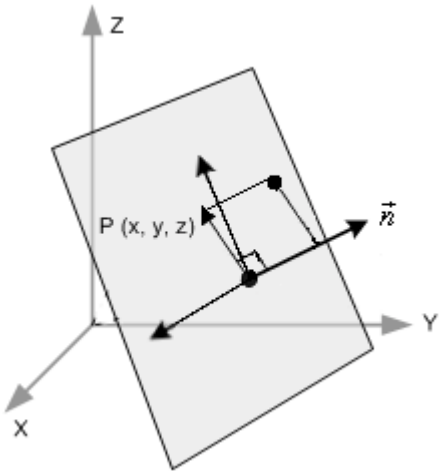

Figure 3.3: Principles of 3D projection

Any vector whose scalar product with the vector normal to the surface of coordinate (x, y, z) is zero, is orthogonal to it. The simplest way to choose such vector is to take $(0, -z, y)$:

```
// First Orthogonal vector to unitCPVect
CSimple3DVector RadialyTangentToSurface(0,-unitCPVect.dz(),unitCPVect.dy());

RadialyTangentToSurface.normalise();
```

Then the local base can be completed by taking the cross product of these two vectors.

```
// Cross product of normal vector and first orthogonal vector
CSimple3DVector AxialyTangentToSurface =
unitCPVect.cross(RadialyTangentToSurface);

AxialyTangentToSurface.normalise();
```

The velocity vectors expressed in the global reference frame should then be converted in the local base.

```
// Calculate the transformation matrix form canonical basis to contact point
coordinate system
```

```
CSimple3x3Matrix
Trans=CSimple3x3Matrix(unitCPVect,RadialyTangentToSurface,AxialyTangentToSurf
ace);

// and its inverse
CSimple3x3Matrix InvT=Trans.inv();

// compute the velocity vectors in the new base
CSimple3DVector U=cfdField*InvT;
CSimple3DVector V=particleVelocity*InvT;
```

The implementation of the free-stream drag model, i.e. further away from obstacles, is a special case of the retardation models presented here with factors set equal to one. It merely corresponds to implementing Eq. 3.5.

$$F_D = \frac{12u^2\rho A_p}{\mathrm{Re}_p} = \frac{12uA_p\mu}{D_p} = 6r_p\pi\mu.u = 3u\pi D_p\mu$$

Eq. 3.5

```
//    Bulk flow Drag force calculation
double eta = 6*p*m_viscosity*radius;
CSimple3DVector BulkDrag=relativeVelocity*eta;
double BDL=BulkDrag.length();
```

It is implemented in an External Force plug-in at step 4 of Figure 4.1 and triggers for every particle at every time step independently of contact detections. The near the wall plug-in will therefore only superimpose the added retardation associated with wall effect and particle wall Van-der-Waals interaction.

The retarded drag is then calculated from the velocity vectors components in the new local contact point base. Retardation coefficients are functions of the inter-surface separation distance *h*

```
// relative surface to surface distance
h=InteractionShelldepth-normalOverlap+rp;

// when particles overlap objects
double hovera=h/radius;

//if there is overlap, the dimensionless distance is set to 1
if  (hovera<=1){  hovera=1;}
```

1. 4. 2. i Particle impinging orthogonally on a rigid wall

$$F_{D\perp} = -6\pi\mu.aV_n.\lambda_\perp + 6\pi\mu.aU_n.f_2$$

Eq. 3.9

In the modified Stokes law, Eq. 3.8, the drag force is composed of the sum of two terms. The presence of a nearby wall is accounted for by the introduction of retardation factors λ_t and f_2 which are approximated by analytical expressions given in Eq. 3.13.

Normal particle velocity, V_n, normal to the wall, is affected by the retardation factor λ_t

$$\lambda_{\perp} = \left[1+(a/h)^{p}\right]^{1/p}$$

With p=0.89.

```
//retardation function for the particle
double Lambdao= pow(1.0+pow(1/hovera,0.89),1/0.89);

//Vn is the components of the orthogonal projections of the particle velocity
vector on the axis normal to the surface
double Vn=V.dx();

//particle velocity component of the retarded normal drag force
double Fnp=-Vn*Lambdao*eta;
```

Moreover, the liquid velocity component, U_n, at the centre of the particle, is affected by coefficient f_2.

$$f_2 = \frac{2.022+h/a}{0.626+h/a}$$

```
//retardation function for the fluid
double f2=(2.022+hovera)/(0.626+hovera);

//Un is the components of the orthogonal projections of the fluid velocity on
the axis normal to the surface
double Un=U.dx();

//fluid velocity component of the retarded normal drag force
double Fnf=Un*f2*eta;
```

The total retarded normal drag force is the sum of both contributions.

```
double FN=(Fnp+Fnf)
```

1. 4. 2. ii Translational and rotational motion of a sphere parallel to a rigid wall

The drag force retarded by a longitudinal wall can also be expressed as the sum of these two contributions:

$$F_{D//} = F_{1//} + F_{2//} = -6\pi\mu.aV.\lambda_{//} + 6\pi\mu.aU.f_3$$

The asymptotic drag retardation is a function of the surface-to-surface distance delta.

```
double delta=InteractionShelldepth-normalOverlap;
```

The retardation function, for amnon-rotating sphere near a plane in a static fluid, Eq. 3.14,

$$\lambda_{//} \approx \frac{8}{15}\ln(\delta / a) - 0.9588$$

Eq. 3.14

Should be applied to both particle velocity components tangential to the surface

```
double Vat=V.dz();
double Vrt=V.dy();
// Vat and Vrt are the components of the orthogonal
// projection of the particle velocity vector in the tangent plane

double deltat=-8/15*log(delta/radius)+0.9588;

CSimple3DVector Ft= CSimple3DVector(0,-Vrt*deltat,-Vat*deltat);
```

To which should be superimposed the force induced by a linear shearing flow past an immobilized sphere near a rigid wall, where the retardation factor is approximated by, equation Eq. 3.15

$$f_3 = 1 + \frac{9}{16}\frac{a}{h}$$

Eq. 3.15

This should also be applied to both components of the fluid velocity that are tangential to the surface.

```
double Uat=U.dz();
double Urt=U.dy();
// Vat and Vrt are the components of the orthogonal
// projection of the fluid velocity vector in the tangent plane

double f3=1+9/(16* hovera);

CSimple3DVector Fs= CSimple3DVector(0,Urt*f3,Uat*f3);
```

The resulting drag force, $F_{D//}$, that is the sum of this two components, then corresponds to a non-rotating solid particle flowing along a much larger solid surface with non-slip boundary conditions at low Reynolds numbers.

```
CSimple3DVector FT=(Fs+Ft)*eta;
```

The final retarded drag coefficient is the vector sum of all contributions:

```
// retarded drag expressed in the contact point coordinate
CSimple3DVector RetardedDrag= CSimple3DVector(FN,FT.dy(),FT.dz());
```

We then have to convert this result back into the global reference frame:

```
// retarded drag expressed in the canonical system
RetardedDrag=RetardedDrag*Trans;
```

The additional drag due to retardation is then computed from:

```
CSimple3DVector ExtraDrag=RetardedDrag-BulkDrag;
```

The calculated extra drag is not added to the total force vector just yet, as it will be further affected if Brownian motion is considered.

4. 4. 3 Lift model

A constant shear rate is assumed over the particle diameter [48], so the local shear rate can be approximated by evaluating fluid velocities at the particle surface near and far from the wall:

```
// fluid velocity value at particle surface near the wall
                  CSimple3DPoint  PointWall(elem1PosX-rp*unitCPVect.dx() ,
elem1PosY-rp*unitCPVect.dy(), elem1PosZ-rp*unitCPVect.dz());
                  double VwallX, VwallY, VwallZ;
                  double K_viscosity=m_viscosity/m_density_fluid;
                  if(m_field->queryVectorField(PointWall.x(), PointWall.y(),
PointWall.z(),8,eIdw,VwallX, VwallY, VwallZ)==false)
                  {
                        VwallX=0;
                        VwallY=0;
                        VwallZ=0;
                  }
                  CSimple3DVector Vwall(VwallX, VwallY, VwallZ);
                  Vwall=Vwall*InvT;
                  Vwall.setdx(0);
                  double TangentVwallMag=Vwall.length();

// fluid velocity value at particle surface away from the wall
                  CSimple3DPoint  PointOut(elem1PosX+rp*unitCPVect.dx() ,
elem1PosY+rp*unitCPVect.dy(), elem1PosZ+rp*unitCPVect.dz());
                  double VoutX, VoutY, VoutZ;
                  if(m_field->queryVectorField(PointOut.x(), PointOut.y(),
PointOut.z(),8,eIdw,VoutX, VoutY, VoutZ)==false)
                  {
                        VoutX=0;
                        VoutY=0;
                        VoutZ=0;
                  }
                  CSimple3DVector Vout(VoutX, VoutY, VoutZ);
                  Vout=Vout*InvT;
                  Vout.setdx(0);
                  double TangentVoutMag=Vout.length();
```

and using them to linearly approximate the velocity gradient over the particle diameter.

```
// linear approximation of the velocity gradient accross the particle region
                  double DVoverDn=(TangentVoutMag-TangentVwallMag)/(2*rp);
```

And applying Eq. 3.7.

The Saffman lift force, Eq. 3.7, can then be implemented in the direction normal to the wall

$$F_{SL} = 0.25.C.D_p^2.\rho_f \left(u_f - u_p\right)\sqrt{\nu \frac{\partial u_f}{\partial n}} \; with \quad C = 6.46$$

Eq. 3.7

```
// velocity gradient induced lift
CSimple3DVector
lift=unitCPVect*6.46*m_density_fluid*relativeVelocity.length()*sqrt(K_viscosi
ty*abs(DVoverDn))*pow(radius,2.);

                  calculatedForceX += lift.dx();
                  calculatedForceY += lift.dy();
                  calculatedForceZ += lift.dz();
```

Provided that:

$$\mathrm{Re}_p << \mathrm{Re}_G^{1/2} \quad \mathrm{Re}_G = \frac{GD_p^2}{\nu}$$

Where in Cartesian coordinates $G = \sqrt{\left(\frac{\partial u}{\partial z}\right)^2 + \left(\frac{\partial v}{\partial z}\right)^2}$

4. 5 Brownian motion and diffusion

Sub-micron sized particles are subject to forces arising from Brownian motion, and the local Stokes' drag force must be corrected for this by a Cunningham factor [93], that has for expression:

$$\mathrm{F}_D^{\mathrm{sub}} = F_D^{ret} / C_C \text{ where } C_C = 1 + \frac{2\lambda}{d}\left(1.2571 + 0.4e^{-0.55d/\lambda}\right)$$

Eq. 3.18

The force F_D^{ret} is the usual drag force including the hydraulic retardation and λ is the molecular mean free path as defined in Eq. 3.18

```
double Kb=1.381e-23;   // (J/K) boltzman constant
double T=300; //K
double mass=elem1Mass;
double Diameter=rp*2;
double tau=mass/eta;          // relaxation time
double u=sqrt(Kb*T/mass);     //mean thermal velocity
double l=tau*u;               //molecular mean free path of the surounding
medium
double   Cc=1+2*l/Diameter*(1.2571+0.4*exp(-0.55*Diameter/l));//   Cunningham
factor
```

The Brownian force components are independent white noise processes. Three independent Gaussian random numbers (Gi) of zero mean and unit variances are generated [108], each corresponding to one component of the random force. As described in and Eq. 3.21

```
if (bm=='y'){ //if Brownian motion enabled
// the cunningam correction factor should be considered
ExtraDrag *= 1/Cc;

// along with the brownian force
// generate 3 independent Gaussian random numbers with zero mean and unit
variance.
G1 = gasdev(1);
G2 = gasdev(1);
G3 = gasdev(1);

S=2*Kb*T*eta/Cc/pi;
F=sqrt(pi*S/timestep);
Nx=G1*F;
Ny=G2*F;
Nz=G3*F;

calculatedForceX += Nx;
calculatedForceY += Ny;
calculatedForceZ += Nz;

}
```

The random number generator here is called `gasdev(1);` it generates random number distributed as showed in Figure 3.5. One can use any reliable generator here instead, provided it generates Gaussian random numbers with zero mean and unit variance.

Now the calculated extra drag can be added to the total force vector, in case of one way coupling simulation.

```
calculatedForceX += ExtraDrag.dx();
calculatedForceY += ExtraDrag.dy();
calculatedForceZ += ExtraDrag.dz();
```

4. 6 Van-der-Waals forces

The Van-der-Waals force between two surfaces immersed in a fluid medium depends on the Hamaker constant wich is usually taken between 1e-20 and 2e-20:

```
double A=1.5e-20;                    //% Hammaker constant (J)
```

For two interacting spherical particles of same radius a, the Van-der-Waals force expression is given by Eq. 3.24.

$$f_{spheres}^{equal} = A.\frac{32}{3}.\frac{a^6}{\delta^2.(2a+\delta)^3(4a+\delta)^2}$$

Eq. 3.24

Magnetic retardation effects should also be included as a multiplying factor in the Van der Waals force expression [99]:

$$f_m = \frac{\lambda(\lambda + 22.24.\delta)}{(\lambda + 11.12.\delta)^2}$$

Eq. 3.27

```
D=delta;
double Lambda=1e-7;                          //%characteristic wave length (L)
double
Fmagnetic_Retardation=Lambda*(Lambda+22.24*D)/pow(Lambda+11.116*D,2.0);
```

In the particle-to-wall contact plug-in, only interaction between a spherical particle and a flat plate is considered, which is

$$f_{plate}^{sphere} = \frac{2.A.a^3}{3.(h^2 - a^2)^2}$$

Eq. 3.25

```
double Flvdw=2/3*A*rp*rp*rp/((h*h-rp*rp)* (h*h-rp*rp))*Fmagnetic_Retardation;
```

The limiting values of the Van-der-Waals force

```
if (Flvdw >= Max_vdw){
Flvdw == Max_vdw;}
else if (Flvdw < 0){
Flvdw == 0;}
```

The Van-der-Waals force applies in direction of the contact vector.

```
CSimple3DVector Flvdw_vector=-unitCPVect*Flvdw;

calculatedForceX += Flvdw_vector.dx();
calculatedForceY += Flvdw_vector.dy();
calculatedForceZ += Flvdw_vector.dz();
```

4. 7 A few limitations

In order to lower the computational cost of simulations, particles are created within an inlet control window that EDEM users call a particle factory. In this work, following the limiting trajectory model [12], particles outside of such an inlet window are expected to have

negligible impact on the simulation results, meaning that particles injected further way from the wall would not contribute to the deposition process. This is a reasonable assumption when the particle concentration is low enough not to form significantly big clusters, with regard to the system geometry; however, for big particle concentrations this assumption becomes invalid.

The current version of the EDEM software does not give the possibility to perform systematic analysis of the size distribution of the particle clusters as a function of either time or space. Such a feature would however be useful in order to support visual observations.

Regarding the implementation of the particle mechanics immersed in water, the model described does not include hydraulic retardation between particles (as opposed to between particles and boundaries), which would be required for high particle concentrations. Furthermore, inter-particles retardation effects is a very a very complex subject [76] that would require its own research project to be incorporated into DEM framework. By decreasing particles velocity near obstacles, retardation effects can be considered as an important deposition mechanism, and therefore it would be expected that including inter-particle retardation effects would increase the simulated deposition. The implementation of surface interaction, surface roughness and heterogeneity has not been taken into account, although it has been argued to have significant effect on particle deposition [6, 109].

CHAPTER 5: Validation

5. 1 Introduction

Many earlier studies that include interfacial physics report using model equations without expanding on how their authors made sure that models were implemented correctly [6, 16, 23, 93, 103]. It was therefore challenging to make sure that the models are doing what there are supposed to do at the particle level. Finding simple enough comparison material has been a challenge and the lack of particle size physical experiment compelled to turn towards other simulation study for model verification. For this reason, only orthogonal retardation model and Van-der-Waals force models could be validated.

5. 2 Hydraulic retardation

5. 2. 1 Meso-scale validation of orthogonal retardation

In order to easily implement retardation equations and validate near the wall simulations, a meso-scale viscometer setup was simulated where a one-millimetre diameter particle of density 2 g/cm³ immersed in a fluid falls along a vertical wall from 5cm height. Figure 5.1 presents the differences induced by the parallel and orthogonal components of the drag retardation when the particle is in the neighbourhood of a wall. Free fall and free-stream equations of motions being well known basic descriptions, results from retarded simulations will be compared against them.

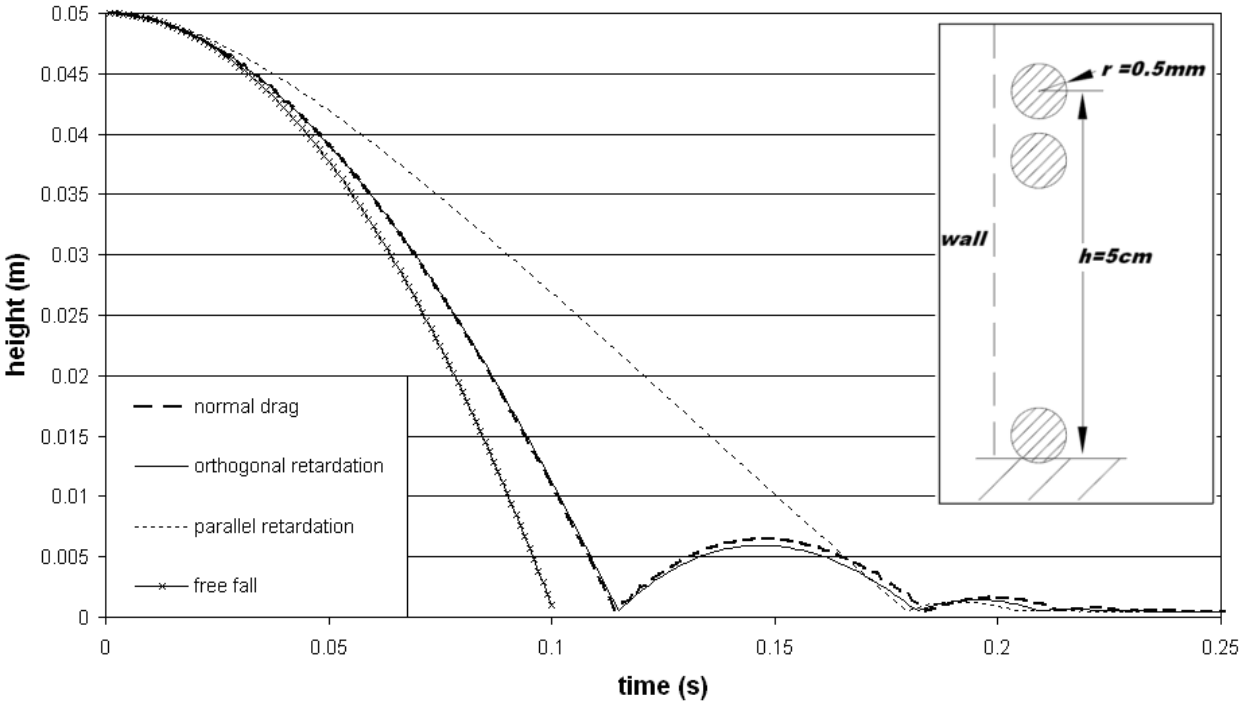

Figure 5.1: Viscometer simulations

Free Fall:

Describes the motion of a small particle only subjected to gravity, from classic mechanics analytical expression. It has been represented in order to compare with the motion with normal drag.

Motion equation for free fall: $\ddot{y} = -g$

Normal drag:

Describes the bouncing motion of a small particle subjected to the common drag described in 3. 3. 1, the bouncing motion have only been represented in order to show the difference induced by the orthogonal retardation as the coefficient of restitution of such micro particle immersed in fluid is still unknown [44].

Motion equation considering free-stream drag: $\ddot{y} = -\frac{g}{m} + 3v\pi D_p \mu$

Parallel retardation:

The particle is separated by half a radius from the wall. The parallel retardation acts all the way down to the horizontal plate. So the trajectory deviate a lot from the normal drag as at each time-step the added retardation drag prevent the particle from accelerating. In real life, the particle would be pushed away from the wall and seek a path of least resistance through rotational lift.

Orthogonal retardation:

The orthogonal retardation appears to have only small impact, relatively to the parallel retardation because in that case, it only acts within a few radius of the horizontal wall.

5. 2. 2 Micro-scale validation of orthogonal retardation

In order to validate the model at the scale used in this work, the orthogonal particle wall interaction has been compared to the work from Chein and Liao [87], who computed near the wall particle trajectories in quiescent viscous fluid using a Lagrangian approach. In their work, they used dimensionless equations. So for the sake of comparison, let us do the same.

When considering non-Brownian particle, not subject to colloidal forces, in a quiescent fluid, the particle equation of motion (Eq. 3.2) simplifies as:

$$m_p \frac{du_p}{dt} = F_a + F_D + F_G$$

$$m_p \frac{du_p}{dt} = -\frac{1}{2} m_f \frac{du_p}{dt} - \lambda(x).\xi.u_p + \left(m_p - m_f\right).g$$

$$\left(m_p + \frac{1}{2} m_f\right) \frac{du_p}{dt} = \left(m_p - m_f\right).g - \lambda(x).\xi.u_p$$

Eq. 5.1

Note that the added mass was considered here for validation only as Chein and Liao considered it as being half of the displaced fluid weight. Also let us remember the friction coefficient $\xi = 6.\pi.\mu.r_p$, and $\lambda(X)$ the orthogonal retardation coefficient. Eq. 5.1 nondimentionalizes in the following way first let us divide everything by $\left(m_p - m_f\right).g$ and neutralise the velocity dimension:

$$\frac{m_p + \frac{1}{2} m_f}{\left(m_p - m_f\right).g} \frac{du_p}{dt} = 1 - \frac{\lambda(x).\xi.u_p}{\left(m_p - m_f\right).g}$$

Introducing the stationary falling velocity $u_\infty = \frac{m_p - m_f}{\xi} g$, Eq. 5.1 becomes:

$$\frac{m_p + \frac{1}{2} m_f}{\xi} \frac{d}{dt} \frac{u_p}{u_\infty} = 1 - \lambda(x) . \frac{.u_p}{u_\infty}$$

Now let us introduce $U = \frac{.u_p}{u_\infty}$, and normalise the time dimension, by introducing $T = \frac{t}{\tau_p}$

so that $dt = \tau_p . dT$. This leads to:

$$\frac{m_p + \frac{1}{2} m_f}{\xi . \tau_p} \frac{dU}{dT} = 1 - \lambda(x) . U$$

Posing $\tau_p = \frac{m_p + \frac{1}{2} m_f}{\xi}$, the dimensionless force balance finally becomes

$$\frac{dU}{dT} = 1 - \lambda(x) . U$$

Let u define the dimensionless length as $X = \frac{x}{r_p}$, so $U = \frac{dx}{u_\infty . dt} = \frac{dx}{u_\infty . \tau_p . dT} = \frac{r_p}{u_\infty . \tau_p} \frac{dX}{dT}$.

The dimensionless factor q was defined as $q = \frac{r_p}{u_\infty . \tau_p}$, which is proportional to the inverse of the particle radius cubed, so that the dimensionless equations of motion become:

$$\begin{cases} \frac{dU}{dT} = 1 - \lambda(x) . U \\ \frac{dX}{dT} = q^{-1} . U \end{cases}$$

Eq. 5.2

We use the same initial conditions described in Chein and Liao's [87] work ($X_0 = 10$ and $V_0 = \lambda^{-1}(X_0) \approx 0.873$, and repeat the viscometer experiment at micro-scale, with a one micron radius particle that impinges orthogonally to a wall. Results are plotted in Figure 5.2.

By displaying the phase portrait of the particle motion when it is subjected to retardation and when the particle is not subjected to retardation, the graph shows the effect of the

retardation model implementation. It can be seen that without retardation, the particle quickly reaches its terminal velocity. However, when subjected to the wall retardation effects, it decelerates approaching the wall as the retardation coefficient increases. In this aspect, near the wall retardation is part of the mechanism of deposition as the particle velocity tends toward zero when approaching the wall. This means that near the wall particles will tend to stay immobile.

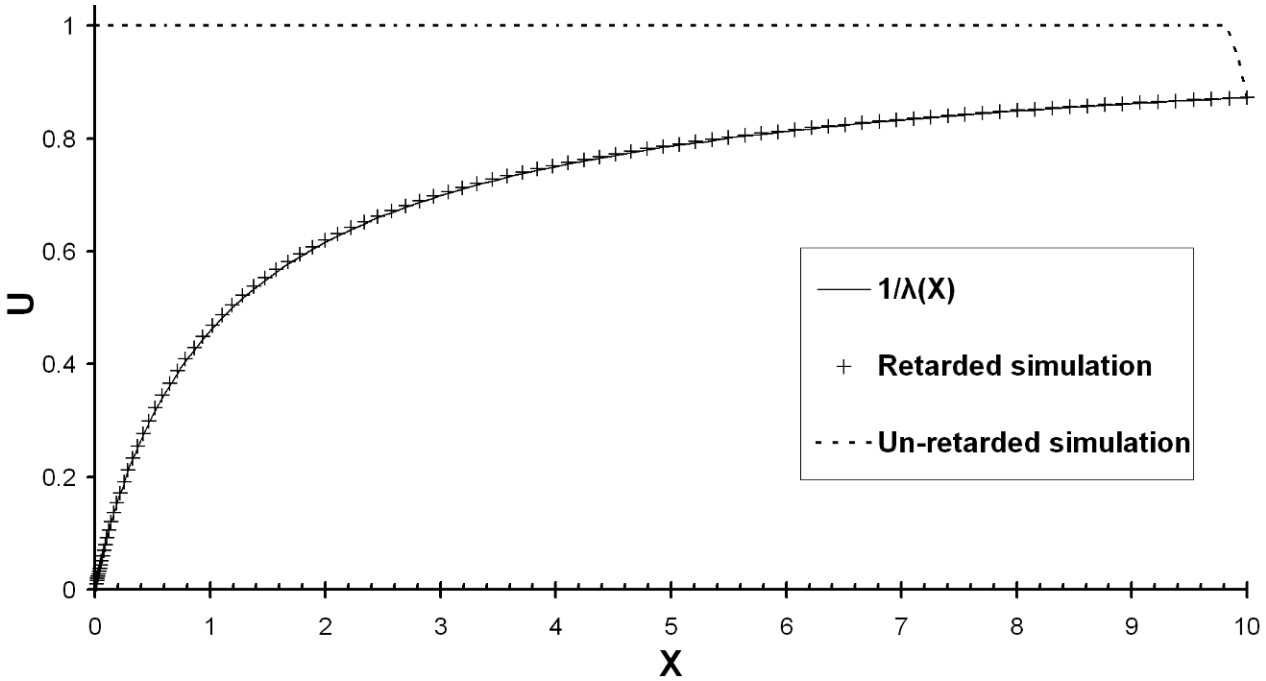

Figure 5.2: Micro-viscometer simulations

Chein and Liao observed that small particles (i.e. for large q), $V(x)$ asymptotically approaches $\lambda^{-1}(X)$, the inverse of the orthogonal retardation coefficient. In the current simulation with a one micron radius particle, q=34692.8 and the phase portrait overlaps the $\lambda^{-1}(X)$ curve as displayed in Figure 5.2, so the results are consistent with Chein and Liao's observation.

5. 3 Van-der-Waals force

The Van-der-Waals model used in this work is compared to Chein and Liao's [87] work in the form of the ratios of VDW forces to gravity force as a function of separation distance, Figure 5.3. It can be observed that the relative strength of Van-der-Waals attraction with

respect to gravitation is smaller for bigger particles, which implies that bigger particles are less subjected to Van-der-Waals forces.

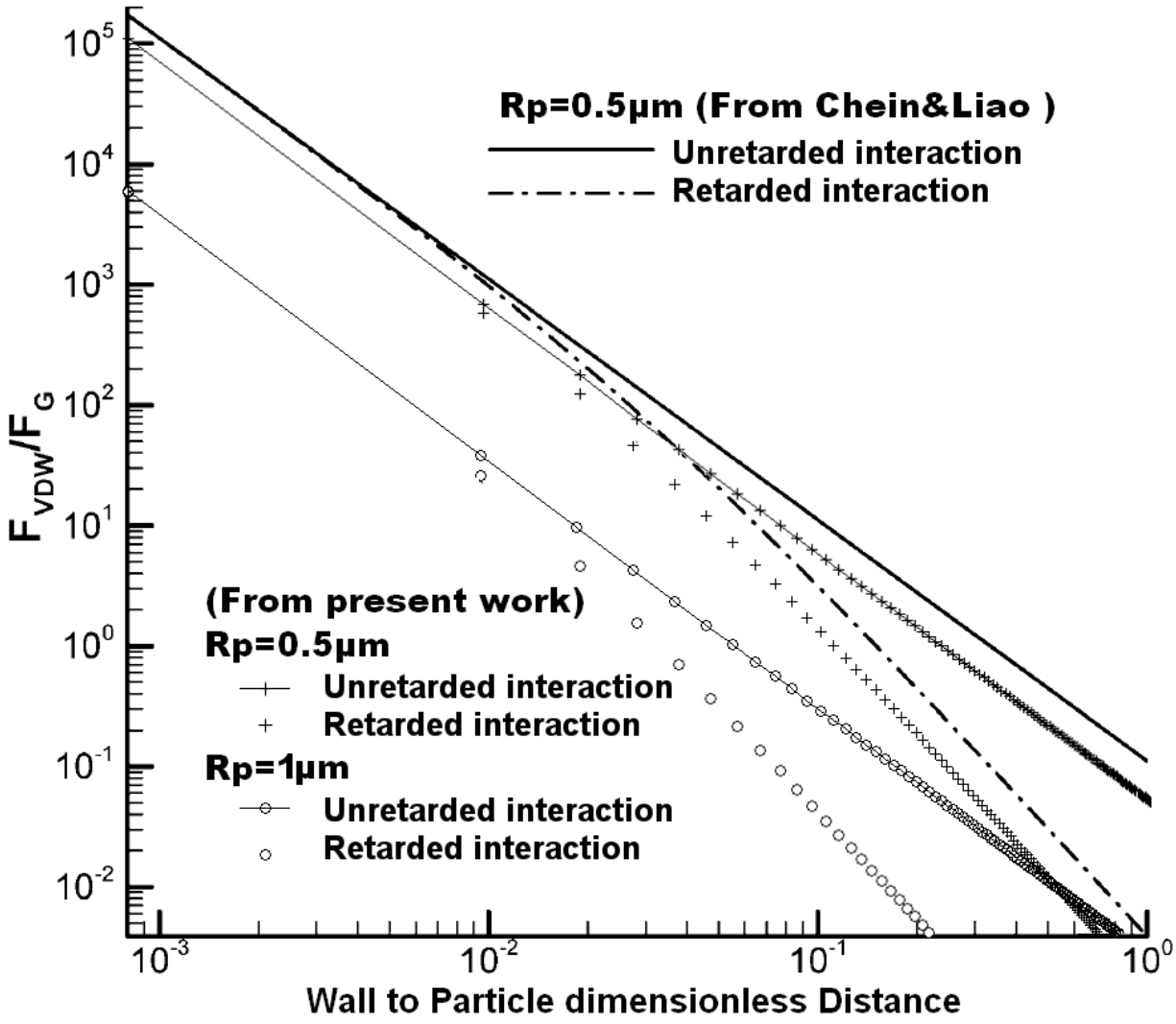

Figure 5.3: Attractive Van-der-Waals force

Particle and physical parameters have been modified to concord with the ones used in their work. However, the VDW Equation as implemented in this work uses the equations derived in the Appendix A, which gives a VDW force between a plate and a particle half as big as the one used in Chein and Liao's work, which accounts for the difference observed for a particle of radius 0.5microns. Many articles use different forms of VDW model equations [95, 99, 101] and this multiplying factor two is a repeating inconsistency of the application of VDW force in past studies. This inconsistency triggered the need to derive a proof of the general equation of the VDW forces in Appendix A that can be relied on and provide a reason for the choice of the equation used in this work. Chein and Liao's work uses a model equation term by term similar to the one used in this work if not for this factor two. That accounts for the

difference in results in Figure 5.3, and it can be seen that results would be equal if the model equation implemented was the same as in Chein and Liao's work.

5. 4 Concluding remarks

Validation work has been carried out by comparing the simulation method and force models presented in previous chapter against analytical results and published results from Chein and Liao. Both VDW model and orthogonal retardation model provide a qualitative agreement with the reported work of Chein and Liao. Results appear to be coherent with their observation and consistent with theoretical considerations; eventual discrepancies have been accounted for. The physical models implemented as described in previous chapters appear to compare well against expected results obtained from formal analysis and published work, they will therefore be used in the simulations described in the next chapters.

CHAPTER 6: Using DEM-CFD method to predict Brownian particles deposition in a constricted tube

6. 1 Introduction

Aggregation and deposition of particulate colloids (particle size between 1μm and 5μm diameter) on a solid surface is of great importance in many industrial processes such as micro-contamination control of microelectronics, membrane filtration, fouling of heat exchangers and surface deposition in micro-fluidic devices. In nature, micro-particle deposition is of great interest in microbial pathogen removal through natural granular filtration of surface water. Deposition of inert colloids is also significant in water disinfection, since microbes and inert colloids exhibit important similarities in saturated porous granular media, as stated by Johnson et al [25], who observed that hydrodynamic drag mitigates deposition and drives re-entrainment of both biological and non-biological colloids.

The DEM approach has been successfully applied by Peng et al. [110] who developed a 2D in house DEM-based model to simulate nano-particle aggregation in a quiescent suspension influenced by an external alternating electrical field, over a broad pH range. Random Brownian diffusion and dielectrophoresis physics were implemented along with the standard DLVO forces. This chapter represents an attempt to extend such a procedure to a 3D particle-laden flow, also called a suspension, flowing through constricted tubes. The deposition in a filter bed can be linked to the deposition in a constricted tube through the approximate number of constricted tubes per unit area of filter. In order to model the solid-fluid system, DEM computation was coupled with Computational Fluid Dynamics (CFD). More generally, the DEM technique allows the consideration of the influence of external force fields by a using data map of the force field. Independently, DEM also considers boundary-particle and particle-particle interactions, enabling the modelling of surface and interfacial forces. The force contribution of each interaction is added to the force balance and the equation of motion of each particle and then integrated [111].

Yoshida and Tien [112] experimentally studied the deposition of particles in a granular filter bed using sinusoidal constricted tubes. They plotted collection efficiency (that is the ratio between the amount of particles deposited and the number of particles injected) against the

wall deposit concentration, in order to study re-entrainment, which was found to be a monotonic function of the extent of deposition. It was also stated that past a threshold wall concentration, a filter bed becomes non-retentive for particles equal to or less than 0.1μm. On the other hand, Marshall [113] reported the importance in the deposition process of particle-particle interaction (particle size exclusion combined with inter-particle DLVO interaction) by showing that aerosol channels with previously deposited particles and agglomerates had a higher capture rate of incoming particles. Bigger deposited agglomerates increase floc re-suspension [15]. Therefore, particle-particle interactions in a flowing fluid are shown to be as critical as surface interaction. Results presented in the present work will demonstrate that this conclusion is also true in hydrosols.

In order to simulate Brownian particle retention in the pore structure of a filter bed, Chang et al. [23] used a Brownian dynamics simulation of a constricted tube model. Particle diameter varied from 0.5 to 2 microns. They plotted the collection efficiency against the Reynolds number for different tube geometries. Like Johnson et al [7, 22, 25], they also encountered difficulty predicting deposition efficiency when the wall and the particles have similar surface charges (non-favourable conditions) which demonstrates the challenge faced when dealing with a secondary energy minimum. For this reason, in the first instance, the present work will only consider favourable deposition conditions, where surface charges are not hindering deposition.

Of particular interest are results reported by Chang et al [16], who observed lump particle deposition occurring before the constriction; they used analytical equations of the fluid streamlines and reported to have solved numerically the Langevin equation to derive each particle trajectory; the contact model was not explained. However, their results show the main deposition to occur immediately before the constriction in the tube, where the fluid flow is accelerating. This does not seem likely to be physically accurate. These authors also discovered that the inclusion of Brownian forces resulted in lower collection efficiencies.

6. 2 Definition of constricted tube geometry

The constricted tube geometry is used as a three-dimensional colloidal particle-tracking model that predicts colloid retention in porous media in favourable retention conditions (i.e. no electrostatic energy barrier). The geometry of the tube constriction and the inlet fluid conditions imposed define the flow field that is computed with CFD.

For comparison purposes, the constricted tube geometry used in this work corresponds to the parabolic constricted tube (PCT) described by Chang et al [16, 23] who used latex particles of density similar to water.

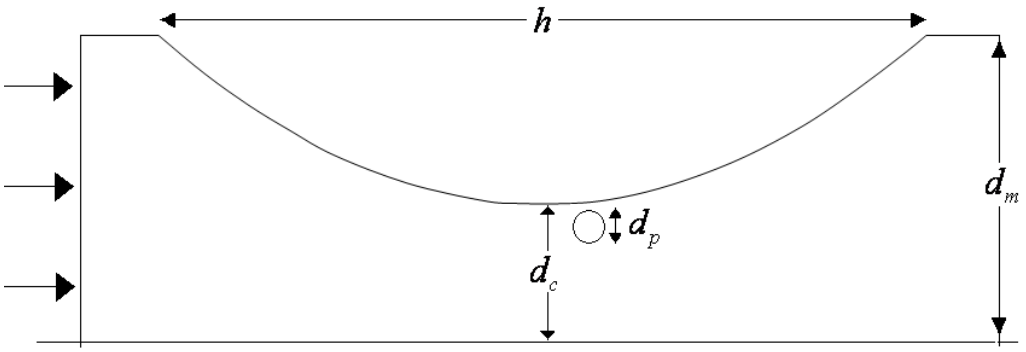

Figure 6.1: Parabolic Constricted Tube parameters definition

Parameter	Value
H	100μm
d_P	1μm - 2μm
d_C	36μm
d_m	80μm

Table 6.1: Geometrical parameters of the parabolic constricted tube

6. 3 Model implementation

Although analytical solutions exist for flow fields inside constricted tube of regular geometries, this might not be the case for other system configurations, and therefore computational fluid dynamics (CFD) was used to derive the flow field. The commercial software Fluent 12.0 has been used to solve the steady-state Navier-Stokes equations under laminar flow hydrodynamics (Eq. 2.7 and Eq. 2.8). The mesh was created to ensure residual convergence and stability. Because of the axi-symmetric nature of the constricted tube, and in order to save computational time, simulations were carried out for only a tenth sector of the tube Figure 6.2.

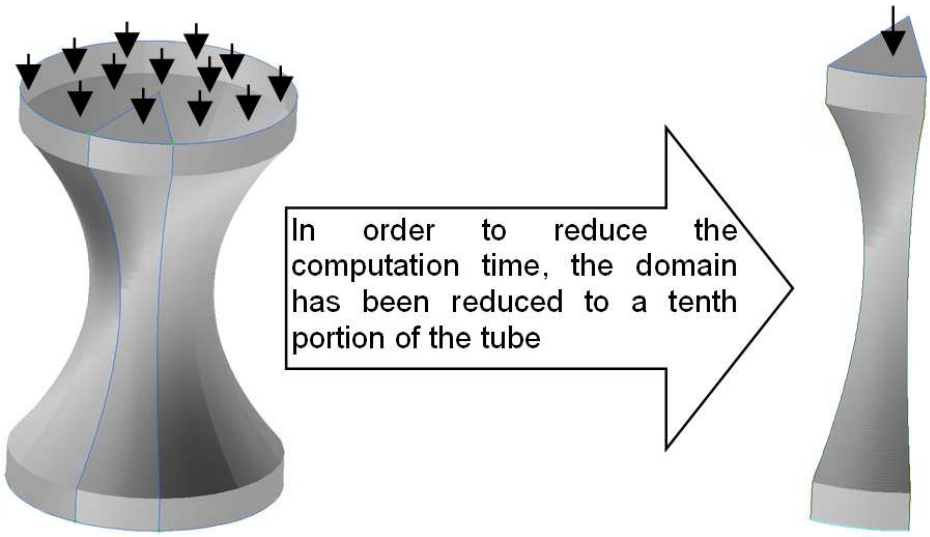

Figure 6.2: Reduction of the computational domain

Boundary conditions for both one-way and two-way implementations of the model include no-slip boundaries at the tube wall surface, symmetry boundaries on both lateral boundaries of the slice and a predefined velocity inlet at the cell entry.

The CFD mesh, consisting of hexahedral elements, had to be modified and significantly coarsened for the two-way coupling simulation compared to the mesh used for the one way coupling. The mesh size was reduced from 331330 elements for the one-way coupling simulation to 17820 elements for the two-way coupling simulation, because DEM-CFD two-way coupling imposes the CFD mesh cells to be at least two times as big as the particles considered. In addition, the time dependence of the two-way coupling imposes the cfd mesh not to be minimised in order to keep reasonable simulation time. The computed undisturbed velocity field was however not affected, as shown in Figure 6.3.

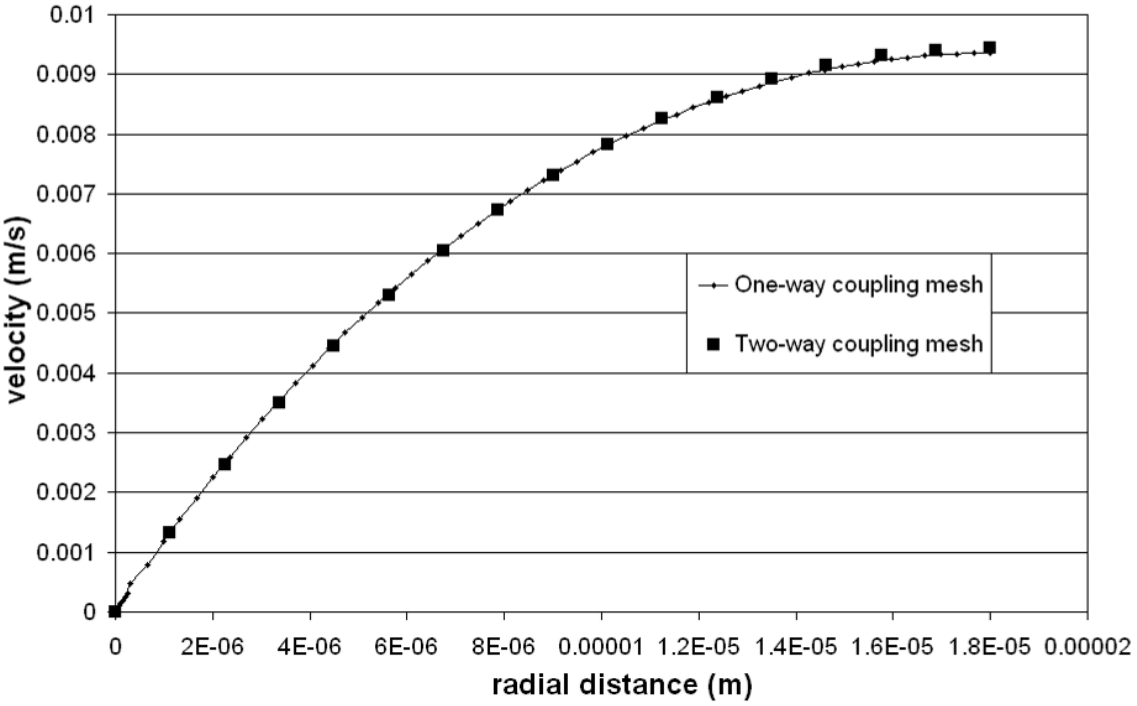

Figure 6.3: Axial velocity at tube constriction

Particles were created within an inlet control window of width y_0=5E-6m (Figure 6.4), which stretches along the wall of the tube. Following the limiting trajectory model [12], particles injected further way from the wall would not contribute to the deposition process.

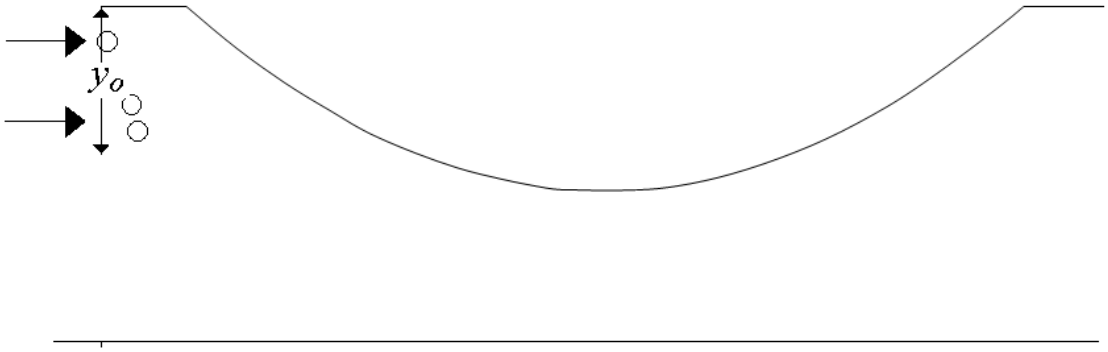

Figure 6.4: Particle inlet window

Particles were randomly created one by one following a uniform distribution over the control window surface and the inlet particle concentration was tuned through the Particle creation rate Γ_{in} ranging from 5.10^3 $particles/s$ to 1.10^5 $particles/s$.

The simulation parameters common to all tested configurations are presented in Table 6.2.

Parameter	Value
Boltzmann constant k_B	1.381e-23 J/K
Temperature T	300 K
characteristic wave length λ	1e-7 m
Hamaker constant $H = n^2 \lambda \pi^2$	1.5e-20 J
Water dynamic viscosity μ	1e-3 kg.s/m
Density of particle ρ_P	1e3 kg/m^3

Table 6.2: Simulation parameters

6. 4 Results and discussion

Specific configuration parameters concerning particle radius, inlet particle concentration and velocity inlet are summed up in Table 6.3 and unless stated otherwise, results apply to one way coupling simulations.

Configurations are numbered from 1 to 4 and will often be referred to by an alphanumeric description of their parameters. For instance, R1c5e3V001 refers to the configuration that involves particles of radius 1 micron at inlet concentration 5000 and velocity inlet 1cm/s. Parameters were chosen to be consistent with the work from Chang [16, 23] and Johnson et al [7, 22, 25].

	Configurations			
Particle radius (micron)	1	1	1	0.5
Inlet concentration (particle/s)	5000	2000	10000	50000
Velocity inlet (mm/s)	10	10	20	10
number of simulations	4	4	5	3
	1: R1c5e3V001	2: R1c2e3V001	3: R1c1e4V002	4: R05c5e4V001

Table 6.3: Configuration parameters

The particle deposition results obtained from the numerical model with the simulation procedures described in CHAPTER 3:, meaning with the purely attractive Van-der-Waals interaction energy curves, retarded drag, Brownian forces, lift force are given in Figure 6.5, which includes the highest and lowest collection efficiency, the mean collection efficiency for each configurations and the standard deviation. It clearly shows that configurations with highest collection efficiency also have the highest results. The variability between different runs of a same configuration is due to both the random particle generation and the randomness of cluster formation and re-suspension, which will be explained in details in section 6. 4. 7.

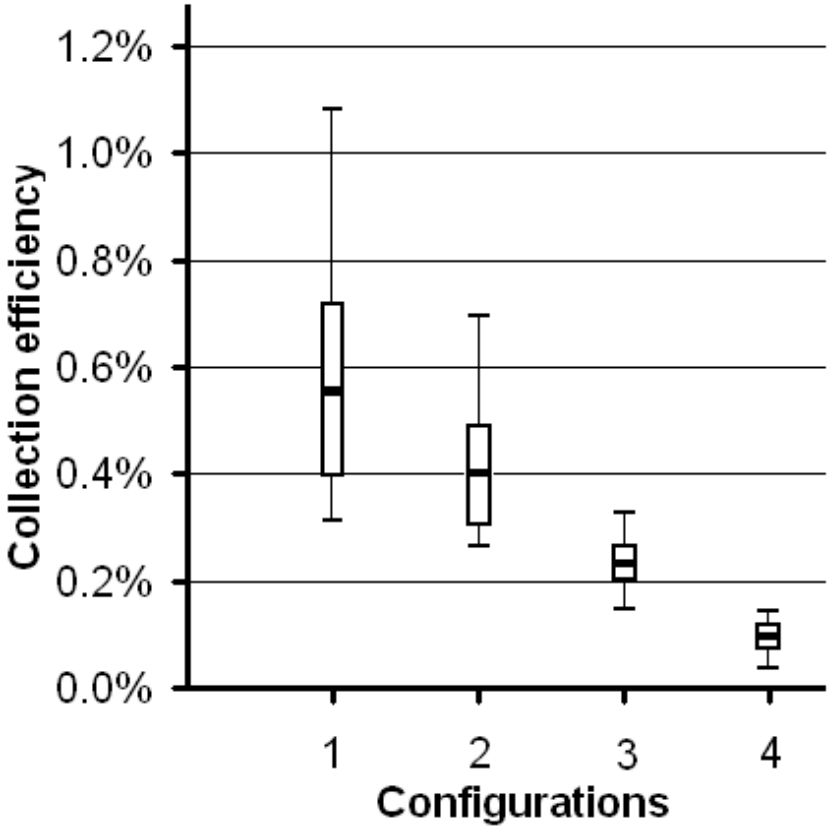

Figure 6.5: Percentage of total number of Brownian particles deposited for each configuration

The removal efficiency due to deposition, which is the number of retained particle over the number of injected particles, for each configuration is summarized in Table 6.4.

	Configurations			
	1: R1c5e3V001	2: R1c2e3V001	3: R1c1e4V002	4: R05c5e4V001
Removal efficiency (%)	1.42%	1.00%	0.57%	0.23%

Table 6.4: Mean removal efficiency for each configuration

6. 4. 1 Flocculation behaviour

A representative example of flocculation behaviour of the particle suspension flowing through the tube is displayed in Figure 6.6. Both fluid and particles flow from the top of the figure to the bottom (though note that gravity was not included in the simulation and the orientation of the figure has no significance). In the region immediately downstream of the inlet, at the top of the figure, particles are evenly distributed due to them being injected following a uniform average distribution over the control window that corresponds to the particle inlet rate previously described.

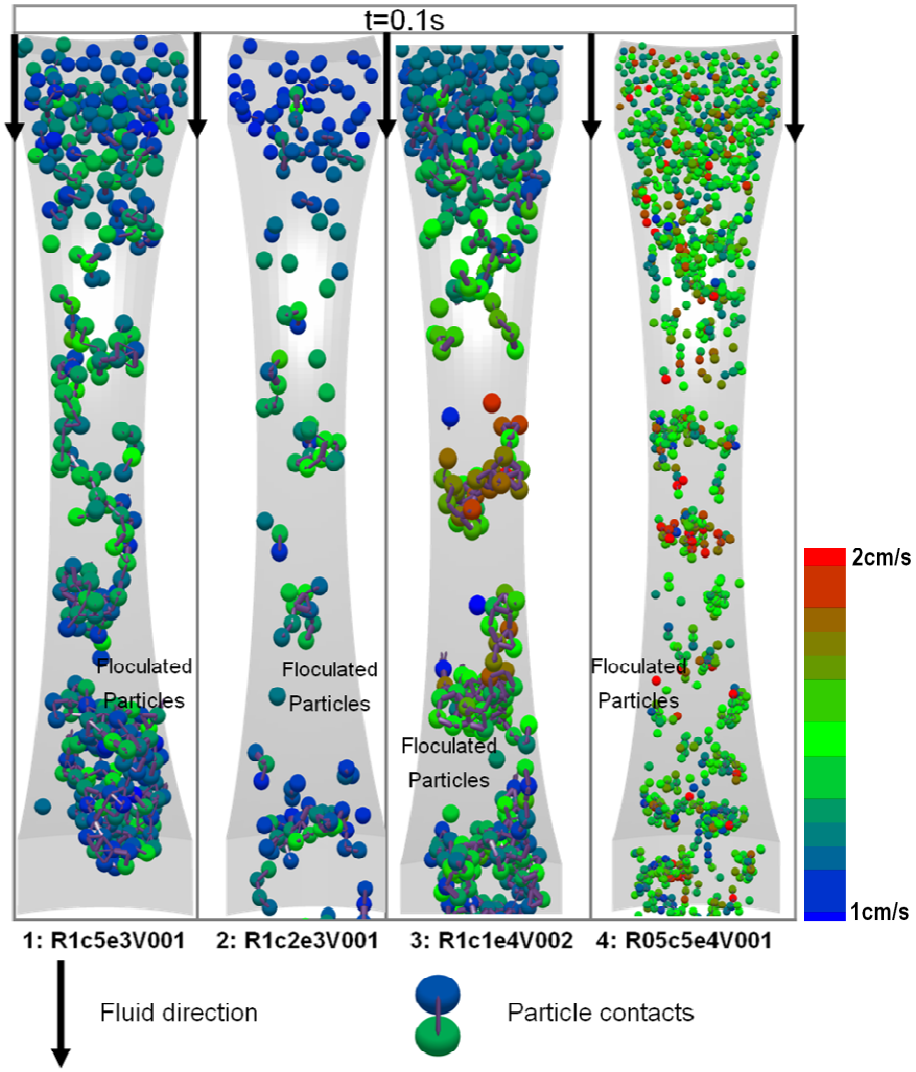

Figure 6.6: Particle agglomeration during particle injection

The particle inlet is in a small region near the wall, particles flowing at the centre being omitted, as following the limiting trajectory principle [12], they do not contribute to the deposition. Under the combined influence of the tube constriction, Brownian forces, particle volume and velocity gradient, the particles form clusters, or flocs, as they flow along the

tube. Clusters grow while flowing through the constriction, and doing so, they segregate themselves from each other, meaning that distinct flowing aggregates are formed (see Figure 6.6), that are delimited by large, particle-free regions in between. These observations are consistent with the related observations made by Marshall [113] when considering aerosol (rather than hydrosol) capture by walls in a particulate channel.

Although the DEM package did not allow easy access to the particle cluster statistics and properties, visual inspection, Figure 6.6, interestingly shows that the flow rate does not seem to influence the size of flowing clusters, as seen on the videos extracted from the performed simulations [114, 115]. Therefore, at given particle volume concentration, the determining factors for cluster size must be the constriction geometry, the particle size and other physical or chemical properties of particles. Visual examination of the results indicates that growth rate of the flocs increases with increasing particle concentration (as defined in Eq. 2.5) as seen on the videos extracted from the performed simulations [114, 116]. This is logical, since particles are given more chance to collide through volume exclusion when a larger number of particles are forced into close proximity. It can be seen that due to the increased growth rate, of the clusters, wall deposition happens much earlier after the particle injection.

6. 4. 2 Deposition morphologies

Example deposition morphologies resulting from each configuration are displayed in Figure 6.7, which shows the particles remaining on the tube walls after all the others have left the computational domain. Along with Table 6.4 and Figure 6.5, it can be seen that on average collection efficiency decreases when concentration or particle size decreases, and when flow rate increases. Most deposition occurs following the pipe constriction, where the flow is decelerating, a result that appears to make sense physically.

The increasing growth of flocs in higher particle concentrations and higher flow velocities does not necessarily mean that particles deposit proportionally to the concentration, as floc formation can have an adverse effect on deposition through impaction and scouring. This increases re-suspension via the scouring mechanism described later.

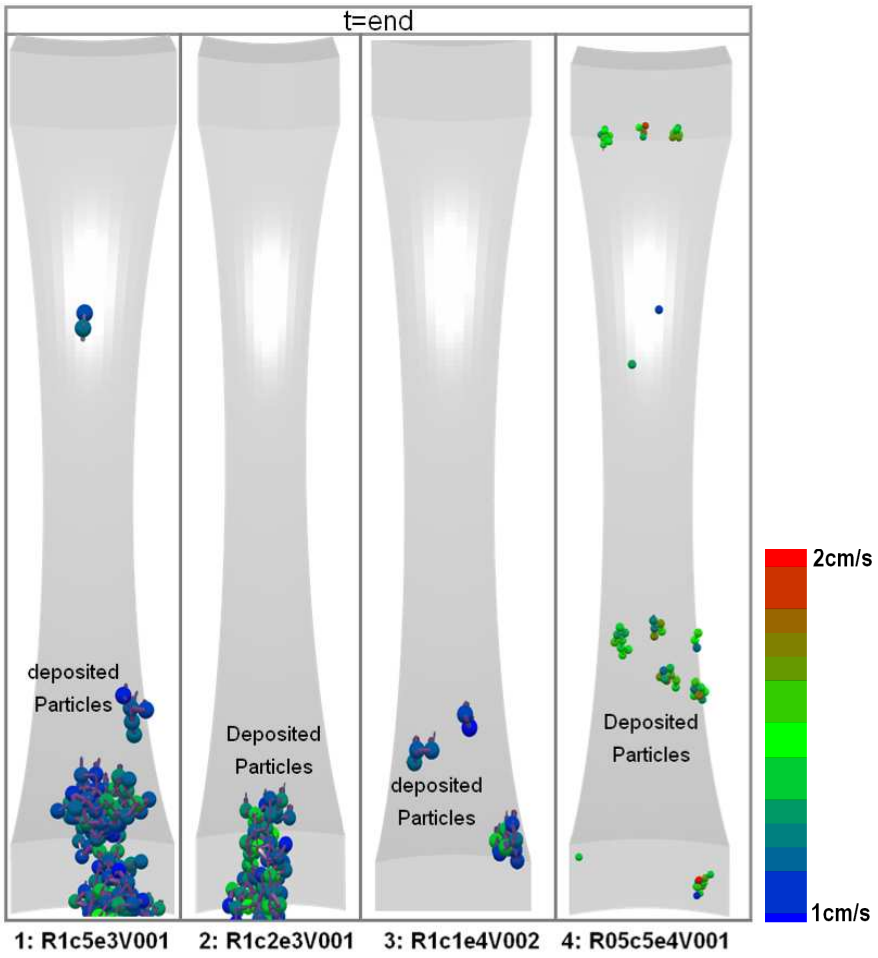

Figure 6.7: Deposited particles after free-flowing particles have escaped

It can be seen that deposition morphologies are quite different than those reported by Chang et al [16], who observed lump particle deposition occurring before the constriction; however the simulation techniques used are different. The contact model and collision detection provided by the DEM framework appear to allow more realistic deposition patterns.

6. 4. 3 Effect of particle size on deposition: notion of total particle volume

As a trend, for the two particle sizes and the concentration range considered in this work, results show that the smaller particle size gave a smaller chance of deposition. For the larger particle size simulated, higher concentration induces higher deposition. The determining factor in particle deposition is not merely the size, but the ratio of total volume of particles flowing inside the tube with respect to the volume of the fluid domain. However,

the number deposited does not increase linearly with the total volume of particles; this is due to impact and scouring mechanisms as later described.

6. 4. 4 Effect of Brownian motion

For configuration 1:R1c5e3V001, a further series of 4 simulations was performed with Brownian forces both enabled and disabled. The mean removal efficiency was found to be 1.42% with Brownian forces included against 3.09% without it. Corresponding collection efficiency (see Eq. 3.2) results are displayed on Figure 6.8. As previously observed by Chang et al [16], Brownian particles have a lower collection efficiency than non-Brownian particles. This phenomenon is explained by the random forces having an adverse effect on deposition, the Brownian forces being applied uniformly in all directions i.e. mostly in directions non-favourable to aggregation.

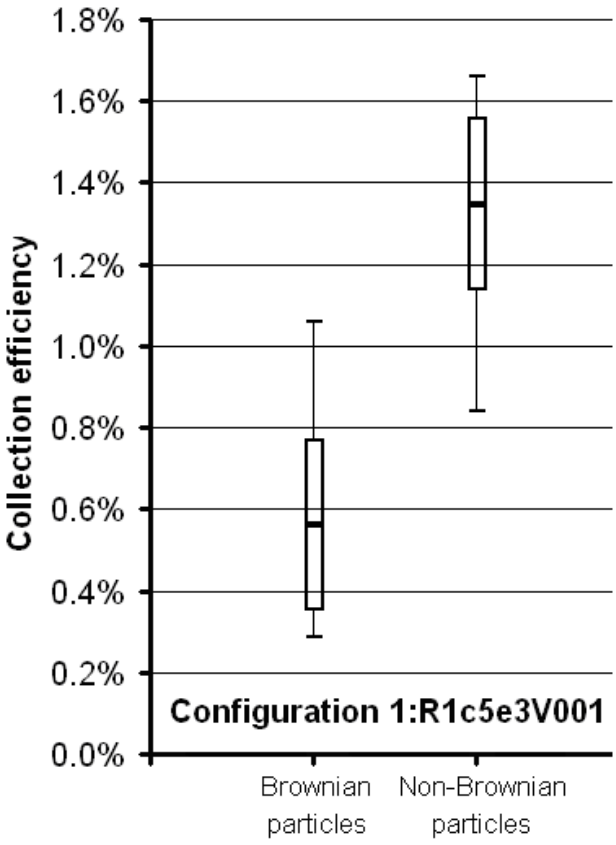

Figure 6.8: Comparison between Deposition of Brownian and Non-Brownian particle

Let's recall that Brownian force components can be written as $F_B = U\sqrt{\frac{12\pi a\mu.kT}{\Delta t}}$ where U is a Gaussian random number with zero mean and unit variance so of maximum value U_{max}~0.035 (Figure 3.5). With the free-stream drag force expressed as $F_D = 6\pi a\mu v$, T=300K, and the time step chosen as 10^{-8}s, the compared magnitude of Brownian force is expressed as:

$$F_B \sim 3{,}5.10^{6}\sqrt{F_D.2kT} \sim 3{,}2.10^{-4}\sqrt{F_D}$$

Given a free-stream drag force of about $F_D = 6\pi a\mu v = 6.3{,}14.10^{-12} N = 3{,}5.10^{-6}\sqrt{F_D}$, it means that Brownian forces are at most $\sqrt{3}.92$ times bigger than drag forces but applied at each step in a random direction, making them balanced each other over several time step, whereas, drag force is constantly applied in the same direction therefore imposing particles' motions over several time-steps.

6. 4. 5 Effect of flow rate on deposition

The number of particles deposited where U_{in} = 0.1 cm/s is always greater than where U_{in} = 0.2 cm/s, hydraulic forces being much larger in the later case, so surface forces become less significant and re-suspension is easier. This is apparent in the comparison between configurations 1:R1c5e3V001 and 3:R1c1e4V002, where in order to keep the same volume concentration of the particle phase, the particle creation rate was increased in the same proportion as the inlet velocity, following Eq. 2.5.

6. 4. 6 Investigation of the mechanism of deposition

In this section we use the results of the DEM simulation to identify the precise mechanism of particle deposition in the collector tube. Central to this is an understanding of how particles move in a direction lateral to the axis of the collector tube, so coming into proximity with the walls. Unless they do this, they cannot deposit.

It should be noted that since the simulated fluid and particle material are of the same density, therefore gravitational effects do not play any role in the particle deposition process. The simulation is laminar, and the inter-particle LvdW forces have insignificant effect unless particles are already in close proximity. Thus, in the absence of other

mechanism, the particles will continue to follow the flow streamlines even as those streamlines curve through the tube geometry.

The DEM results allow mechanical particle interactions to be explicitly considered. DEM-simulated particles, as in reality, have a finite volume and cannot physically overlap or occupy the same volume as another object, which is explained in section 2. 1. 2. Instead, the particles collide and then push each other, which is a major cause of lateral displacement that induces aggregation and wall deposition. This concept can be referred to as *particle size exclusion*.

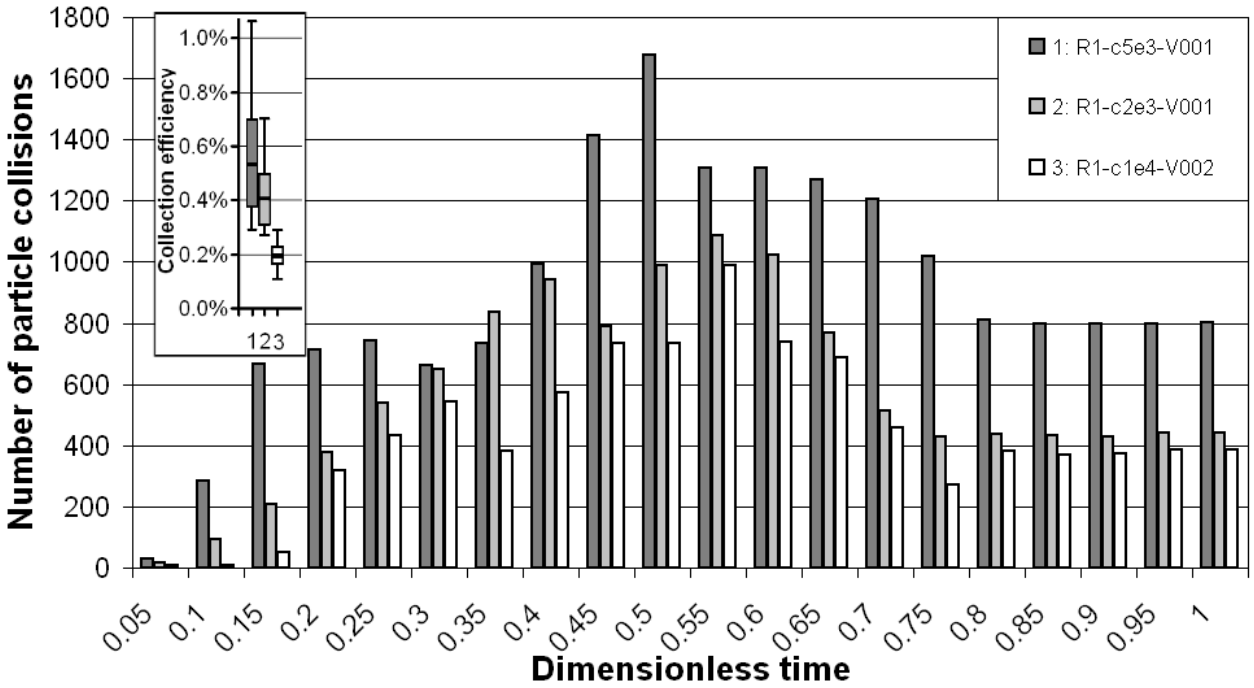

Figure 6.9: Particle to particle collisions correlation with collection efficiency

Figure 6.9 illustrates the size exclusion concept by plotting the average number of particle collisions over the simulation time, for different configurations, related to the collection efficiency of each configuration. It can be seen that the number of particle collisions correlates strongly to the collection efficiency of the configuration. This is explained by the consideration that in the simulations, particle collisions are the only significant mechanism that can induce lateral displacement. Whilst in the DEM implementation it was not possible to estimate the lateral displacement of particles directly, a time consuming property plugin should have been developed for this purpose, it can be inferred, from the above discussion, that lateral displacement is proportional to particle collisions. And will therefore be used in this work as an indicator for particle collision.

Analysing Figure 6.9 along with Figure 6.5, it can be seen that the higher the number of particle collisions, the higher the number of deposited particles. It is then interesting to see what the correlation between collection efficiency and the number of collisions is. This is what Figure 6.10 displays. With only three data points, which correspond to the considered configurations, trends can be suggested. It can be seen that the correlation has been interpolated by linear and parabolic function, as the number of data point is insufficient to have an optimal curve fitting. However, no matter what correlation is used, its intersection with the X-axis gives the threshold of minimum average of collision that has to occur in the tube in order to observe any deposition; it lies between 70 and 310.

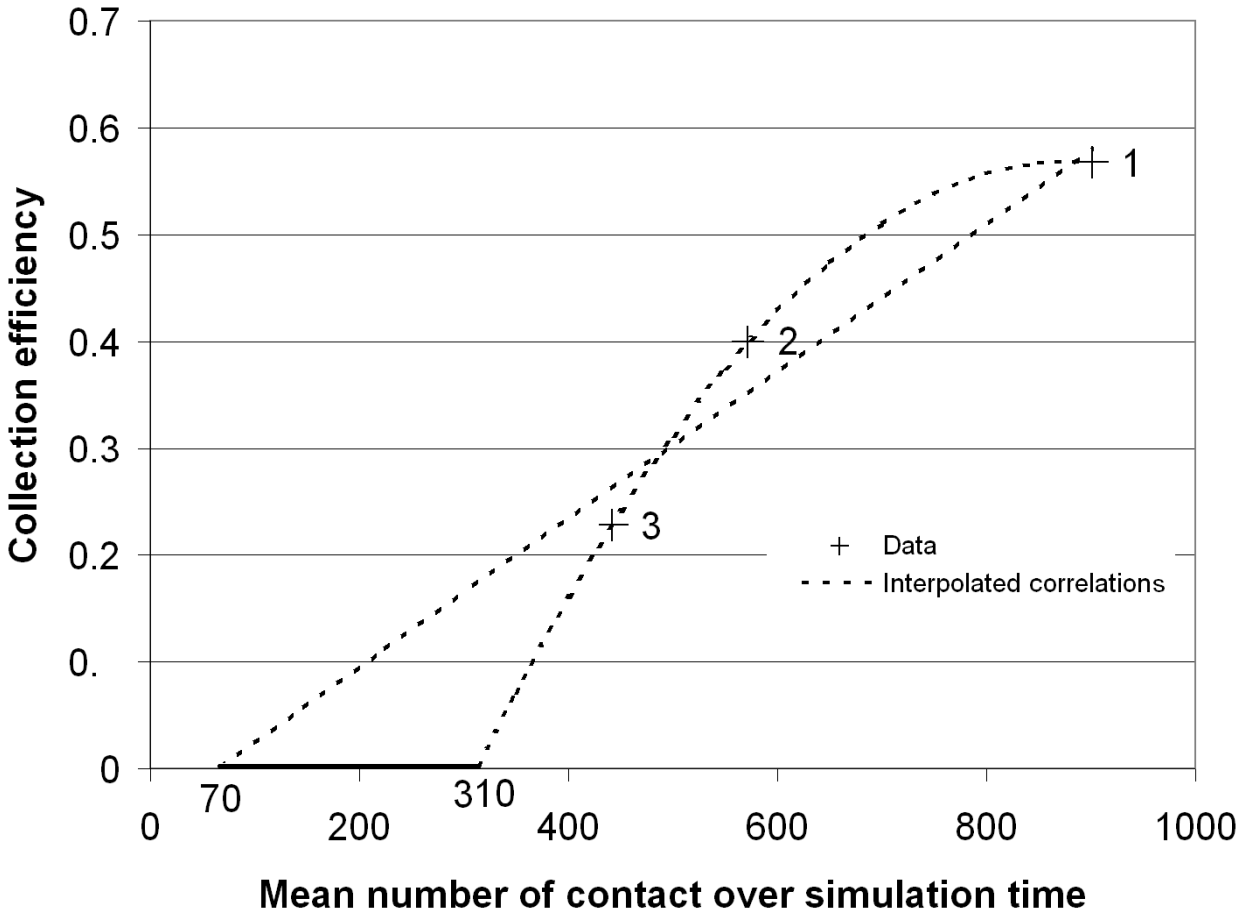

Figure 6.10: Correlation between collection efficiency and particle collision number

Unlike conceptual 'point' particles, with effectively no volume, our results show that particle collision arising from particle size exclusion that derives from considering the volume of particles plays a major role in deposition mechanism, as it is responsible for bringing particles in proximity to the wall, through lateral displacement.

6. 4. 7 Investigation of the mechanism of re-suspension

The DEM results allow for the detailed investigation of the re-suspension of previously deposited particles. Champlin [117] observed that organic matter deposited on a membrane was reduced in the presence of particulate matter and postulated that particles acted as abrasive scouring.

Altmann [118] showed that deposited particles are either re-suspended as flocs or not at all, meaning that single deposited particles will not re-suspend due to hydrodynamic forces alone. However, because of the near-wall shear layer in the fluid, the side of larger deposited clusters closer to the centre of the tube is subjected to larger fluid forces than the area nearer the wall.

Aggregate or floc formation in the bulk of the fluid facilitates particle re-suspension by floc collision and scouring; in fact, these phenomena are identifiable in the simulations as the main cause of particle detachment. Figure 6.11 illustrates each step of the mechanism, where a deposited, immobile, aggregate of particles (1) grows bigger by accumulating/catching free flowing particles and flocs, (2). Then, either the impact (3) of a free flowing cluster will cause the initial deposited aggregate to re-suspend (4) or the newly agglomerated particle will cause the deposited aggregate to experience higher hydraulic forces without contributing to the cluster's attachment to the wall, causing it to either roll or re-suspend directly.

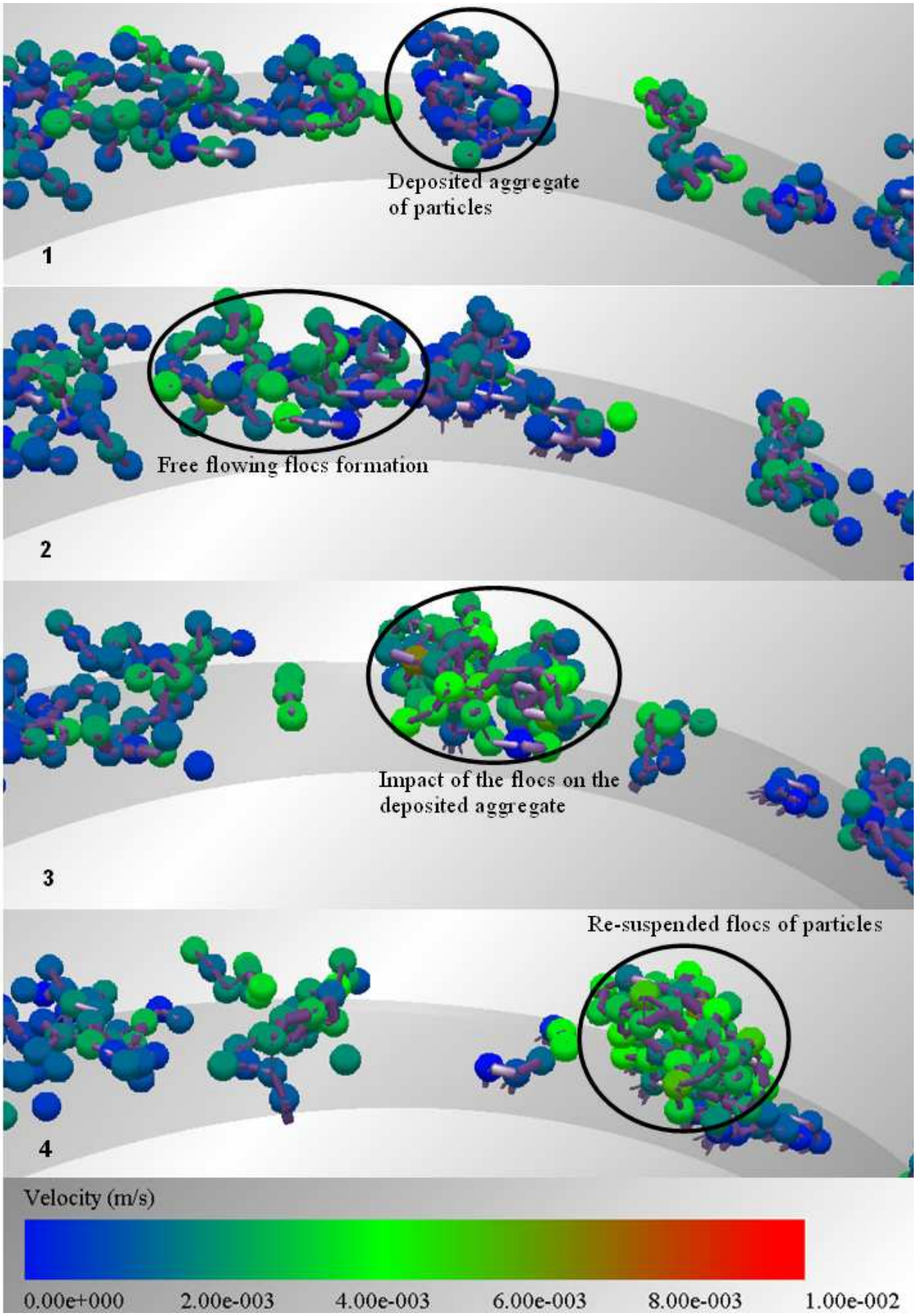

Figure 6.11: Frame by frame example of scouring mechanism on deposited particles

Figure 6.12 plots the evolution of the number of deposited particles as a function of the number of injected particles (i.e. as a function of time, since injected particle number is the creation rate multiplied by time). For each configuration, different coloured lines are displayed that corresponds to different runs with the same set of parameters, these lines illustrate how the variability of results for a same configuration compels to perform multiple simulations for each configurations.

By looking at the graphs, one can examine the deposition and re-suspension behaviour. Each configuration exhibits peaks and troughs that are linked to the scouring mechanism. If a cluster is loosely attached to the wall, i.e. via a small number of its particles, it can roll along the wall, attaching itself to the wall via different particles that successively attach and detach themselves from the wall as the cluster rolls. The rolling mechanism is generally associated on Figure 6.12 with flattened peaks (indicated by the arrows ↘). The height of the peaks is broadly proportional to the size of the flocs.

In some cases, the number of particles that attach the cluster to the wall is not enough to balance the fluid forces acting on the cluster, and it will re-suspend (Figure 6.11), meaning it is pulled back into the bulk of the suspension. This corresponds with downward slopes on the plots in Figure 6.12. The graphs exhibit a wide range of peaks sizes, which confirms the importance of cluster scouring in the variability of the results that relates to the above analysis of Figure 6.11 that matches the numbering (1, 2, 3, 4) on displayed as an example on the purple line of Configuration 1 . This conclusion would not have been possible without the explicit particle modelling available using DEM.

Interestingly, as previously explained, configurations with high particle depositions are also the one with the biggest standard deviation, which can be explained by cluster scouring, where as more particles deposit, more particle clusters then re-suspend during scouring.

Due to simulation time constrains and the necessity of repeating simulations, only a fixed number of particle were simulated and particle flow was not continuous over a long period of time. Therefore, it cannot be assumed that simulations reached the steady state. However, particle flow was continuous over the time interval investigated, hence the mechanisms described above can be assumed to be representative of mechanisms that would occur under steady state conditions.

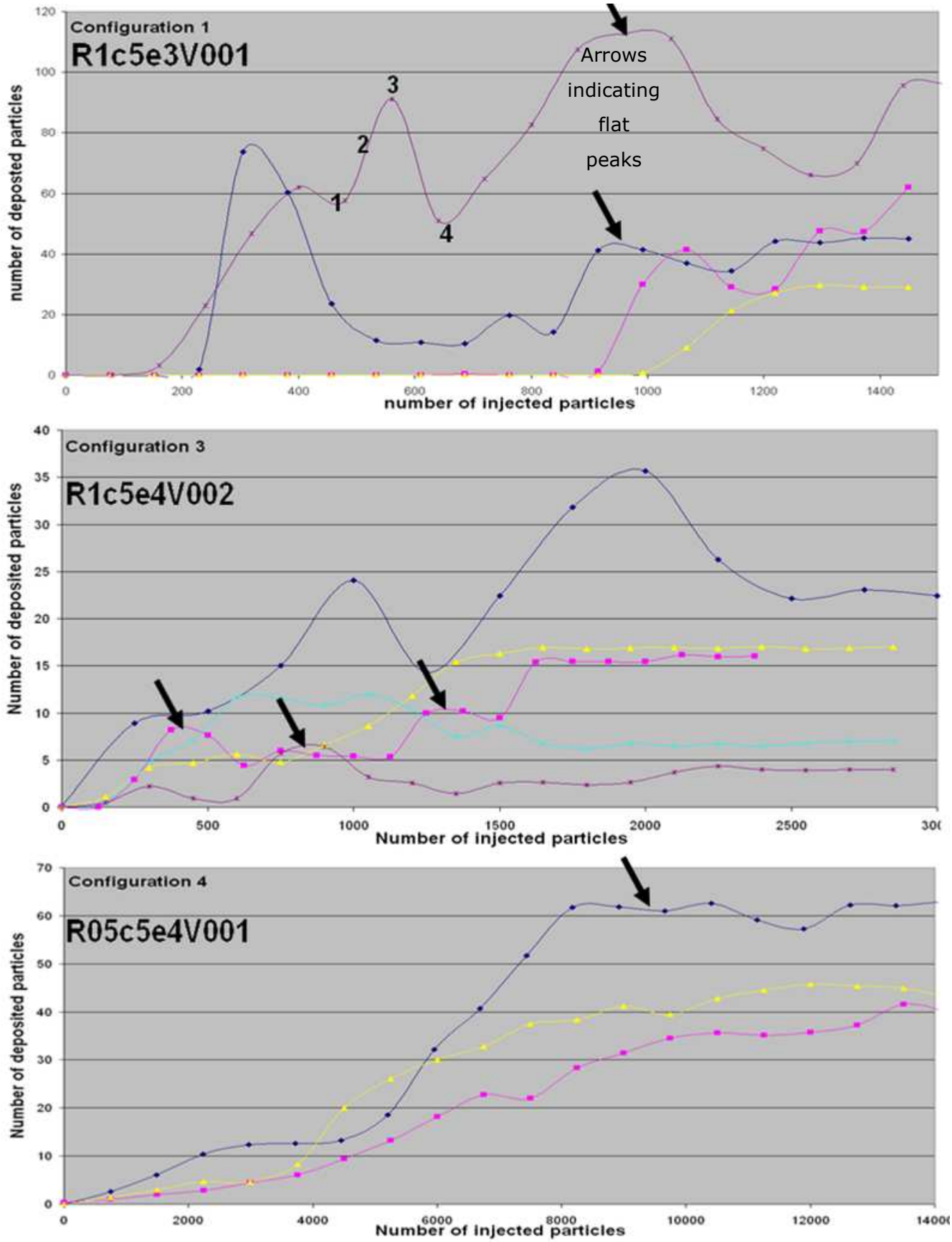

Figure 6.12: Evolution of particle deposition

6. 4. 8 Comparison between one-way and two-way coupling

The configuration 2:R1c2e3V001 has been run 5 times with the one-way coupling and gave an average removal efficiency of 1% with the highest being 1.64% and the lowest 0.63%. The configuration 2:R1c2e3V001 was run only once with the two-way coupling, because computational time was four times higher than for the one way coupling, taking up to 21 days to run on a 3GHz Core2 Quad CPU desktop computer with 3GB RAM. The computed removal efficiency is 1.22%, which is not significantly different from the result obtained more quickly with the one way coupling. The configuration 3:R1c1e4V002 has been run 4 times with the one-way coupling and gave an average removal efficiency of 0.57% with the highest 0.96% and the lowest 0.16%. The configuration 3:R1c1e4V002 was run only once with the two-way coupling because computational time was five times higher than for the one way coupling, taking up to 29 days to run. The computed removal efficiency is 0.45%, which is, again, similar to the results obtained the one way coupling.

	Coupling type	Removal efficiency (%)	Average time (days)
Computation comparison for 2: R1c2e3V001	one-way	1.00%	5
	two-way	1.22%	21
Computation comparison for 3: R1c1e4V002	one-way	0.57%	5
	two-way	0.45%	29

Table 6.5: effect of coupling method on computation

The two-way coupling takes much more time to run, firstly because of the added CFD computation that must be updated, in this work, at least every 50 DEM iterations for the fluid conditions to be coupled faithfully with the local particle loading. Indeed, the CFD time-step in two-way coupling has to be chosen big enough not to hinder computational speed un-necessarily, but small enough as to provide a sensible continuous description of the multiphase flow. Secondly, and more importantly, because the extensive exchange of information between the two platforms takes longer than the CFD computation time and

DEM computation time combined. Whatever the simulated particle size, the two way coupling requires that the CFD cells be at least two times bigger that the particle diameter, so the CFD mesh is coarser for the two-way coupling and any flow disturbance induced by cluster formation could not be captured. Therefore the simulated particle trajectories were not affected, which led to similar results to the one-way coupling, that by definition did not take into account the flow disturbance and modified drag induced by cluster formation.

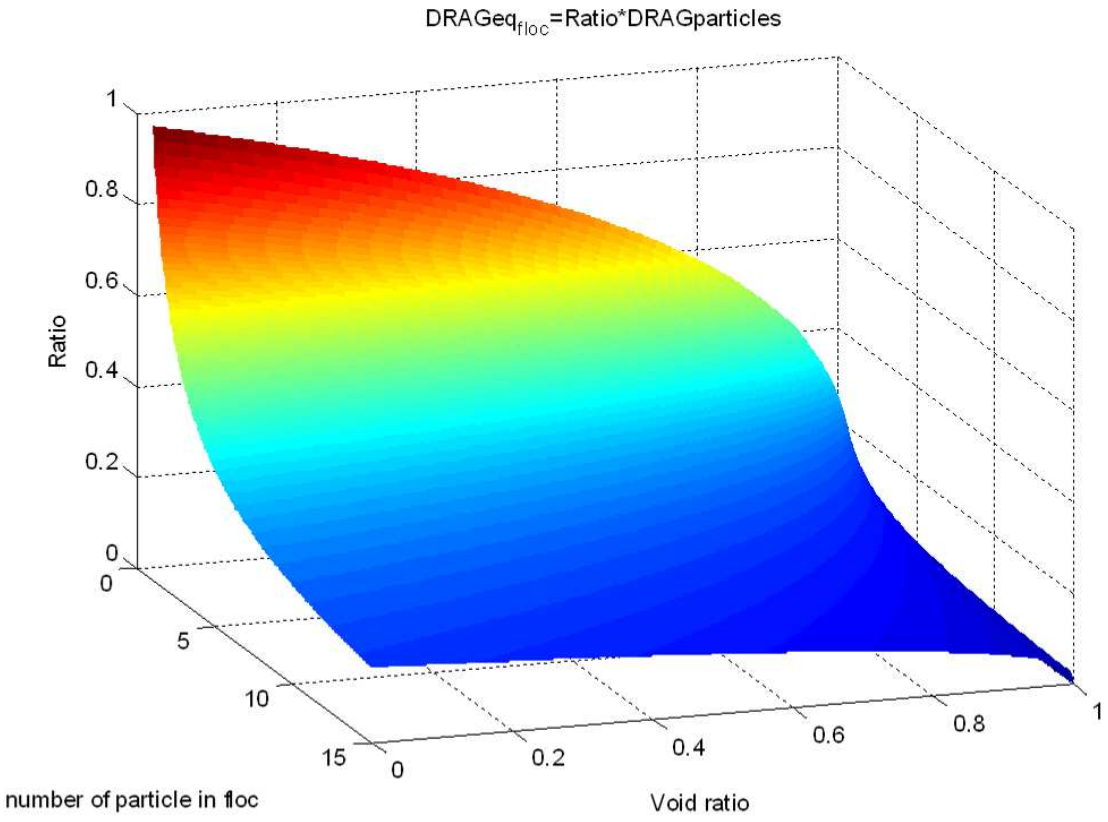

Figure 6.13: Drag force ratio on a particle of cluster equivalent volume

In the present work, clusters overlapped a maximum of two or three cell centres, and occupied a volume fraction inferior to 30% in these cells. If the DEM-CFD method allowed having smaller mesh sizes, it would have been expected, because of shading effects i.e. lost of relative fluid velocity within the cluster, that the drag on a cluster of particles would have been lower than the sum of the drag on each particle that are within it, as defined in Figure 6.13. Therefore, wall deposition would have been enhanced. It follows that, for the current configurations there is evidently no advantage in running full two-way coupled solutions.

A further issue is the accurate modelling of hydrodynamic drag on flocs on the one way coupling DEM simulations. The drag was calculated on each particle separately, and the drag on a floc was therefore determined from the aggregate of these. However, particles

located within a cluster, are shielded from the fluid flow, and they contribute much less to the drag on the cluster. It means that the net drag on a floc is much less than the sum of that on all the particles individually. This effect can be calculated, comparing the drag on particles to clusters with a conceptual radius and density dependent on void ratio, as shown in Figure 6.13. Significant changes to the DEM implementation of flocculation would be required to reproduce this effect. For example, an algorithmic structure keeping track of the entire network of connected particles might prove usefull. In any case, an efficient way of computing the local volume fraction of particle would be required in one-way coupling simulations to be able to implement Ergun type drag model that better estimates the effects of neighbouring particle on drag.

6. 5 Conclusion

A series of particle scale simulations have been performed using DEM in order to model numerically flocculation and deposition of colloids in a constricted tube. Colloidal surface forces were implemented and interfacial Van der Waals interaction, retardation effects were considered along with Brownian forces. A model was implemented through the commercial DEM software EDEM 2.3®, allowing the implementation of custom forces. A CFD computed velocity field was used to represent fluid velocity.

The DEM results have allowed the interpretation of particle aggregation, deposition and re-suspension phenomena that have not been explained in previous work where particles were not explicitly represented in the simulations.

It was found that particle deposition was strongly correlated to inter-particle collisions, with increasing particle concentration and particle size – ie the total volume concentration of particle phase material in the flow – contributing significantly.

It was further found that aggregate formation and scouring due to hydrodynamic forces and the impact of other flocs still in suspension contributed significantly to particle re-suspension.

One-way computational coupling between the fluid flow (CFD) and the particle (DEM) models was found to give similar results to the two-way coupling, but was much more computationally efficient.

Local volume fraction of particle would be required in one-way coupling simulations to be able to better estimate the effects of neighbouring particle on drag.

Implementing colloidal forces with DEM-CFD technique has offered the ability to look easily into details of each of the particle deposition factors and their correlation between each other. It enables higher visibility and reproducibility, and broadens the number of possible users of such modelling.

CHAPTER 7: DEM simulations of initial deposition of colloidal particles around non-woven membrane spacers

7. 1 Introduction

Spiral-wound modules (SWM) are used in many types of filtration processes like desalination, water purification and food processing since their spiral type configuration offers high specific membrane area. However, they are restricted in their performance by concentration polarisation and fouling, like any membrane process. This fouling results in increased capital and operating costs, for example in the installation of redundant modules, the replacement of used modules and in filtration efficiency drop. The spiral configuration also requires membrane spacers to keep each layer of the spiral separated and provide sufficient room for the water inflow.

Spacers play an important role in membrane systems [119]. They support and separate membrane sheets, or layers, in SWMs, which is why they are also found in electro-dialysis stacks. They can have beneficial effects on mass transfer, homogenizing and mixing behaviour, hence reducing fouling [120]. Spacers are usually composed of net of intrer-locking filaments as shown in Figure 7.1 or more rarely of extrusions of membrane surface [121]. Feed spacers can be designed for enhancing re-suspension of the rejected species to the bulk of the feed flow and thus lowering concentration polarization in spiral wound membrane modules. However, one adverse effect is that they induce pressure drop along the membrane module; this can lead to higher power consumption as illustrated by Da Costa et al [122], who showed that hydrodynamic angles (α and $\beta=2\alpha$), Figure 7.1, are critical parameters in designing spacer-filled membrane channels. Pressure drop is dominated by the drag force on spacer strands and Darcy-Weisbach friction like kinetic losses due to the flow direction changes [123].

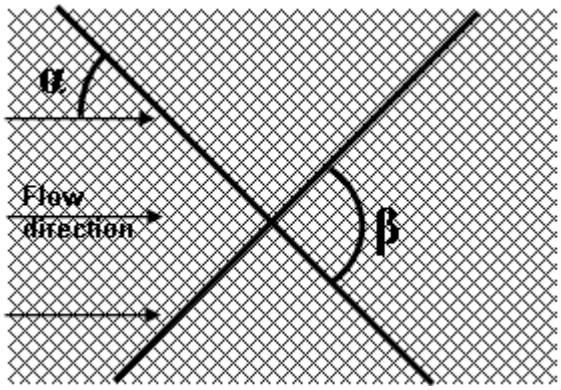

Figure 7.1: Sketch of net-type spacer's structure

In order to optimize the trade-off between enhanced mass transfer and increased cross-flow power consumption, CFD modelling [124, 125], [126], [127], [128, 129], [130], [131], [132, 133] has been used extensively. However, computational techniques have rarely been used to investigate the other issue of SWM, that is bio-fouling, arising from their extensive use in municipal water treatment plants and in industrial food processing. Spacer bio-fouling has been observed in industrial SWM autopsies, which are a laborious method and can be studied though a direct observation through membrane (DOTM) requiring expensive optical instrumentation. For this reason, numerical modelling can provide precious insight. Spacers provoked great interest and Vrouwenvelder et al [134] went as far as saying that "bio-fouling is a spacer and feed channel problem".

Bio-fouling occurs via the formation of a bio-film that is initiated by the adhesion of primary colonizing organisms like microbes and bacteria, whose adhesion is controlled at first by long-range forces such as attractive Van-Der-Waals forces and repulsive electrostatic forces [135]. They form micro-colonies composed initially by organisms of same species. They later combine and form colonies and other types of bio-film structures composed of different microbial strains including algae, fungi and protozoa. These find energy and organic material (nutrient) for growth from dissolved feed-water organic material [136]

The critical flux of a membrane system is defined as the flux at which the relation between the trans-membrane pressure (TMP) and flux is no longer linear, due to matter deposition. Neal et al [137] used the DOTM technique to determine the effect of spacer orientation on this critical flux. They found that spacers significantly increase critical flux for a flow laden with 6.4μm latex beads. The degree of enhancement depended on spacer orientation, which means that spacer orientation has an effect on how particle deposit on the membrane. A similar observation technique was used by Vrouwenvelder et al [134] in order to observe the onset of bio-film formation on the spacer itself and showed that deposition initiates

upstream of the spacer, in front of the filament junctions and to a lesser extent on the filament body after a long time. These results were later extended using the multi-physics package COMSOL and a cellular automata algorithm to numerically model the fluid dynamics and bio-fouling of feed channels [138]. It was shown that bio-fouling is a problem of initial deposition and bio-film growth and not a deposition effect due to filtration pressure. They confirmed that initial deposition occurs upstream of the spacers, but demonstrated that the biomass volume increase, that reduces the filtration efficiency, corresponds to microorganisms multiplication that accumulate mainly downstream of the spacer. Experimental work from Ngene [121] on a structured membrane, which is essentially a membrane with protrusions that play the same hydraulic role as SWM spacers, showed that there is initially a predominance of bio-film formation upstream of the structures, with a downstream formation of filamentous bio-film attached to the back of the structure at a later stage. Bio-film formation on the micro-obstacles was observed to be following a mechanism comparable to that on woven spacers [121].

Calculations made by Bacchin [4] et al suggested that critical flux depends strongly on particle size. For particles over 1μm, the shear-induced diffusion that lifts particles away from the membrane surface becomes significant and competes with the surface charge effects. Following this, a lower amount of foulant is observed with such particles, in comparison to the effects of bio-fouling, where extra-cellular polymeric substance (EPS) adherence and growth also contribute. In addition, for particulate fouling, there is a limited mass of particles that can be deposited on the surface of the structures, after which there is equilibrium between the deposition and detachment of particles from the structure surface. However, the mechanisms of initial particle deposition strongly correlate with observations on primary bio-fouling [139]. It is therefore hypothesised that simulations of particulates as described in this work can predict initial deposition patterns which are applicable both to particulate fouling and to bio-fouling, meaning much can be learned about bio-fouling without the need to model the impact of EPS mediation and growth, which would be computationally expensive.

This work will describe a novel and simple method to address the issue of initial particulate and bio-film deposition. The later stages of microbial growth and colonization will not be considered, as it would require more extensive computational resources. Simulations will consider 2μm diameter size micro-particle (which is about the same size as common microbes such as *E. coli* [3]) around the joints of non-woven net type spacers, as those are the most commonly used in SWM. Simulations will only be considered at low inlet velocity, which correspond to lab scale setup rather than industrial application. This is because the

effects of turbulence-particle interaction encountered at higher velocities remain an unresolved subject of ongoing research.

The ability of DEM-CFD to model particle agglomeration, cluster scouring and particle re-suspension as flocs was demonstrated in CHAPTER 6: therefore the same technique will be use to model the particle interactions with the spacers' surface and between themselves.

7. 2 Definition of spacer geometry

Spacer geometry has been chosen to match the commercial range of spacers NALTEX-51 as this has already been subject to published studies, both experimental [122, 126], and computational [126], and has therefore a well defined geometry, with specifications readily available. Many studies [120, 128, 129, 140] use artificial, generalized dimensions in order to evaluate qualitatively spacers' mitigating effect on filtration. However, the present study seeks to evaluate the modelling method against previous results. Therefore, it has been chosen to model commonly cited configurations. There is a wide range of commercial spacers to choose from, but only a few particle deposition studies that poorly communicate the dimensions of their models. The Naltex series were the best documented ones at the time of this study, although no particle deposition study has been found with their exact geometry. It is however believed that deposition numbers and morphologies follow similar enough trends to be compared. Naltex basic geometry is shown in Figure 7.2.

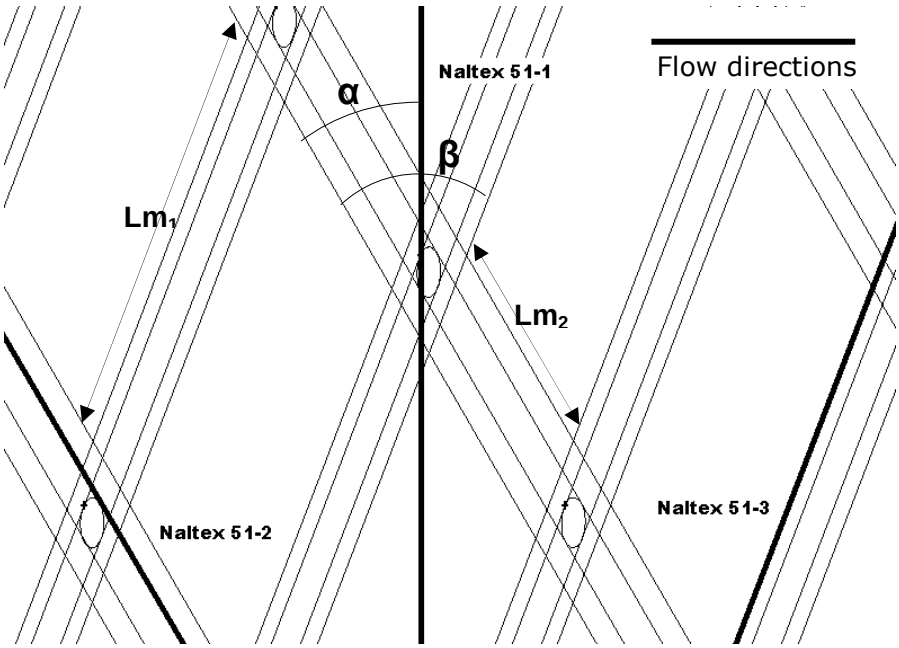

Figure 7.2: Naltex spacer parameters definition

Each product in the range is merely a rotation of the others by various angles, indicated by α and β in the figure. This fits the purpose of our work to model how the feed flow direction influences particle deposition on the spacer filaments.

Spacers parameters	Value
α	30°
β	51°
R_S (small filament radius)	0.25mm
R_B (big filament radius)	0.35mm
Lm_1	5.37mm
Lm_2	2.89mm
Filament overlap	0.03mm

Table 7.1: geometrical parameters of the Naltex-51 spacers

The three-dimensional model was built using GAMBIT 2.1® with dimensions provided in Table 7.1, and the fluid velocity field was computed with FLUENT 12.0 with a 1mm/s inlet velocity in order for the flow to remain laminar [130]. A particle-tracking model, implemented through the DEM software EDEM 2.3®, was used to simulate the particle deposition under the influence of both fluid drag and Van der Waals attraction, as described in the next section.

7. 3 Model implementation

7. 3. 1 CFD method description

Due to the complexity of the spacer-filled channel to be modelled, computational fluid dynamics (CFD) was used to derive the flow velocity field, and an unstructured mesh was used (Figure 6) to compute the fluid velocity field that will be used for the spacers simulations which will all be exclusively one-way coupled.

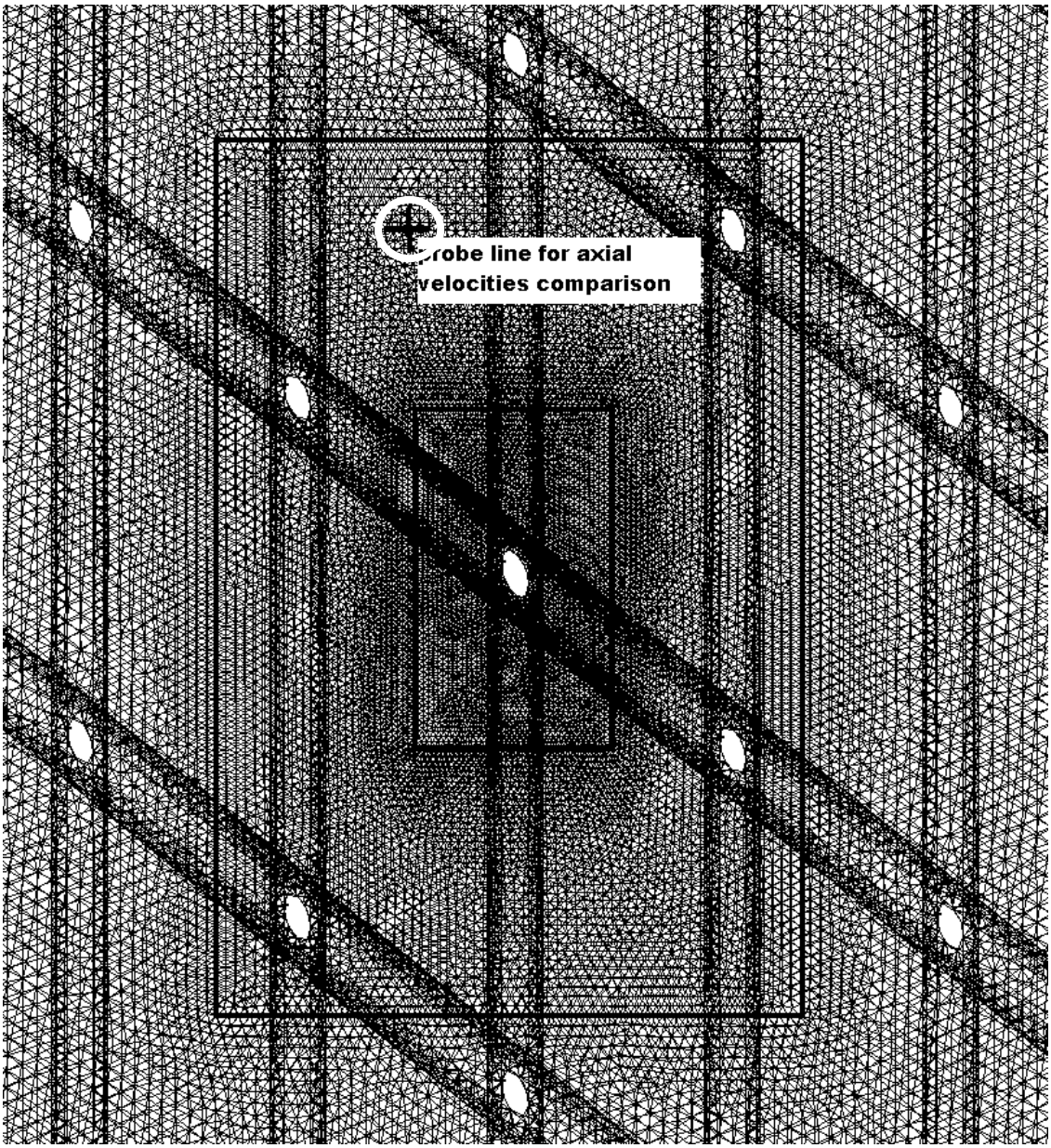

Figure 7.3: Unstructured mesh around spacer filaments joint

The commercial software FLUENT 12.0 was used to solve the steady-state Navier-Stokes equations under laminar flow hydrodynamics. The mesh was created to ensure residual convergence and stability as well as independence of the solution.

Boundary conditions for the model include no-slip boundaries at the spacers' wall surface, a no-slip condition at the membrane surface; permeate flow is considered slow enough to be neglected as [141], and a predefined inlet velocity of 1cm/s was used at the cell entry.

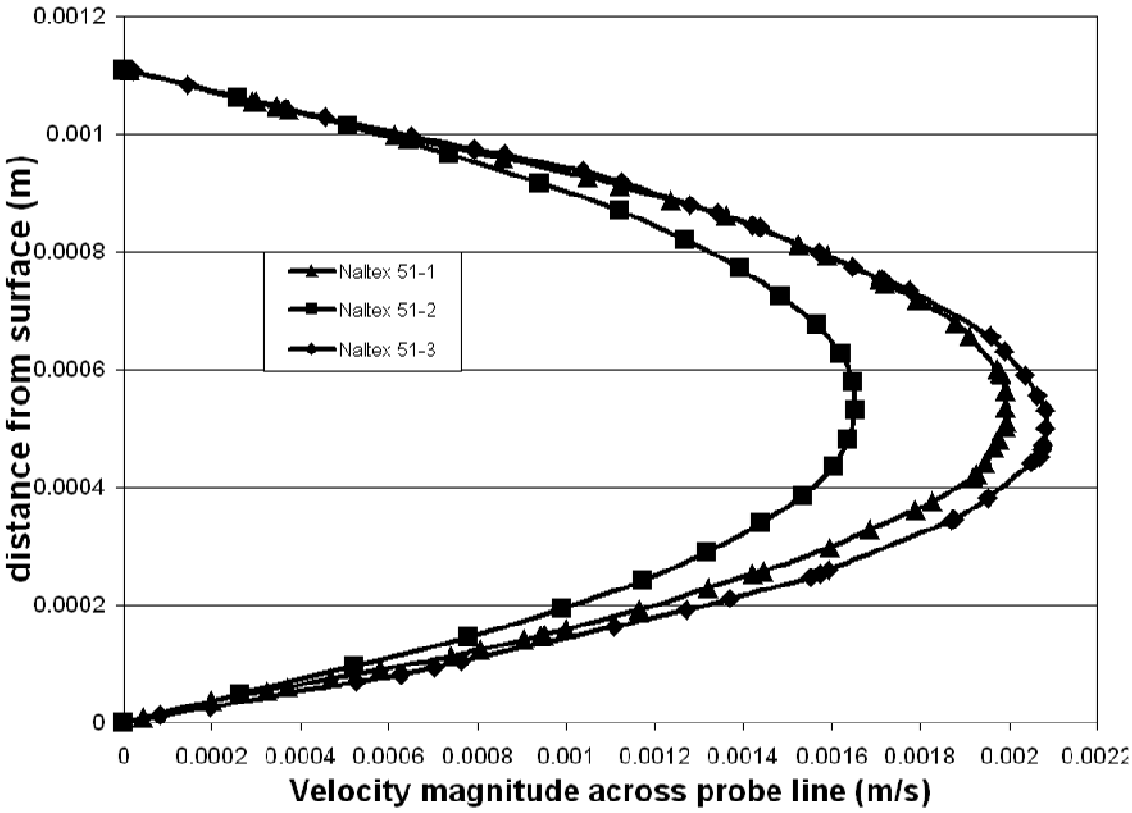

Figure 7.4: Axial fluid velocities comparison

Velocity magnitudes have been extracted from CFD results along a probe-line located at the centre of the spacer cells (Figure 7.3) in a similar manner to Karode and Kumar[126] (Figure 7.4). Velocity profiles appear to be close to parabolic, which is to be expected for a laminar flow between two plates. CFD results are also consistent with Wardeh and Morvan work [130], although their test feed channel geometry is slightly wider.

7. 3. 2 DEM implementation description

Mechanistic principles are implemented via the EDEM™ 2.3 software which allows coupling with CFD data, with the ability, via API programming, to add the required force models which are not standard to the software.

For each spacer configuration, particles were created within an inlet control window (Figure 7.5), which surrounds the spacer filaments. Following the limiting trajectory principle [12], particles injected further way from the wall would not contribute to the deposition process.

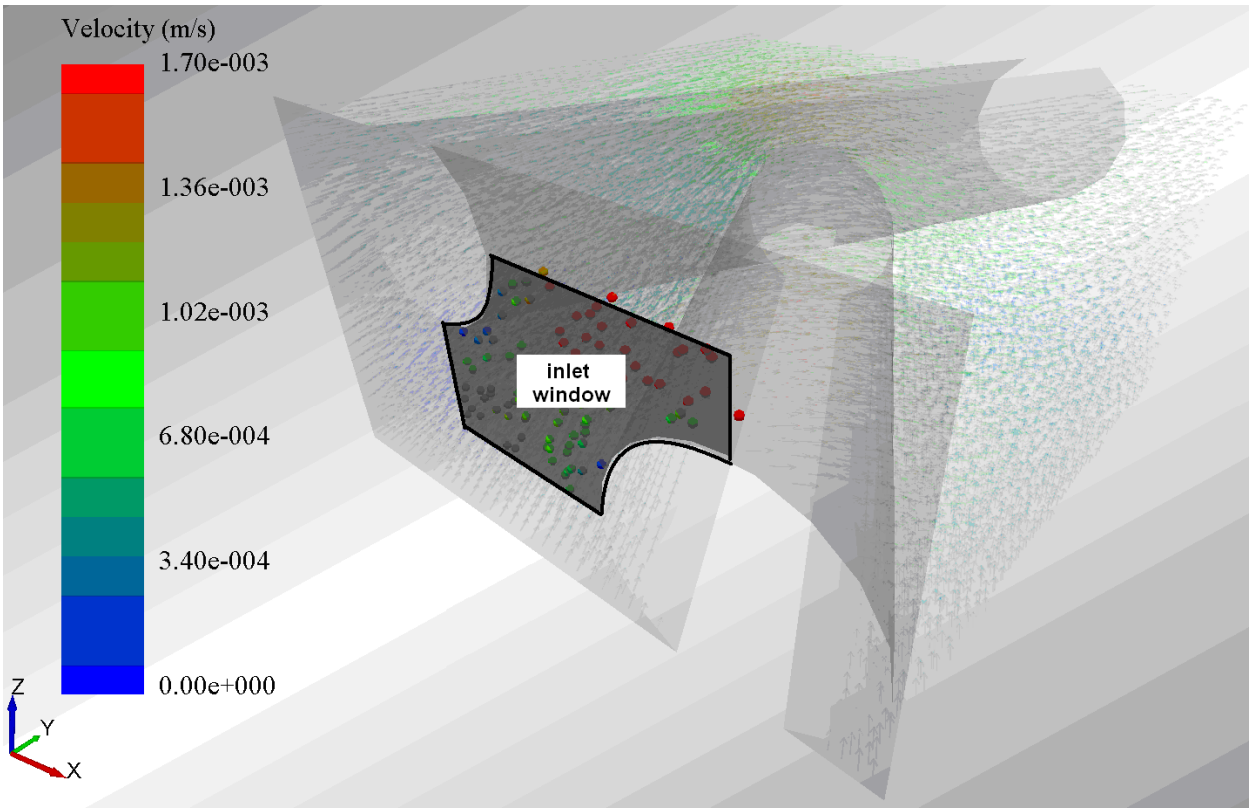

Figure 7.5: Particle inlet window

Particles were randomly created one by one following a uniform distribution over the control window surface. The particle creation rate was set to 10^5particles/s in order to allow a high enough concentration of particles in the computational volume and favour particle-to-particle collisions and cluster formation.

For each single simulation, the computation was left running until the suspended particles escaped entirely, on a 3GHz Core2 Quad CPU desktop computer with 3GB RAM, it took 6.5 days to run each of the three simulations. Once each simulation finished, only deposited particles remained in the computational domain, which provided a way to quantify the amount of deposited particle for each configuration.

7. 4 Results and discussion

The number of particles deposited in each Naltex 51 spacer configuration obtained from the simulations is given in Figure 7.6. Results display the number of particles deposited in function of the axial distance from the spacer join, in the direction of the inlet flow.

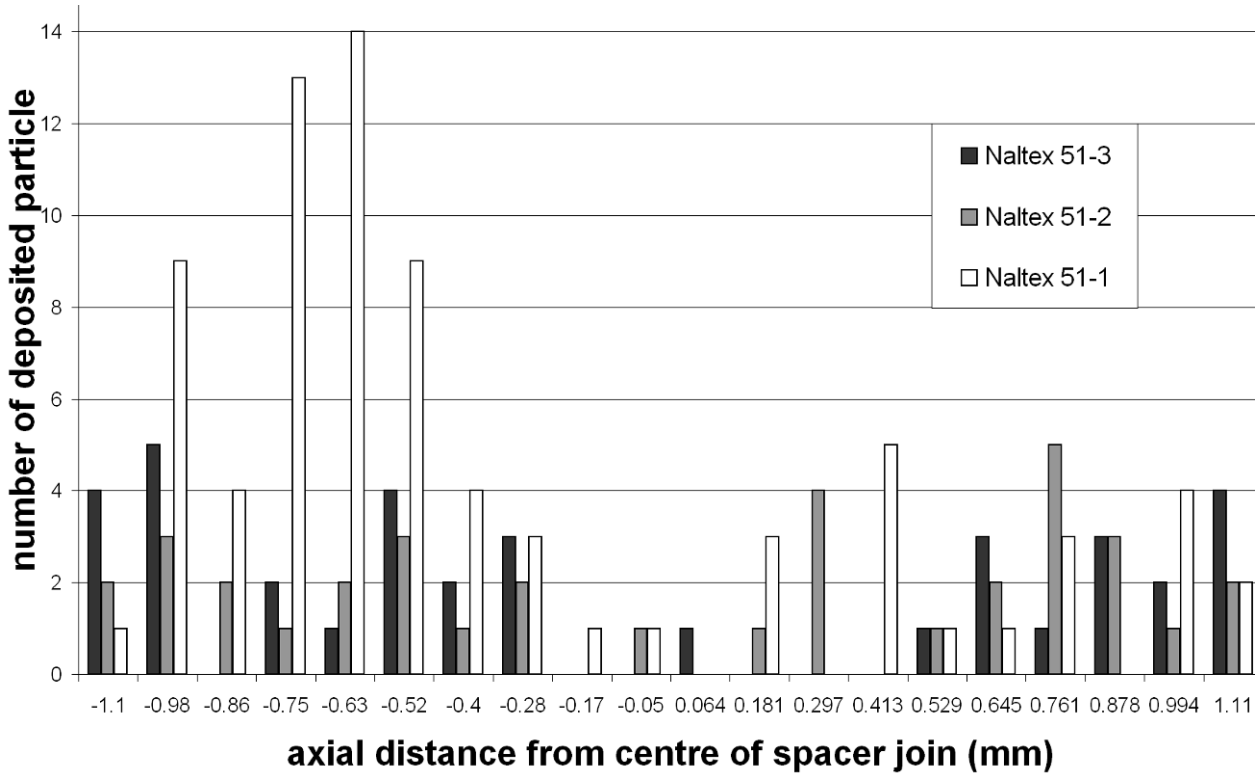

Figure 7.6: Number of deposited particles for each configuration

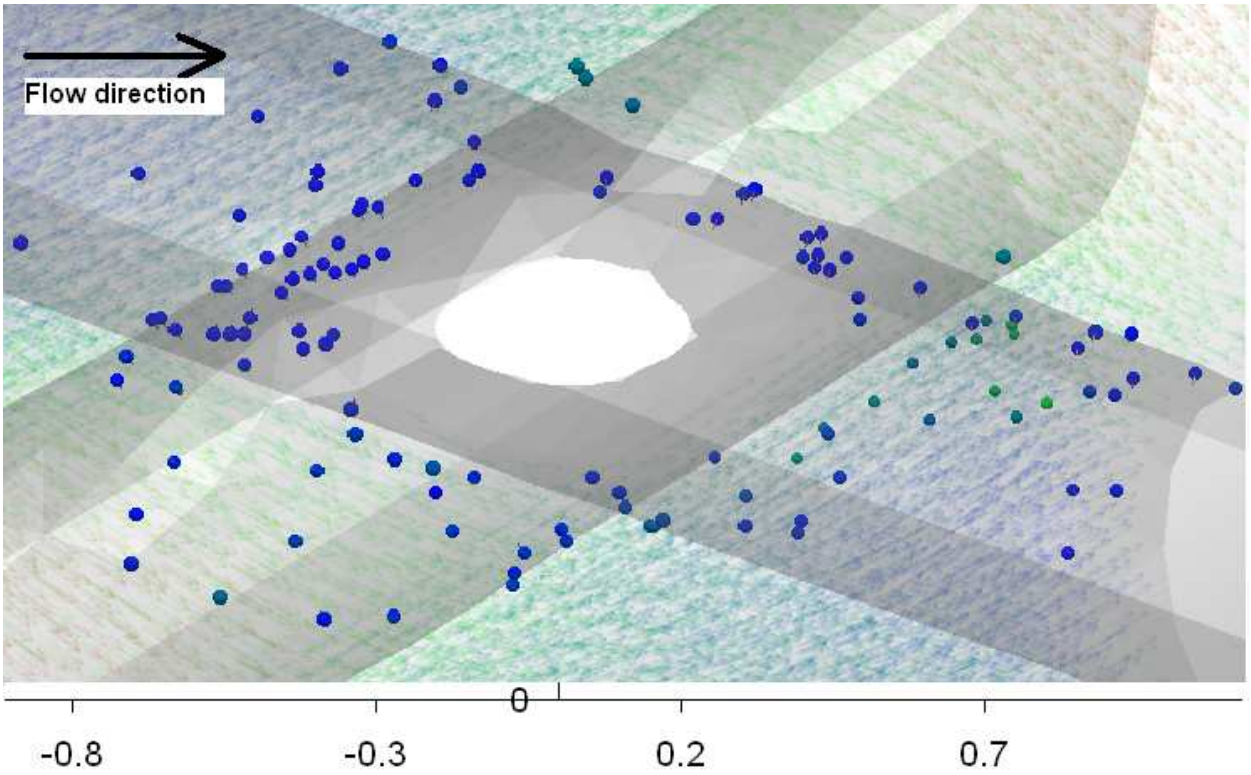

Figure 7.7: Deposition around Naltex 51-1 spacer joint (with distance scale in mm)

For configuration 51-1, Figure 7.6 and Figure 7.7 show there is a preferred deposition location in front of the spacer joint, which does not appear for configuration 51-2 or 51-3 where a constant deposition regardless of the position of the joint is exhibited. After the joint, 51-1 seems to display a similar deposition pattern as 51-2, Figure 7.8, and 51-3, Figure 7.9, meaning a uniform deposition along the filament.

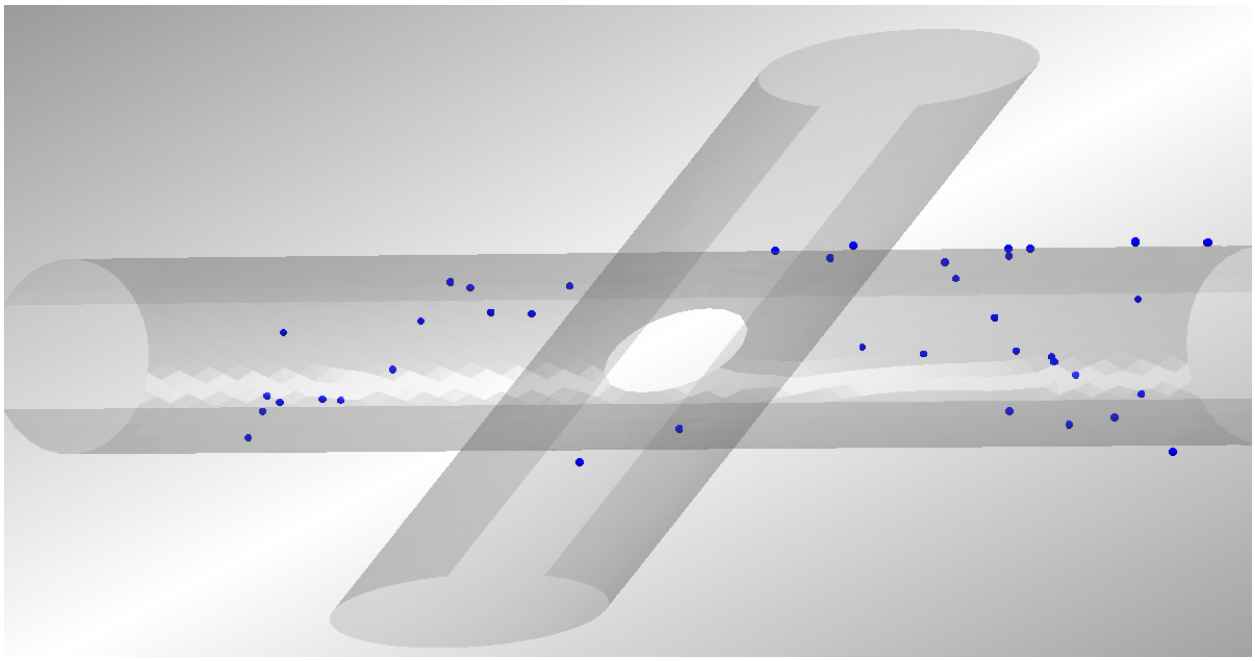

Figure 7.8: Deposition around Naltex 51-2 spacer joint

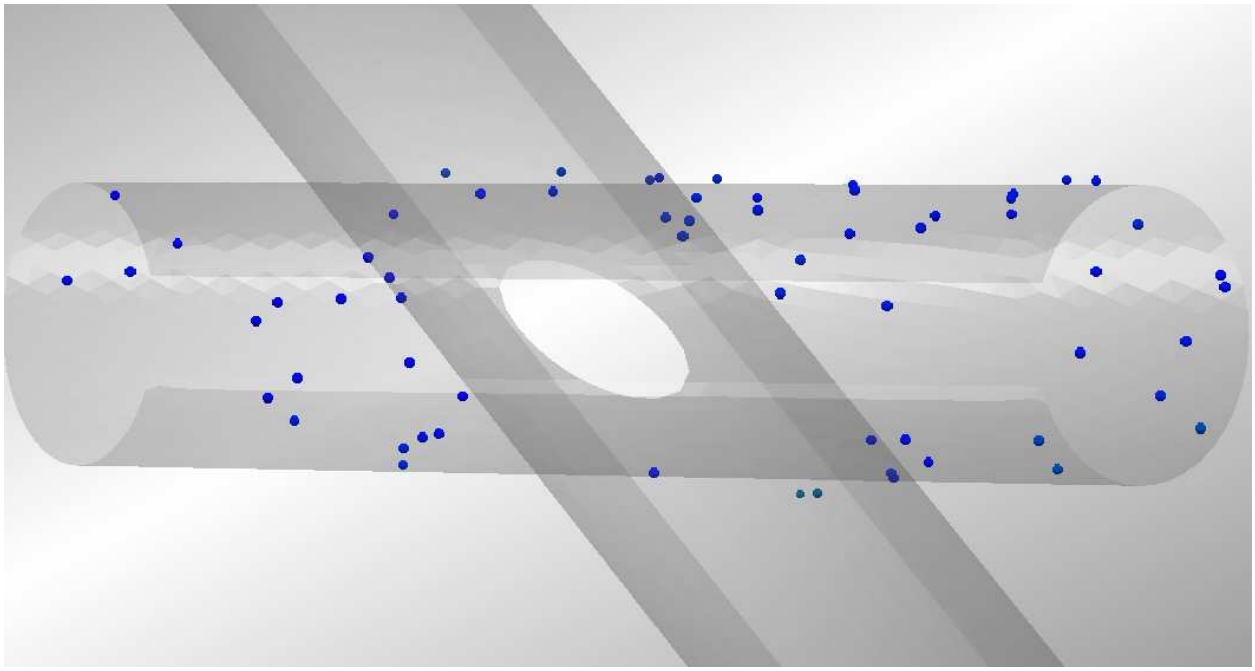

Figure 7.9: Deposition around Naltex 51-3 spacer joint

Although the spacer types are different, results show the same orientation sensitivity as experimental findings from Neal et al [137], who studied not the particle deposition on spacers but particle deposition in the gaps between them using square nets of equal sized filaments. Results from the present work are in agreement with Neal's work; both results show that deposition numbers depend on spacer orientation. In the current study, with the filaments arranged symmetrically around the flow direction (Naltex 51-1), deposition occurred particularly at the filament junction, whilst in configurations with filaments parallel to the flow (51-2 and 51-3), deposition occurs across the entire longitudinal filament, parallel to flow. Neal also observed a zone of no deposition at the back of the transverse filament; this does not appear in our simulations. However, in Neal et al's work this applied when filaments are at a 90° angle, which is not the case for Naltex 51 spacer configuration used in this work.

Figure 7.10 displays the numbers of deposited particles around the spacer join with respect to time, the curve being derived from the number of particle-to-wall contacts in the zone displayed in red on the top part of the figure. It can be seen that after the first wall-to-particle contact in the red zone at around 0.3, Naltex 51-1 displays a much greater rate of deposition than the other two spacer geometries. This is attributable to the fact that for the simulations of Naltex 51-2 and 51-3, particles deposit upon impact and stay relatively immobile. On the other hand, for Naltex 51-1, particles depositing at any location on a spacer can still subsequently move and collect at the join, which makes the deposited particle count around the junction increase significantly with appear to increase at a higher rate time.

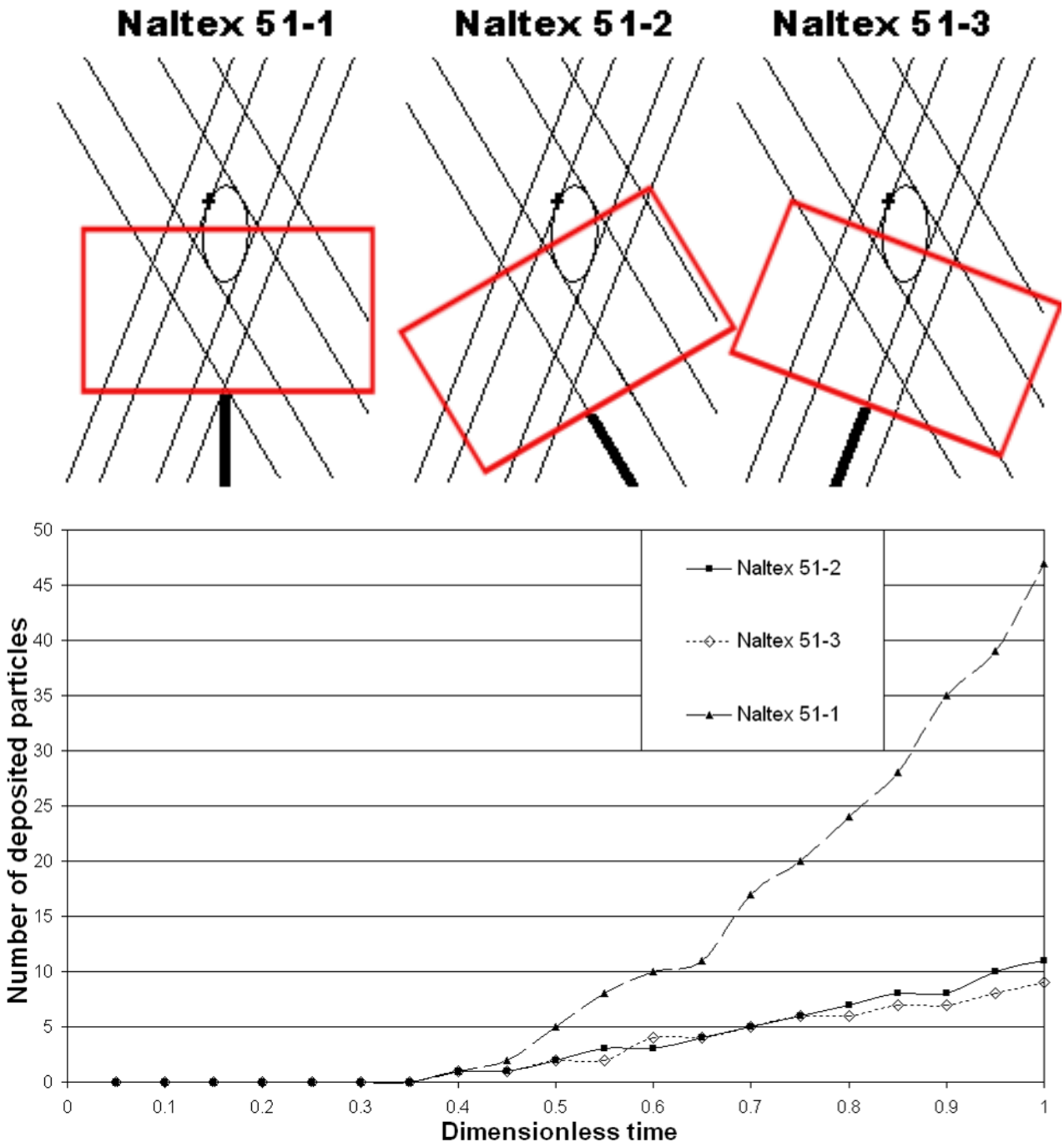

Figure 7.10: Evolution with time of deposited particles around spacer join

Vrouwenvelder's [142] experiments (Figure 7.11.A) shows deposition patterns similar to our simulation results. Where initial deposition occurring upstream of the spacer with a preferred deposition location at the spacer joint. Before, growth, propagation and colonisation occurs, which depend on nutrient availability, the initiation of bio-fouling is comparable (Figure 7.11) to the particulate deposition simulated in the current study.

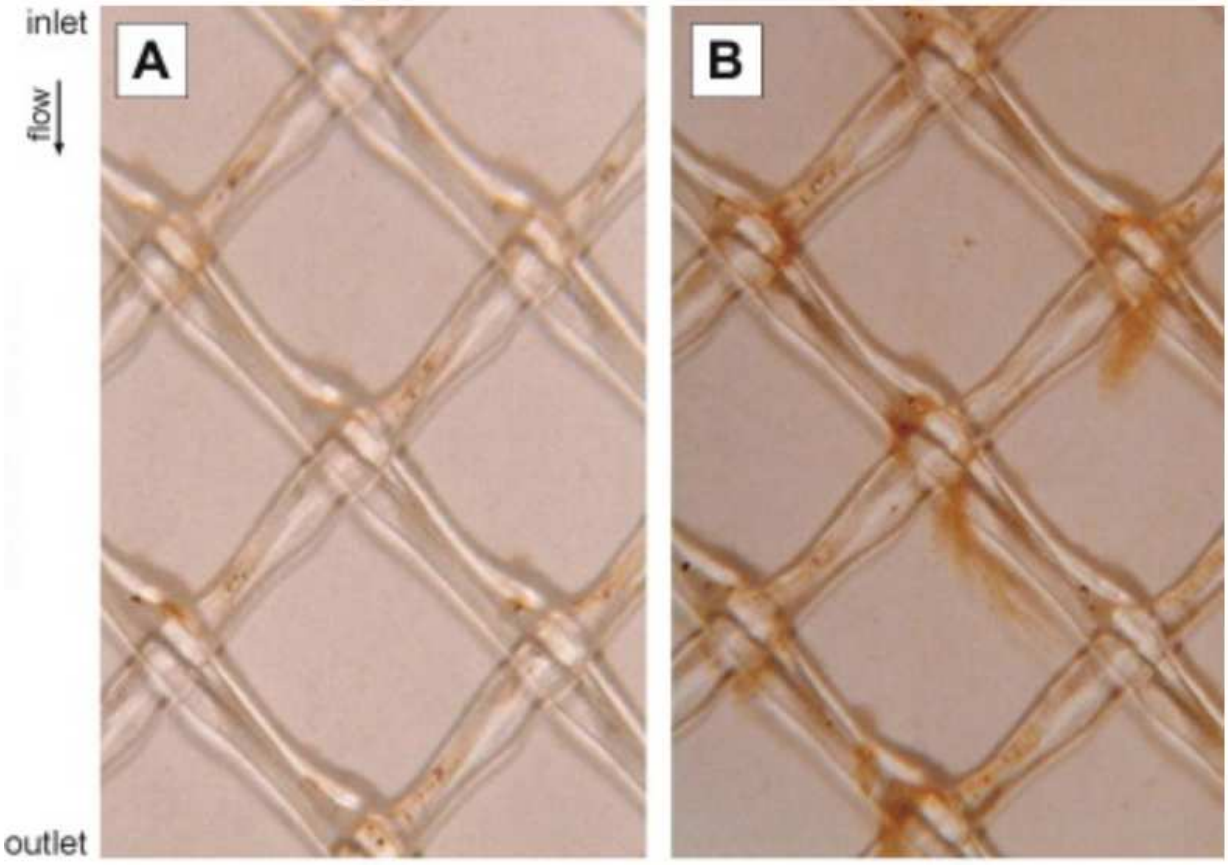

Figure 7.11: In-situ visual observations of the feed spacer and membrane without and with nutrient [142]

The observed fouling at the spacer junction agrees with some reports regarding microorganism deposition on spacers which state that the chance of attachment increases for decreasing values of shear stress around the obstacle [143, 144]. That would suggest increased deposition at regions of relatively low shear stress. The lowest shear is observed around the filament junction and away from spacer structures in between filament gaps, as shown in Figure 7.12.

It means that during initial deposition, adhesion simply occurs where the particles contact the filament, and tend to move in regions of low shear rate. The increase of biomass that occurs later compels the particles to shed in areas of lower shear strain (light green region between $-4s^{-1}$ and $2s^{-1}$ in Figure 7.12), toward the gaps between filaments, where the lower hydraulic forces do not break apart particle aggregates.

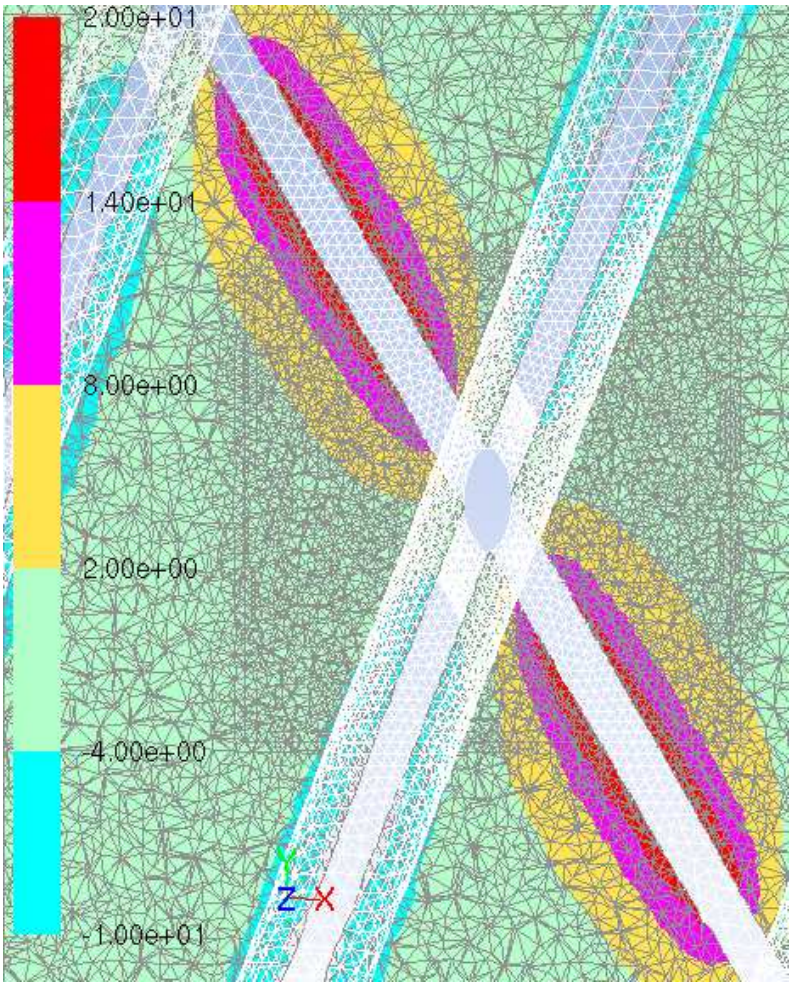

Figure 7.12: Shear rate contour around Naltex 51-1 spacer join

Under the flow, concentration and particle size conditions described in this work, very little particle-to-particle collision (Figure 7.13) could be observed. In the spacer feed channel, the ratio of particle volume to total volume was extremely small. Therefore, geometrical constraints were too low to induce bulk or surface cluster formation. Figure 7.13 shows a linear increase of inter-particle collision up to 0.45 of the total simulation time, which corresponds to the injected particles colliding amongst themselves up until they reach the filament junction. Then numbers drop as the un-deposited particles flow toward the outlet. That suggests that in these simulations, particle-to-particle collisions were not a significant factor for deposition

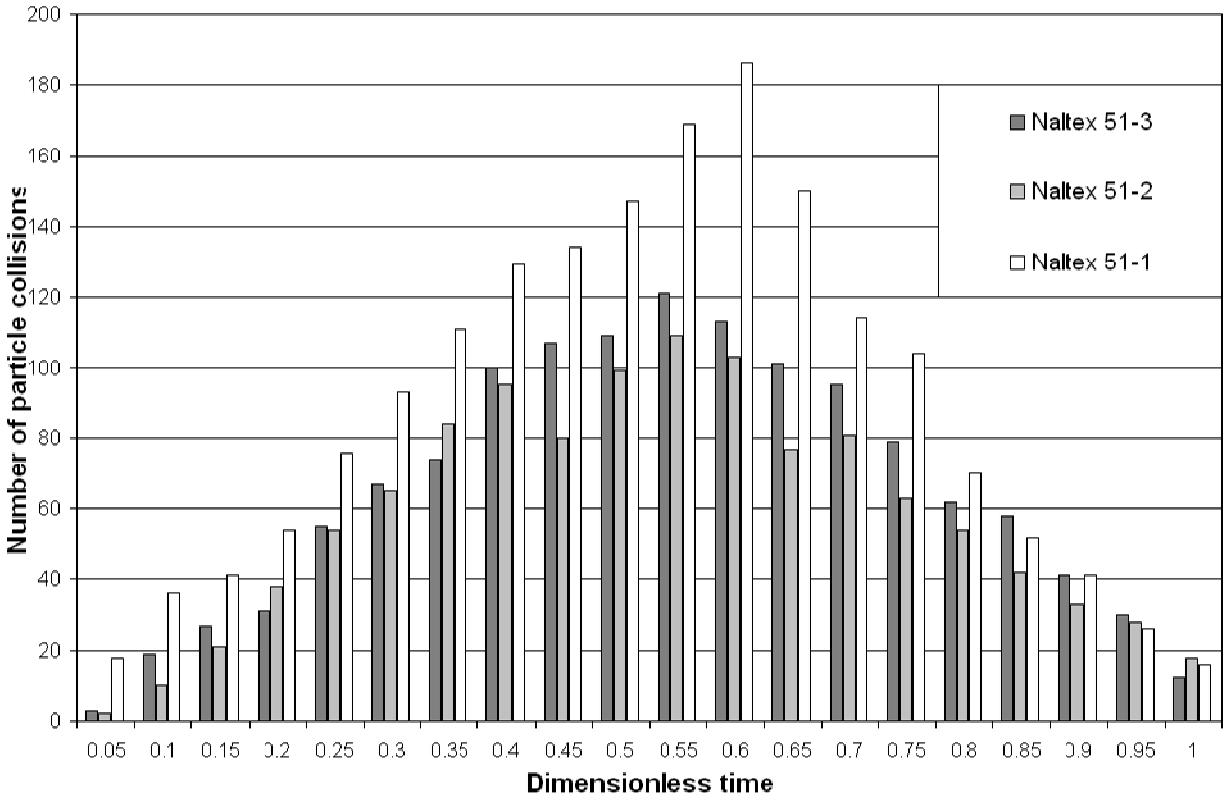

Figure 7.13: Comparison of particle collision around spacers

DEM-CFD method and EDEM post-processing capability allowed to follow the particle interactions with simulated structures and demonstrated that particle scale collisions were not significant for these simulations, but surface interaction models were still able to deposition pattern consistent with reported observations.

7. 5 Conclusion

This work reports a study of incipient colloidal fouling around feed channel spacers typical of a spiral wound membrane, and how deposition morphology changes with spacer filament orientation. DEM has been used with a one way CFD coupling, in order to simulate the initial bio-film formation on the commercial membrane spacer Naltex 51. It has been found that initial deposition pattern appear in region of low shear stresses, which agrees with reported experiments, and simulations. A preferred deposition patterns that depends on spacer orientation is also predicted, and particle accumulation around Naltex51-1 filament junction was simulated, which is in coherence with reported observations.

CHAPTER 8: Conclusions

This work presents a study on the applicability of the DEM-CFD method to simulate colloidal particles. Representative test cases were used to analyse the use of the DEM-CFD method at micro scale. Computation focused on simulating how micron-scale spherical latex particles immersed in water, agglomerate and deposit when flowing passed constraining geometries.

8. 1 Benefits of particle scale modelling

Particle scale modelling helped to understand the effect of particle-particle interaction, rolling effects and scouring mechanisms. Collision or near-contact relative motion was confirmed to play a key role in particle deposition and capture mechanisms. Interfacial force models allowed the removal of "stick upon contact" assumptions, which become inapplicable when a high number particle aggregate and break-off mechanism are expected to occur.

Particle scale point of view allowed implementing the interfacial force models and near contact hydraulics essential for flowing colloidal suspension modelling. Having a near contact detection radius bigger than the physical particle radius was a key feature that allowed such implementation.

The implementation technique was designed to remain as simple as possible using and customizing the commercially available software EDEM2.3 and FLUENT 12.0. Post-processing tools and correlation graphs were used to discuss and assess the validity of the particle scale mechanistic models to simulate aggregation and re-suspension in the same computational point of view. Results were presented in Chapter 6 and 7.

8. 2 Lessons learned

In Chapter 6, a series of particle scale simulations have been performed in order to model numerically flocculation and deposition of colloids in a constricted tube that can be seen as a single unit representation of a porous medium. The cluster formation, and particle deposition induced by the tube constriction were observed and analysed.

It was found that particle lateral displacement and migration result primarily from volume exclusion and collision that increase/decreases when ratio of total particle volume to fluid volume increases/decreases. Graphs displaying the evolution of the number of deposited particles in function of time were analysed to show the deposition and re-suspension behaviour of clusters of particles. Impact and scouring mechanisms were described and shown to induce non-linear deposition with respect to the total volume of injected particles. Increasing cluster sizes was linked to higher variability of deposited particle number. That was due to the competing effect of cluster formation, which increases interception rate but has an adverse effect on deposition through impact and scouring. Cluster rolling was described to occur under weak surface cohesion.

In terms of computational models, cluster formations and influence were shown to be insufficient to justify the use of two-way coupling. For the investigation of colloidal suspensions, the one-way DEM-CFD coupling was therefore preferred over the two-way coupling that was much more computationally expensive, without capturing the flow disturbance that was expected to alter the deposition numbers. It was observed that Brownian motion reduces the amount of deposited particles, because it applies mainly in non-favourable directions.

In Chapter 7, the one-way DEM-CFD technique is used to investigate how particles deposit around the filaments of spacers commonly used in membrane filtration systems. It gave indication on the onset of bio-film deposition around membrane spacers. The geometrical scale of simulation did not allow extended simulation time or high number of injected particles. Therefore, no cluster formation occurred because of the low concentration used. It has however been found that initial deposition patterns appear in region of low shear stresses, and simulations predicted particle accumulation around filament junction.

The particle scale modelling appeared very powerful to simulate and describe mechanistic processes involved in colloidal agglomeration and deposition. However, the restriction inherent to DEM-CFD imposed a few constrains that limited the scope of this work.

8. 3 Limitations of the work

In order cut the computational cost, the simulations presented were operated under a few limiting hypothesis. Particles were created within an inlet control window. Furthermore, the particle concentration was kept low in order for particles outside of the inlet window to have

a negligible impact on agglomeration and deposition. Furthermore, the deposition process could only be simulated on a short time scale, due to the time limit.

Forces between surfaces are as abundant as system and particle configuration types. This work constitutes a proof of concept that colloidal scale simulation can be performed via DEM-CFD methodology under the following restrictions:

- Small computational domain
- Short time scale
- Low particle concentration (due to inlet window hypothesis)
- Long range interaction forces restricted to near contact detection radius

8. 4 Suggested follow up

Further investigation would be needed in order to get rid of these restrictions, for example, more computational power, along with the appropriate populating model, would have allowed to simulate the bio-film growth and not only the initial deposition. That could be a useful tool for people who wish to control bio-fouling.

However, the method described in this work as it is could be extended to studies that would be more specific. For example, specialized simulations would include the electrostatic interaction in the DLVO model. That would allow simulating the agglomeration of particles that have surface charges. That would be useful in studying further microbial deposition.

In addition, it could be used to study the mitigation effect on aggregation and transport of adsorbed organic matter in colloids, which is a critical subject in soil and sediment science.

Furthermore, surface forces change drastically when polymers are adsorbed onto colloid surfaces or onto a membrane wall. This would cause aggregation dynamics to differ from the case where only the DLVO forces are significant. Further investigation would be needed to implement such interactions.

References

1. Fennell Evans, H.w., *The colloidal domain where physics, chemistry, biology and technology meet.* Wiley, 1999.
2. Larsen, A.E. and D.G. Grier, *Like-charge attractions in metastable colloidal crystallites.* Nature, 1997. **385**(6613): p. 230-233.
3. Metcalf and Eddy, *Wastewater Engineering : Treatment and reuse (4th Ed.)*, McGraw-Hill, 2002
4. Bacchin, P., P. Aimar, and V. Sanchez, *Model for colloidal fouling of membranes.* AIChE Journal, 1995. **41**(2): p. 368-376.
5. AWWA, A.W.W.A., *Water Quality and Treatment, A handbook of Community Water Supplies, Chapter 6: Coagulation and Flocculation Chapter 8: Granular bed and precoat filtration.* McGraw-Hill,1999.
6. Johnson, W.P., X. Li, and G. Yal, *Colloid Retention in Porous Media:â€‰ Mechanistic Confirmation of Wedging and Retention in Zones of Flow Stagnation.* Environmental Science & Technology, 2007. **41**(4): p. 1279-1287.
7. Ma, H., et al., *Hemispheres-in-Cell Geometry to Predict Colloid Deposition in Porous Media.* Environmental Science & Technology, 2009. **43**(22): p. 8573-8579.
8. Overbeek, E.J.W.V.a.J.T.G., *Theory of the Stability of Lyophobic Colloids.* Courier Dover 1948.
9. Van der Hoef, M.A., et al., *Numerical Simulation of Dense Gas-Solid Fluidized Beds: A Multiscale Modeling Strategy.* Annual Review of Fluid Mechanics, 2008. **40**(1): p. 47-70.
10. Woods, J.A., R.B. Thorpe, and S.E. Johnson, *Horizontal pneumatic conveying from a fluidized bed.* Chemical Engineering Science, 2008. **63**(7): p. 1741-1760.
11. Konstandopoulos, A.G., *Deposit growth dynamics: particle sticking and scattering phenomena.* Powder Technology, 2000. **109**(1-3): p. 262-277.
12. Rajagopalan, R. and C. Tien, *Trajectory analysis of deep-bed filtration with the sphere-in-cell porous media model.* AIChE Journal, 1976. **22**(3): p. 523-533.
13. Tien, C. and B.V. Ramarao, *The process of particle deposition in granular media: Description and formulation*, in *Granular Filtration of Aerosols and Hydrosols (Second Edition)*. 2007, Butterworth-Heinemann: Oxford. p. 337-403.
14. Kanaoka, C., S. Hiragi, and W. Tanthapanichakoon, *Stochastic simulation of the agglomerative deposition process of aerosol particles on an electret fiber.* Powder Technology, 2001. **118**(1-2): p. 97-106.
15. Li, S.Q. and J.S. Marshall, *Discrete element simulation of micro-particle deposition on a cylindrical fiber in an array.* Journal of Aerosol Science, 2007. **38**(10): p. 1031-1046.
16. Chang, Y.-I., et al., *A study on particle deposition morphology within a constricted tube in the presence and absence of the detachment mechanism.* Separation and Purification Technology, 2008. **63**(3): p. 566-576.
17. Huang, B., et al., *Experimental investigation on the particle capture by a single fiber using microscopic image technique.* Powder Technology, 2006. **163**(3): p. 125-133.
18. Hughes, D., et al., *In situ 3D characterization of membrane fouling by yeast suspensions using two-photon femtosecond near infrared non-linear optical imaging.* Journal of Membrane Science, 2006. **280**(1-2): p. 124-133.

19. Kuznar, Z.A. and M. Elimelech, *Direct microscopic observation of particle deposition in porous media: Role of the secondary energy minimum.* Colloids and Surfaces A: Physicochemical and Engineering Aspects, 2007. **294**(1-3): p. 156-162.
20. Hildich, R.G. and G.M. Zhang, *Internal fouling of microporous cross-flow filtration membranes with dilute latex suspensions.* The Chemical Engineering Journal and the Biochemical Engineering Journal, 1995. **60**(1-3): p. 31-37.
21. Echizen, H. and H. Unno, *Concentration of Fat Globules in Milk by an Oscillating Membrane Unit: Experiment Using Model Emulsified Solutions.* Food and Bioproducts Processing, 2001. **79**(1): p. 3-12.
22. Johnson, W.P., E. Pazmino, and H. Ma, *Direct observations of colloid retention in granular media in the presence of energy barriers, and implications for inferred mechanisms from indirect observations.* Water Research. **44**(4): p. 1158-1169.
23. Chang, Y.I., S.C. Chen, and E. Lee, *Prediction of Brownian particle deposition in porous media using the constricted tube model.* Journal of Colloid and Interface Science, 2003. **266**(1): p. 48-59.
24. Duursma, G., et al., *DEM-CFD Modelling of Voidage and Heat Transfer in Fluidized Beds*, in *8th World Congress on Chemical Engineering*. 2009: Montreal, Canada.
25. Johnson, W.P., X. Li, and S. Assemi, *Deposition and re-entrainment dynamics of microbes and non-biological colloids during non-perturbed transport in porous media in the presence of an energy barrier to deposition.* Advances in Water Resources. **30**(6-7): p. 1432-1454.
26. Kuznar, Z.A. and M. Elimelech, *Adhesion Kinetics of Viable Cryptosporidium parvum Oocysts to Quartz Surfaces.* Environmental Science & Technology, 2004. **38**(24): p. 6839-6845.
27. Happel, J., *Viscous flow in multiparticle systems: Slow motion of fluids relative to beds of spherical particles.* AIChE Journal, 1958. **4**(2): p. 197-201.
28. Nelson, K.E. and T.R. Ginn, *Colloid Filtration Theory and the Happel Sphere-in-Cell Model Revisited with Direct Numerical Simulation of Colloids.* Langmuir, 2005. **21**(6): p. 2173-2184.
29. Shams, M., G. Ahmadi, and H. Rahimzadeh, *A sublayer model for deposition of nano- and micro-particles in turbulent flows.* Chemical Engineering Science, 2000. **55**(24): p. 6097-6107.
30. Cundall, P.A. and O.D.L. Strack, *A discrete numerical model for granular assemblies.* Géotechnique, 1979. **29**(1): p. 47-65.
31. Yasuda, R., T. Harada, and Y. Kawaguchi. *Real-Time Simulation of Granular Materials Using Graphics Hardware*. in *Computer Graphics, Imaging and Visualisation, 2008. CGIV '08. Fifth International Conference on*. 2008.
32. Rapaport, D.C., *The Art of Molecular Dynamics Simulation.* Cambridge University Press; 2nd edition, 2004.
33. Luding, S., *Molecular Dynamics Simulations of Granular Materials*, in *The Physics of Granular Media*. 2005, Wiley-VCH Verlag GmbH & Co. KGaA. p. 297-324.
34. Ristow, G.H. *Granular Dynamics: A Review about recent Molecular Dynamics Simulations of Granular Materials*. in *Ann. Rev. of Comput. Phys. I*. 1994: World Scientific.
35. DEMSolutionsLtd., *EDEM 2.3 user-manual*. 2011.
36. Luding, S., *http://www2.msm.ctw.utwente.nl/sluding/TEACHING/ParticleTechnology/Luding_PForcesModels.pdf*.

37. Hoffmann, R., *DEM Simulations of Toner Particles with an O (N log N) Hierarchical Tree Code Algorithm.* Granular Matter, 2006. **8**(3): p. 151-157.
38. Hoomans, *Granular dynamics of gas-solid two-phase flows.* PhD thesis, University of Twente, 2000.
39. van der Hoef, M.A., et al., *Multiscale Modeling of Gas-Fluidized Beds*, in *Advances in Chemical Engineering*. 2006, Academic Press. p. 65-149.
40. DEMSolutionsLtd., *EDEM 2.1.2 user-guide.* 2011: p. 109.
41. Alizadeh, E., F.o. Bertrand, and J. Chaouki, *Development of a granular normal contact force model based on a non-Newtonian liquid filled dashpot.* Powder Technology. **237**(0): p. 202-212.
42. Di Renzo, A. and F.P. Di Maio, *Comparison of contact-force models for the simulation of collisions in DEM-based granular flow codes.* Chemical Engineering Science, 2004. **59**(3): p. 525-541.
43. Ning, Z., et al., *Distinct element simulation of impact breakage of lactose agglomerates.* Advanced Powder Technology, 1997. **8**(1): p. 15-37.
44. Radl, S., et al., *Mixing characteristics of wet granular matter in a bladed mixer.* Powder Technology, 2010. **200**(3): p. 171-189.
45. Cook, R., et al., *Concepts and applications of finite element analysis*. 2002: John Wiley and Sons. Inc.
46. Johnson, S.M., J.R. Williams, and B.K. Cook, *Quaternion-based rigid body rotation integration algorithms for use in particle methods.* International Journal for Numerical Methods in Engineering, 2008. **74**(8): p. 1303-1313.
47. Das, A.K. and P.K. Das, *Bubble evolution through submerged orifice using smoothed particle hydrodynamics: Basic formulation and model validation.* Chemical Engineering Science, 2009. **64**(10): p. 2281-2290.
48. Elimelech, M., et al., *Particle Deposition and Aggregation - Measurement, Modelling and Simulation _ Chapter 4*. 1998, Elsevier.
49. Patankar, S.V. and D.B. Spalding, *A calculation procedure for heat, mass and momentum transfer in three-dimensional parabolic flows.* International Journal of Heat and Mass Transfer, 1972. **15**(10): p. 1787-1806.
50. Versteeg, H.K. and W. Malalasekera, *An Introduction to Computational Fluid Dynamics, The finite Volume Method*. 1995: Prentice Hall.
51. Zhu, H.P., et al., *Discrete particle simulation of particulate systems: Theoretical developments.* Chemical Engineering Science, 2007. **62**(13): p. 3378-3396.
52. Cloete, S., S.T. Johansen, and S. Amini, *Performance evaluation of a complete Lagrangian KTGF approach for dilute granular flow modelling.* Powder Technology, 2012. **226**(0): p. 43-52.
53. Delnoij, E., J.A.M. Kuipers, and W.P.M. van Swaaij, *A three-dimensional CFD model for gas-liquid bubble columns.* Chemical Engineering Science, 1999. **54**(13-14): p. 2217-2226.
54. Coetzee, W., R.L.J. Coetzer, and R. Rawatlal, *Semianalytical Bubble-Flow Models for the Development of a Novel Bubble-Column Simulator.* Industrial & Engineering Chemistry Research, 2012. **51**(21): p. 7398-7409.
55. Kuipers, J.A.M., et al., *A numerical model of gas-fluidized beds.* Chemical Engineering Science, 1992. **47**(8): p. 1913-1924.
56. Elghobashi, S., *Particle-laden turbulent flows: direct simulation and closure models.* Applied Scientific Research, 1991. **48**(3): p. 301-314.

57. Kawaguchi, T., T. Tanaka, and Y. Tsuji, *Numerical simulation of two-dimensional fluidized beds using the discrete element method (comparison between the two- and three-dimensional models).* Powder Technology, 1998. **96**(2): p. 129-138.
58. DEMSolutionsLtd., *EDEM CFD Coupling Interface: Programming Guide.* 2012.
59. Liang, Y., et al., *Interaction forces between colloidal particles in liquid: Theory and experiment.* Advances in Colloid and Interface Science, 2007. **134-135**(0): p. 151-166.
60. Lemos, M.J.S.d., *Overview*, in *Turbulence in Porous Media*. 2006, Elsevier Science Ltd: Oxford. p. ix-x.
61. Netz, R., *Sources for ancient science.* Endeavour, 2000. **24**(2): p. 53-54.
62. Noel, R.N.W., *The Archimedes Codex: How a Medieval Prayer Book Is Revealing the True Genius of Antiquity's Greatest Scientist.* The Orion Publishing Group, 2007. **1-2**.
63. Crowe, C.T.S., M.; Tsuji, Y., *Multiphase Flow with Droplets and Particles.* 1998.
64. Ergun, S., *Fluid flow through packed columns.* Chem. Eng. Prog., 1952. **48**: p. 89.
65. Wen, C. and Y. Yu, *Mechanics of fluidization.* Chem. Eng. Prog. Symp. Ser, 1966 **62**(62): p. 100.
66. Niven, R.K., *Physical insight into the Ergun and Wen & Yu equations for fluid flow in packed and fluidised beds.* Chemical Engineering Science, 2002. **57**(3): p. 527-534.
67. Di Felice, R., *The voidage function for fluid-particle interaction systems.* International Journal of Multiphase Flow, 1994. **20**(1): p. 153-159.
68. Pang, M.J. and J.J. Wei, *Analysis of drag and lift coefficient expressions of bubbly flow system for low to medium Reynolds number.* Nuclear Engineering and Design, 2011. **241**(6): p. 2204-2213.
69. Hibiki, T. and M. Ishii, *Lift force in bubbly flow systems.* Chemical Engineering Science, 2007. **62**(22): p. 6457-6474.
70. Dijkhuizen, W., M. van Sint Annaland, and J.A.M. Kuipers, *Numerical and experimental investigation of the lift force on single bubbles.* Chemical Engineering Science, 2010. **65**(3): p. 1274-1287.
71. Ookawara, S., et al., *Quasi-direct numerical simulation of lift force-induced particle separation in a curved microchannel by use of a macroscopic particle model.* Chemical Engineering Science, 2007. **62**(9): p. 2454-2465.
72. Wang, Q., et al., *On the role of the lift force in turbulence simulations of particle deposition.* International Journal of Multiphase Flow, 1997. **23**(4): p. 749-763.
73. Lataste, J., et al., *On the shear lift force acting on heavy particles in a turbulent boundary layer.* Atmospheric Environment, 2000. **34**(23): p. 3963-3971.
74. Hall, D., *Measurements of the mean force on a particle near a boundary in turbulent flow.* Journal of Fluid Mechanics, 1988. **187**: p. 451-466.
75. Drew, D.A., *The lift force on a small sphere in the presence of a wall.* Chemical Engineering Science, 1988. **43**(4): p. 769-773.
76. Sangani, et al., *An O(N) algorithm for Stokes and Laplace interactions of particles*. Vol. 8. 1996, Melville, NY, ETATS-UNIS: American Institute of Physics. 21.
77. Pasol, L., et al., *Analytical solutions for a spherical particle near a wall in axisymmetrical polynomial creeping flows.* Physics of Fluids, 2005. **17**(7).
78. Brenner, H., *The slow motion of a sphere through a viscous fluid towards a plane surface.* Chemical Engineering Science, 1961. **16**(3-4): p. 242-251.
79. Goldman, A.J., R.G. Cox, and H. Brenner, *Slow viscous motion of a sphere parallel to a plane wall--I Motion through a quiescent fluid.* Chemical Engineering Science, 1967. **22**(4): p. 637-651.
80. Goldman, A.J., R.G. Cox, and H. Brenner, *Slow viscous motion of a sphere parallel to a plane wall--II Couette flow.* Chemical Engineering Science, 1967. **22**(4): p. 653-660.

81. Brenner, H., *The slow motion of a sphere through a viscous fluid towards a plane surface.* Chemical Engineering Science, 1961. **16**(3-4): p. 242-251.
82. Haberman, W. and R.M. Sayre, *Motion of Rigid and FluidSpheres in Stationary and Moving liquids inside Cylindrical Tubes.* PhD thesis, 1958. **U.S. Navy Department, Washington D.C**.
83. Nguyen, A.V. and G.M. Evans, *Exact and approximate expressions for resistance coefficients of a colloidal sphere approaching a solid surface at intermediate Reynolds numbers.* Applied Mathematical Modelling, 2007. **31**(4): p. 763-769.
84. A., L.H., Abh. theoret. Phys, 1907. **1 23**.
85. Adamczyk, Z., M. Adamczyk, and T.G.M. van de Ven, *Resistance coefficient of a solid sphere approaching plane and curved boundaries.* Journal of Colloid and Interface Science, 1983. **96**(1): p. 204-213.
86. Maude, A.D., *End effects in a falling-sphere viscometer.* British Journal of Applied Physics, 1961. **12**(6): p. 293.
87. Chein, R. and W. Liao, *Analysis of particle-wall interactions during particle free fall.* Journal of Colloid and Interface Science, 2005. **288**(1): p. 104-113.
88. Odar, F. and W. Hamilton, *Forces on a sphere accelerating in a viscous fluid.* Journal of Fluid Mechanics, 1964. **18**(02): p. 302-314.
89. Basset, A.B., *A Treatise on Hydrodynamics, Volume 2.* 1888.
90. Candelier, F., J.R. Angilella, and M. Souhar, *On the effect of the Boussinesq--Basset force on the radial migration of a Stokes particle in a vortex.* Physics of Fluids, 2004. **16**(5): p. 1765-1776.
91. Hjelmfelt, A. and L. Mockros, *Motion of discrete particles in a turbulent fluid.* Applied Scientific Research, 1966. **16**(1): p. 149-161.
92. Johnson, R.W., *Handbook of Fluid Dynamics 18-4.* CRC Press, 1998.
93. Ounis, H., G. Ahmadi, and J.B. McLaughlin, *Brownian diffusion of submicrometer particles in the viscous sublayer.* Journal of Colloid and Interface Science, 1991. **143**(1): p. 266-277.
94. Farinato, R.S. and P.L. Dubin, *Colloid-Polymer Interactions: From Fundamentals to Practice.* Wiley, 1999.
95. Rafael, T., *The London-van der Waals interaction energy between objects of various geometries.* Journal of Physics: Condensed Matter, 2001. **13**(9): p. L195.
96. London, F., *Zur Theorie und Systematik der Molekularkrafte.* Zeitschrift fur Physik, 1930. **63**(3-4): p. 245-279.
97. Prieve, D.C. and W.B. Russel, *Simplified predictions of Hamaker constants from Lifshitz theory.* Journal of Colloid and Interface Science, 1988. **125**(1): p. 1-13.
98. Johnson, W.P., X. Li, and G. Yal, *Colloid Retention in Porous Media: Mechanistic Confirmation of Wedging and Retention in Zones of Flow Stagnation (supporting information page 7).* Environmental Science & Technology, 2007. **41**(4): p. 1279-1287.
99. Gregory, J., *Approximate expressions for retarded van der waals interaction.* Journal of Colloid and Interface Science, 1981. **83**(1): p. 138-145.
100. Hogg, R., T.W. Healy, and Fuersten.Dw, *Mutual Coagulation of Colloidal Dispersions.* Transactions of the Faraday Society, 1966. **62**(522P): p. 1638-&.
101. Weronski, P. and M. Elimelech, *Novel numerical method for calculating initial flux of colloid particle adsorption through an energy barrier.* Journal of Colloid and Interface Science, 2008. **319**(2): p. 406-415.
102. Ma, H.L. and W.P. Johnson, *Colloid Retention in Porous Media of Various Porosities: Predictions by the Hemispheres-in-Cell Model.* Langmuir, 2009. **26**(3): p. 1680-1687.

103. Ma, H., et al., *Hemispheres-in-Cell Geometry to Predict Colloid Deposition in Porous Media: supporting information.* Environmental Science & Technology, 2009. **43**(22): p. 8573-8579.
104. Naumov, V.A., *Influence of Saffman's lift force on the motion of a particle in a Couette layer.* Journal of Engineering Physics and Thermophysics, 1995. **68**(5): p. 683-686.
105. DEMSolutionsLtd., www.dem-solutions.com.
106. P.A, C., *Formulation of a three-dimensional distinct element model - Part I. A scheme to detect and represent contacts in a system composed of many polyhedral blocks.* International Journal of Rock Mechanics and Mining Sciences & Geomechanics Abstracts, 1988. **25**(3): p. 107-116.
107. Raji, A.O. and J.F. Favier, *Model for the deformation in agricultural and food particulate materials under bulk compressive loading using discrete element method. I: Theory, model development and validation.* Journal of Food Engineering, 2004. **64**(3): p. 359-371.
108. Vetterling, W.T. and W.H. Press, *Numerical recipes example book (C++)*, Cambridge University Press; 2nd edition, 2002.
109. Bhattacharjee, S., C.H. Ko, and M. Elimelech, *DLVO interaction between rough surfaces.* Langmuir, 1998. **14**(12): p. 3365-3375.
110. Peng, Z., E. Doroodchi, and G. Evans, *DEM simulation of aggregation of suspended nanoparticles.* Powder Technology, 2010. **204**(1): p. 91-102.
111. Jing, L., O. Stephansson, and S. Lanru Jing and Ove, *Discrete Element Methods for Granular Materials*, in *Developments in Geotechnical Engineering*. 2007, Elsevier. p. 399-444.
112. Yoshida, H. and C. Tien, *Analysis of Brownian particle deposition and reentrainment in granular beds.* Journal of Colloid and Interface Science, 1986. **111**(1): p. 189-196.
113. Marshall, J.S., *Particle aggregation and capture by walls in a particulate aerosol channel flow.* Journal of Aerosol Science, 2007. **38**(3): p. 333-351.
114. chaumeil, f., *http://www.see.ed.ac.uk/~s0925077/video/R1-c5e3-v001.wmv.* 2012.
115. chaumeil, f., *http://www.see.ed.ac.uk/~s0925077/video/R1-V002-c1e4.wmv.* 2012.
116. chaumeil, f., *http://www.see.ed.ac.uk/~s0925077/video/r1-c2e3-v001.wmv.* 2012.
117. Champlin, T.L., *Using circulation tests to model natural organic matter adsorption and particle deposition by spiral-wound nanofiltration membrane elements.* Desalination, 2000. **131**(1-3): p. 105-115.
118. Altmann, J. and S. Ripperger, *Particle deposition and layer formation at the crossflow microfiltration.* Journal of Membrane Science, 1997. **124**(1): p. 119-128.
119. Pak, A., et al., *CFD modeling of porous membranes.* Desalination, 2008. **222**(1-3): p. 482-488.
120. Zimmerer, C.C. and V. Kottke, *Effects of spacer geometry on pressure drop, mass transfer, mixing behavior, and residence time distribution.* Desalination, 1996. **104**(1-2): p. 129-134.
121. Ngene, I.S., et al., *Particle deposition and biofilm formation on microstructured membranes.* Journal of Membrane Science. **364**(1-2): p. 43-51.
122. Da Costa, A.R., A.G. Fane, and D.E. Wiley, *Spacer characterization and pressure drop modelling in spacer-filled channels for ultrafiltration.* Journal of Membrane Science, 1994. **87**(1-2): p. 79-98.
123. Maharudrayya, S., S. Jayanti, and A.P. Deshpande, *Pressure losses in laminar flow through serpentine channels in fuel cell stacks.* Journal of Power Sources, 2004. **138**(1-2): p. 1-13.

124. Li, F., et al., *Optimization of commercial net spacers in spiral wound membrane modules.* Journal of Membrane Science, 2002. **208**(1-2): p. 289-302.
125. Li, F., et al., *Experimental validation of CFD mass transfer simulations in flat channels with non-woven net spacers.* Journal of Membrane Science, 2004. **232**(1-2): p. 19-30.
126. Karode, S.K. and A. Kumar, *Flow visualization through spacer filled channels by computational fluid dynamics I.: Pressure drop and shear rate calculations for flat sheet geometry.* Journal of Membrane Science, 2001. **193**(1): p. 69-84.
127. Wiley, D.E. and D.F. Fletcher, *Techniques for computational fluid dynamics modelling of flow in membrane channels.* Journal of Membrane Science, 2003. **211**(1): p. 127-137.
128. Shakaib, M., S.M.F. Hasani, and M. Mahmood, *CFD modeling for flow and mass transfer in spacer-obstructed membrane feed channels.* Journal of Membrane Science, 2009. **326**(2): p. 270-284.
129. Shakaib, M., S.M.F. Hasani, and M. Mahmood, *Study on the effects of spacer geometry in membrane feed channels using three-dimensional computational flow modeling.* Journal of Membrane Science, 2007. **297**(1-2): p. 74-89.
130. Wardeh, S. and H.P. Morvan, *CFD simulations of flow and concentration polarization in spacer-filled channels for application to water desalination.* Chemical Engineering Research and Design, 2008. **86**(10): p. 1107-1116.
131. Cao, Z., D.E. Wiley, and A.G. Fane, *CFD simulations of net-type turbulence promoters in a narrow channel.* Journal of Membrane Science, 2001. **185**(2): p. 157-176.
132. Ahmad, A.L. and K.K. Lau, *Impact of different spacer filaments geometries on 2D unsteady hydrodynamics and concentration polarization in spiral wound membrane channel.* Journal of Membrane Science, 2006. **286**(1-2): p. 77-92.
133. Ahmad, A.L., et al., *Integrated CFD simulation of concentration polarization in narrow membrane channel.* Computers & Chemical Engineering, 2005. **29**(10): p. 2087-2095.
134. Vrouwenvelder, J.S., et al., *A critical flux to avoid biofouling of spiral wound nanofiltration and reverse osmosis membranes: Fact or fiction?* Journal of Membrane Science, 2009. **326**(1): p. 36-44.
135. Bos, R., H.C. van der Mei, and H.J. Busscher, *Physico-chemistry of initial microbial adhesive interactions – its mechanisms and methods for study.* FEMS Microbiology Reviews, 1999. **23**(2): p. 179-230.
136. Schäfer, A.I., A.G. Fane, and T.D. Waite, *Nanofiltration: Principles and Application.* Elsevier Science, 2005.
137. Neal, P.R., et al., *The effect of filament orientation on critical flux and particle deposition in spacer-filled channels.* Journal of Membrane Science, 2003. **214**(2): p. 165-178.
138. Vrouwenvelder, J.S., et al., *Biofouling in spiral wound membrane systems: Three-dimensional CFD model based evaluation of experimental data.* Journal of Membrane Science, 2010. **346**(1): p. 71-85.
139. Costerton, J.W., P.S. Stewart, and E.P. Greenberg, *Bacterial Biofilms: A Common Cause of Persistent Infections.* Science, 1999. **284**(5418): p. 1318-1322.
140. Li, Y.-L. and K.-L. Tung, *CFD simulation of fluid flow through spacer-filled membrane module: selecting suitable cell types for periodic boundary conditions.* Desalination, 2008. **233**(1-3): p. 351-358.
141. Rahimi, M., S.S. Madaeni, and K. Abbasi, *CFD modeling of permeate flux in cross-flow microfiltration membrane.* Journal of Membrane Science, 2005. **255**(1-2): p. 23-31.
142. Vrouwenvelder, J.S., et al., *Biofouling of spiral-wound nanofiltration and reverse osmosis membranes: A feed spacer problem.* Water Research, 2009. **43**(3): p. 583-594.
143. Knutsen, J.S. and R.H. Davis, *Deposition of foulant particles during tangential flow filtration.* Journal of Membrane Science, 2006. **271**(1-2): p. 101-113.

144. Rahimi, M., et al., *CFD and experimental studies of fouling of a microfiltration membrane.* Chemical Engineering and Processing: Process Intensification, 2009. **48**(9): p. 1405-1413.
145. Chaumeil, F. and M. Crapper, *DEM simulations of initial deposition of colloidal particles around non-woven membrane spacers.* Journal of Membrane Science, 2013. **442**(0): p. 254-263.

List of figures

List of tables

APPENDIX A: Derivation of Van-der-Waals interactions for various objects

According to London's theory, the universal Van der Waals forces between two atoms will be proportional to r^{-7}. The corresponding attractive potential therefore varies as

$$E_{pot} = -\frac{\lambda}{h^6}$$

According to the definition by Verwey and Overbeek, we shall replace the discrete summation individual contribution by a continuous integral over the atomic assembly since assemblies of colloidal dimension are big enough and their distance from each other is big compared to atomic dimensions.

A. 1 Interaction between an atom and a circular surface, first way

Let us consider an infinitesimal flat annulus of radius h and width dh, at a distance r from an atom. Then its surface (Pappus's theorem) is $2.\pi.h.dh$, let us define s, the number density of atom per surface unit. Then we can compute that the force induced by i annulus on an atom at distance X is the summation of all the forces between the on atom and the atom from the annulus:

$$df_{atom}^{annulus} = f_{pair}.s.2\pi.h.dh.\cos\theta = \frac{6\lambda}{r^7}\frac{X}{r}.s.2\pi.h.dh$$

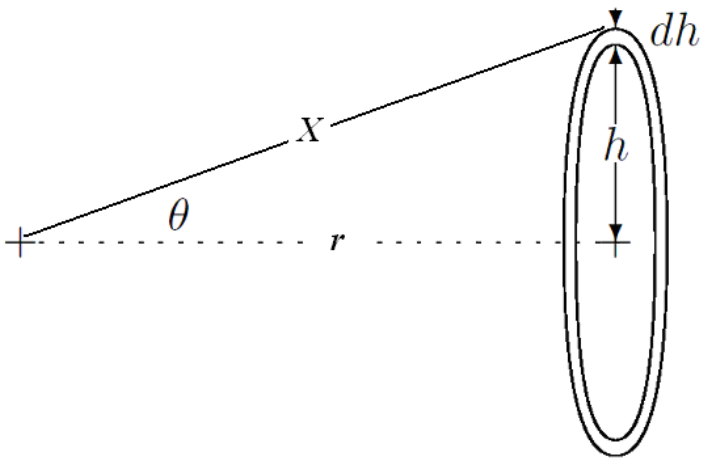

In order to obtain the total force induced by an infinitely flat circular disc of radius R we just have to integrate this infinitesimal expression between 0 and R. Let us remember that $r2=h2+X2$.

$$f_{atom}^{disc} = 6.s.\pi.\lambda.X.\int_{h=0}^{R}\frac{2h}{r^8}dh = 6.s.\pi.\lambda.X.\int_{h=0}^{R}\frac{2h}{\left(h^2+x^2\right)^4}dh = 2.s.\pi.\lambda.X\left[\frac{1}{X^6}-\frac{1}{\left(R^2+X^2\right)^3}\right]$$

A. 2 Interaction between an atom and a circular surface, second way

The reasoning presented above is the one used by Verwey and Overbeek, another way of addressing the problem of a flat circular surface interacting with an atom is to use a trigonometric formulation. The infinitesimal circular surface is still:

$$df_{atom}^{annulus} = f_{pair}.s.2\pi.h.dh.\cos\theta = \frac{6\lambda}{r^7}.s.2\pi.h.dh.\cos\theta$$

But this time instead of integrating over h let us integrate over θ given that $tan(\theta)=h/X$ and $cos\theta=X/r$. So that:

$$\frac{dh}{d\theta} = \frac{X}{\cos^2\theta}$$

Then

$$df_{atom}^{annulus} = 6.s.2\pi.\lambda.X.\sin\theta\frac{\cos^5\theta}{X^5}d\theta$$

And

$$f_{atom}^{disc} = \frac{6.s.2\pi.\lambda}{X^5}.\int_{\theta=0}^{\theta=\arctan\frac{R}{X}}\sin\theta.\cos^5\theta d\theta = \frac{s.2\pi.\lambda}{X^5}\left[1-\frac{1}{\left(1+\frac{R^2}{X^2}\right)^3}\right]$$

This confirms the previous expression

A. 3 Interaction between an atom and a circular plate

Now in order to obtain the force between an atom and a circular plate of thickness δ, let us define l the density number of atoms per unit of length and integrate the above expression with respect to X over the thickness of the plate δ.

$$f_{atom}^{circ\ plate} = l.2.s.\pi.\lambda.\int_X^{X+\delta} \frac{1}{X^5} - \frac{X}{\left(R^2+X^2\right)^3} dX = -\frac{l.s.\pi.\lambda}{2}\left[\frac{1}{X^4} - \frac{1}{\left(R^2+X^2\right)^2}\right]_X^{X+\delta}$$

$$f_{atom}^{circ\ plate} = \frac{l.s.\pi.\lambda}{2}\left[\frac{1}{X^4} - \frac{1}{\left(R^2+X^2\right)^2} - \frac{1}{\left(X+\delta\right)^4} + \frac{1}{\left(R^2+\left(X+\delta\right)^2\right)^2}\right]$$

The interaction between an atom and an infinite plate derives from the above expression when R is much bigger than X so that the equation simplifies as:

$$f_{atom}^{\inf\ plate} = \frac{l.s.\pi.\lambda}{2}\left[\frac{1}{X^4} - \frac{1}{\left(X+\delta\right)^4}\right]$$

A. 4 Interaction between a row of atoms and an infinite plate

Now let us consider a row of atom made from sweeping the above single atom over a distance δ in the opposite direction of the plate, and define l the number of atoms per unit of length so that the number of atoms in an elementary section dR of the row is $l.dR$. Once again, the interaction between that row and the thick plate is obtained by integration.

$$f_{row}^{\inf\ plate} = \frac{l.s.\pi.\lambda}{2}.\int_R^{R+\delta} \frac{1}{R^4} - \frac{1}{\left(R+\delta\right)^4} dR$$

$$f_{row}^{\inf\ plate} = \frac{l.s.\pi.\lambda}{6}.\left[\frac{1}{R^3} + \frac{1}{\left(R+2\delta\right)^3} - \frac{2}{\left(R+\delta\right)^3}\right]$$

A. 5 Interaction between two plates

The interaction between two infinite thick plates is just the sum over an infinite number of rows that are constantly separated by a distance R from the surface of the original plate. Let us define s the number of rows per unit of surface so that $n=s.l$. This time the invariance principle makes the integration even easier as it consist in adding always the same amount, and the total force per unit of area between two plates of thickness δ is:

$$f_{plates} = \frac{n^2.\pi.\lambda}{6}.\left[\frac{1}{R^3} + \frac{1}{(R+2\delta)^3} - \frac{2}{(R+\delta)^3}\right]$$

Although force quantities are instinctively easier to understand, most publications will only describe interactions in term of potential (or free energy). Where the potential can be derived from the force from the simple formula:

$$f = -\nabla E_{pot}$$

Therefore, the expression of the interaction potential is given by:

$$E_{pot} = -\int_R^\infty f_{plates} = -\frac{n^2.\pi.\lambda}{6}.\int_R^\infty \frac{1}{R^3} + \frac{1}{(R+2\delta)^3} - \frac{2}{(R+\delta)^3}\,dR$$

$$E_{pot} = \frac{n^2.\pi.\lambda}{12}.\left[\frac{1}{R^2} + \frac{1}{(R+2\delta)^2} - \frac{2}{(R+\delta)^2}\right]$$

Hamaker defined the quantity $H=n^2\pi^2\lambda$ that describes the properties of the material of the interacting objects. Introducing that quantity in the above expression, gives:

$$E_{pot} = \frac{H}{12\pi}.\left[\frac{1}{R^2} + \frac{1}{(R+2\delta)^2} - \frac{2}{(R+\delta)^2}\right]$$

A. 6 Interaction between an infinite plate and a solid sphere

Remember that the interaction between an infinite plate of thickness δ and an atom separated by a distance X is:

$$f_{atom}^{\inf\ plate} = \frac{n.\pi.\lambda}{2}\left[\frac{1}{X^4} - \frac{1}{(X+\delta)^4}\right]$$

Therefore, the interaction between any infinitely flat surface composed of such atoms and the same thick plate separated by a distance X is:

$$f_{flat\ surf}^{inf\ \ plate} = \frac{A.s.n.\pi.\lambda}{2}\left[\frac{1}{X^4} - \frac{1}{(X+\delta)^4}\right]$$

Where s is defined as a number concentration of atom per unit of area, and A is the area of the infinitely flat surface. If the flat surface is circular of radius r then the expression is

$$f_{flat\ disc}^{inf\ \ plate} = \frac{r^2.s.n.\pi^2.\lambda}{2}\left[\frac{1}{X^4} - \frac{1}{(X+\delta)^4}\right]$$

Now, a sphere can be thought as a parallel assembly of flat circular surface whose radius r is defined as $r^2=a^2+x^2$, where a is the radius of the resulting sphere and x is the distance of the centre of the sphere from the circular surface. Therefore in order to derive the interaction force between a sphere and an infinite flat plate of thickness δ, let us sum the contribution of each circular surface that compose a sphere of radius a whose centre is at a distance X from the infinite thick surface.

$$\begin{aligned}
f_{sphere}^{plate} &= \frac{nsl\lambda\pi^2}{2}\int_{-a}^{a}\left[\frac{1}{(X+x)^4} - \frac{1}{(X+x+\delta)^4}\right]h^2dx \\
&= \frac{nsl\lambda\pi^2}{2}\int_{-a}^{a}\left[\frac{1}{(X+x)^4} - \frac{1}{(X+x+\delta)^4}\right](a^2-x^2)dx \\
&= \frac{nsl\lambda\pi^2}{2}\frac{-a^2}{3}\left[\frac{1}{(X+x)^3} - \frac{1}{(X+x+\delta)^3}\right]_{-a}^{a} - \\
&\qquad \frac{nsl\lambda\pi^2}{2}\int_{-a}^{a}\left[\frac{x^2}{(X+x)^4} - \frac{x^2}{(X+x+\delta)^4}\right]dx
\end{aligned}$$

Before going further, let us decompose the polynomial fraction from the last integral as:

$$\frac{x^2}{(X+x)^4} = \frac{1}{(X+x)^2} - \frac{2X}{(X+x)^3} + \frac{X^2}{(X+x)^4}$$

So that

$$\begin{aligned}
&\int_{-a}^{a}\frac{x^2}{(X+x)^4} - \frac{x^2}{(X+x+\delta)^4}dx \\
&= \int_{-a}^{a}\frac{1}{(X+x)^2} - \frac{2X}{(X+x)^3} + \frac{X^2}{(X+x)^4} - \frac{1}{(X+\delta+x)^2} + \frac{2(X+\delta)}{(X+\delta+x)^3} - \frac{(X+\delta)^2}{(X+\delta+x)^4}dx \\
&= \left[\frac{-1}{X+x} + \frac{X}{(X+x)^2} - \frac{X^2}{3(X+x)^3} + \frac{1}{X+\delta+x} - \frac{(X+\delta)}{(X+\delta+x)^2} + \frac{(X+\delta)^2}{3(X+\delta+x)^3}\right]_{-a}^{a}
\end{aligned}$$

Then all together,

$$\frac{2f_{sphere}^{plate}}{nsl\lambda\pi^2} =$$

$$\frac{-a^2}{3}\left[\frac{1}{(X+x)^3}-\frac{1}{(X+x+\delta)^3}\right]_{-a}^{a} -$$

$$\left[\frac{-1}{X+x}+\frac{X}{(X+x)^2}-\frac{X^2}{3(X+x)^3}+\frac{1}{X+\delta+x}-\frac{(X+\delta)}{(X+\delta+x)^2}+\frac{(X+\delta)^2}{3(X+\delta+x)^3}\right]_{-a}^{a}$$

$$=-\left[\frac{-1}{X+x}+\frac{X}{(X+x)^2}-\frac{X^2-a^2}{3(X+x)^3}+\frac{1}{X+\delta+x}-\frac{(X+\delta)}{(X+\delta+x)^2}+\frac{(X+\delta)^2-a^2}{3(X+\delta+x)^3}\right]_{-a}^{a}$$

$$=-\frac{2a}{X^2-a^2}+\frac{4aX^2}{(X^2-a^2)^2}-\frac{2a(3X^2+a^2)}{3(X^2-a^2)^2}+\frac{2a}{(X+\delta)^2-a^2}-$$

$$\frac{4a(X+\delta)^2}{((X+\delta)^2-a^2)^2}+\frac{2a(3(X+\delta)^2+a^2)}{3((X+\delta)^2-a^2)^2}$$

$$=-\frac{2a}{X^2-a^2}-\frac{2a(a^2-3X^2)}{3(X^2-a^2)^2}+\frac{2a}{(X+\delta)^2-a^2}+\frac{2a(a^2-3(X+\delta)^2)}{3((X+\delta)^2-a^2)^2}$$

$$=-\frac{6a(X^2-a^2)+2a(a^2-3X^2)}{3(X^2-a^2)^2}+\frac{6a((X+\delta)^2-a^2)+2a(a^2-3(X+\delta)^2)}{3((X+\delta)^2-a^2)^2}$$

$$=\frac{4a^3}{3(X^2-a^2)^2}-\frac{4a^3}{3((X+\delta)^2-a^2)^2}$$

So in the end:

$$f_{sphere}^{plate}=\frac{nsl\lambda\pi^2}{2}\left[\frac{4a^3}{3(X^2-a^2)^2}-\frac{4a^3}{3((X+\delta)^2-a^2)^2}\right]$$

Or again since $n=s.l$

$$f_{sphere}^{\inf\ plate}=\frac{2.n^2.\pi^2.\lambda.a^3}{3}\left[\frac{1}{\left(X^2-a^2\right)^2}-\frac{1}{\left((X+\delta)^2-a^2\right)^2}\right]$$

A. 7 Interaction between a sphere and an atom: one of many ways

Now a sphere can be thought as a continuous succession of parallel circular surfaces (e.g. one can very well derive the volume of a sphere from the area of circle).

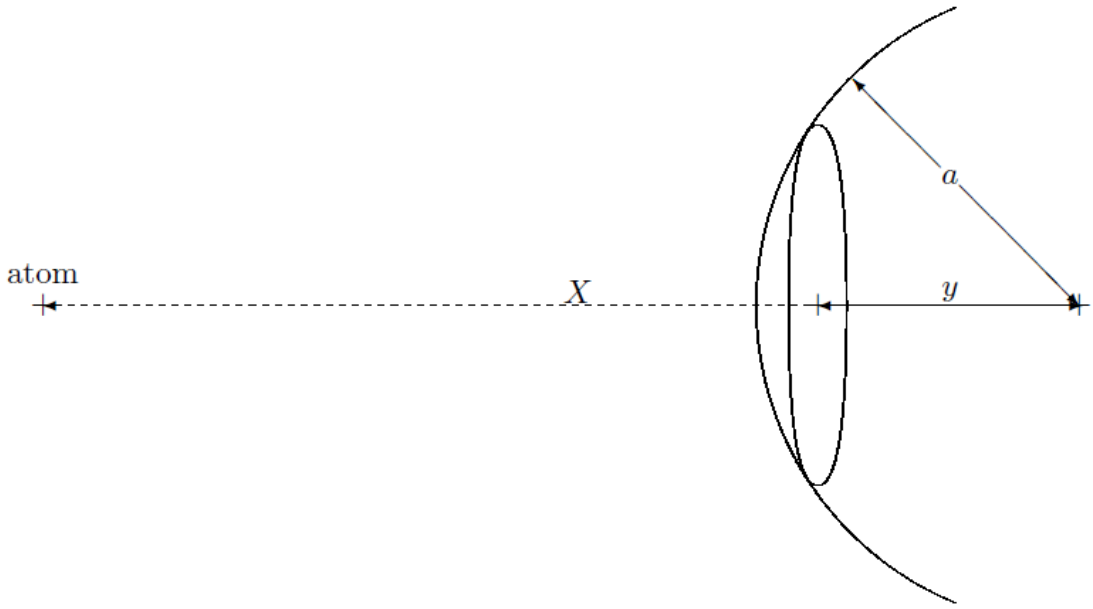

Therefore all we have to do is sum the force contribution of each infinitesimal circular surfaces that correspond to a cut of a sphere of radius a, and whose centre is at a distance X from the atom. That gives:

$$f_{atom}^{spher} = 6.s.l.\pi.\lambda.\int_{y=-a}^{y=a} \frac{1}{(X+y)^6} - \frac{X+y}{\left(R^2+(X+y)^2\right)^3}.dy$$

Where y is the distance of the infinitesimal circular surface from the centre of the sphere and h its radius, then $a^2=h^2+y^2$.

$$f_{atom}^{sphere} = 2sl\lambda\pi \int_{y=-a}^{y=a} \frac{1}{(X+y)^5} - \frac{X+y}{(a^2-y^2+(X+y)^2)^3}dy = 2sl\lambda\pi \int_{y=-a}^{y=a} \frac{1}{(X+y)^5} - \frac{X+y}{(a^2+X^2+2Xy)^3}dy$$
$$= \frac{sl\lambda\pi}{2}\left[\frac{-1}{(X+y)^4} + \frac{1}{(a^2+X^2+2Xy)^2}\right]_{y=-a}^{y=a} - 2sl\lambda\pi \int_{y=-a}^{y=a} \frac{y}{(a^2+X^2+2Xy)^3}dy$$

Before going further, let us decompose the polynomial fraction in the last integral.

$$\frac{y}{(a^2+X^2+2Xy)^3} = \frac{1}{2X}\left[\frac{1}{(a^2+X^2+2Xy)^2} - \frac{a^2+X^2}{(a^2+X^2+2Xy)^3}\right]$$

hence

$$\begin{aligned} f_{atom}^{sphere} &= \frac{sl\lambda\pi}{2}\left[\frac{-1}{(X+y)^4} + \frac{1}{(a^2+X^2+2Xy)^2} + \frac{2}{X}\frac{1}{2X(a^2+X^2+2Xy)} - \frac{2}{X}\frac{a^2+X^2}{4X(a^2+X^2+2Xy)^2}\right]_{y=-a}^{y=a} \\ &= \frac{sl\lambda\pi}{2}\left[\frac{-1}{(X+y)^4} + \frac{1}{X^2(a^2+X^2+2Xy)} + \frac{2X^2}{2X^2(a^2+X^2+2Xy)^2} - \frac{a^2+X^2}{2X^2(a^2+X^2+2Xy)^2}\right]_{y=-a}^{y=a} \\ &= \frac{sl\lambda\pi}{2}\left[\frac{-1}{(X+y)^4} + \frac{1}{X^2(a^2+X^2+2Xy)} + \frac{X^2-a^2}{2X^2(a^2+X^2+2Xy)^2}\right]_{y=-a}^{y=a} \end{aligned}$$

$$\begin{aligned} f_{atom}^{sphere} &= \frac{sl\lambda\pi}{2}\left[\frac{1}{(X-a)^4} - \frac{1}{(X+a)^4} + \frac{1}{X^2(X+a)^2} - \frac{1}{X^2(X-a)^2} + \frac{X^2-a^2}{2X^2(X+a)^4} - \frac{X^2-a^2}{2X^2(X-a)^4}\right] \\ &= \frac{sl\lambda\pi}{2}\left[\frac{8Xa(X^2+a^2)}{(X^2-a^2)^4} + \frac{-4aX}{X^2(X^2-a^2)^2} + \frac{-8aX(X^2-a^2)(X^2+a^2)}{2X^2(X^2-a^2)^4}\right] \\ &= \frac{sl\lambda\pi}{2}\left[\frac{8X^3a(a^2+X^2) - 4aX(X^2-a^2)^2 - 4aX(X^2-a^2)(a^2+X^2)}{X^2(X^2-a^2)^4}\right] \\ &= \frac{sl\lambda\pi}{2}\left[\frac{16a^3X^3}{X^2(X^2-a^2)^4}\right] \\ &= sl\lambda\pi\frac{8a^3X}{(X^2-a^2)^4} \end{aligned}$$

A. 8 Interaction between a sphere and a thick disc

In order to derive the expression of the force between a sphere and a disc of thickness δ, let us first consider the interaction between a sphere and a circular surface.

As usual, the expression for the infinitesimal surface is *dS=2.pi hdh* therefore the expression for the force of the sphere on that elementary surface is:

$$df = s.f_{atom}^{sphere}dS.\cos\theta = s.8.n.\lambda.2.\pi^2\frac{ra^3h}{\left(r^2-a^2\right)^4}\frac{X}{r}dh = s.8.n.\lambda.a^3.\pi^2.X\frac{2h}{\left(h^2+X^2-a^2\right)^4}dh$$

So the total force induced by the sphere on the flat surface is:

$$f_{circ\ surf}^{sphere} = s.8.n.\lambda.a^3.\pi^2.X\int_{h=0}^{b}\frac{2h}{\left(h^2+X^2-a^2\right)^4}dh$$

$$f_{circ\ surf}^{sphere} = s.\frac{8}{3}n.\lambda.a^3.\pi^2.X.\left[\frac{1}{\left(X^2-a^2\right)^3} - \frac{1}{\left(b^2+X^2-a^2\right)^3}\right]$$

In order to derive the expression for total interaction of a disc of thickness δ and a sphere it only remains to integrate the above equation with respect to X over a distance δ.

$$f_{disc}^{sphere} = \frac{8}{3} n^2 .\lambda .a^3 .\pi^2 .\int_X^{X+\delta} \frac{X}{\left(X^2 - a^2\right)^3} - \frac{X}{\left(b^2 + X^2 - a^2\right)^3} dX$$

$$f_{disc}^{sphere} = -\frac{2}{3} n^2 .\lambda .a^3 .\pi^2 .\left[\frac{1}{\left(X^2 - a^2\right)^2} - \frac{1}{\left(b^2 + X^2 - a^2\right)^2} \right]_X^{X+\delta}$$

$$f_{disc}^{sphere} = \frac{2}{3} n^2 .\lambda .a^3 .\pi^2 .\left(\frac{1}{\left(X^2 - a^2\right)^2} - \frac{1}{\left((X+\delta)^2 - a^2\right)^2} - \frac{1}{\left(b^2 + X^2 - a^2\right)^2} + \frac{1}{\left(b^2 + (X+\delta)^2 - a^2\right)^2} \right)$$

The expression of the interaction between a sphere and a plate is just the limit of the above expression when b is big, therefore:

$$f_{plate}^{sphere} = \frac{2}{3} n^2 .\lambda .a^3 .\pi^2 .\left(\frac{1}{\left(X^2 - a^2\right)^2} - \frac{1}{\left((X+\delta)^2 - a^2\right)^2} \right)$$

A. 9 Interaction between spherical colloidal particles

Let us consider two spherical particles of respective radius a and b whose centres are separated by a distance R. The interaction between them is the sum of all the forces between the infinitesimal circular surfaces constituting one sphere with the entire opposite sphere.

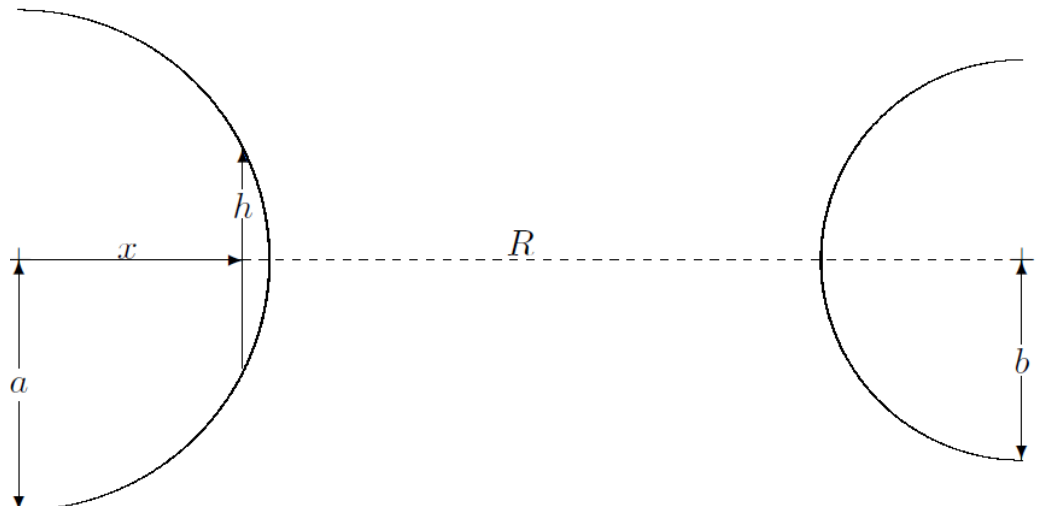

The interaction between two spherical particles can be expressed as:

$$f_{spheres} = \int_{x=-a}^{a} f_{circ\ surf}^{sphere}(x).l.dx = ls.\frac{8}{3}n.\lambda.b^3.\pi^2.\int_{x=-a}^{a}\frac{R+x}{\left((R+x)^2-b^2\right)^3}-\frac{R+x}{\left(h^2+(R+x)^2-b^2\right)^3}.dx$$

Where $a^2=x^2+h^2$, therefore:

$$\begin{aligned}
\frac{f_{spheres}}{\frac{8}{3}n^2\lambda\pi^2b^3} &= \int_{x=-a}^{a}\left[\frac{R+x}{((R+x)^2-b^2)^3}-\frac{R+x}{(a^2+R^2-b^2+2Rx)^3}\right]dx \\
&= -\frac{1}{4}\left[\frac{1}{((R+x)^2-b^2)^2}\right]_{x=-a}^{x=a}+\frac{1}{4}\left[\frac{1}{(a^2+R^2-b^2+2Rx)^2}\right]_{x=-a}^{x=a} \\
&\qquad -\frac{1}{2R}\int_{-a}^{a}\frac{1}{(a^2+R^2-b^2+2Rx)^2}-\frac{a^2+R^2-b^2}{(a^2+R^2-b^2+2Rx)^3}dx \\
&= \frac{1}{4R^2}\left[\frac{1}{a^2+R^2-b^2+2Rx}-\frac{a^2+R^2-b^2}{2(a^2+R^2-b^2+2Rx)^2}\right]_{-a}^{a} \\
&= \frac{1}{8R^2}\frac{32R^3a^3}{\left((R+a)^2-b^2\right)^2\left((R-a)^2-b^2\right)^2}
\end{aligned}$$

So in the end:

$$f_{spheres} = \frac{32}{3}n^2.\lambda.R.\pi^2.\frac{b^3a^3}{\left(\left((R+a)^2-b^2\right).\left((R-a)^2-b^2\right)\right)^2}$$

Or again:

$$f_{spheres} = \frac{32}{3}n^2.\lambda.R.\pi^2.\frac{b^3a^3}{\left((b+a-R).(R-b+a).(b+a+R).(a-R-b)\right)^2}$$

Which is symmetric in a and b as expected.

For two spheres of same radius, the expression simplifies as:

$$f_{spheres} = \frac{32}{3}n^2.\lambda.\pi^2.\frac{a^6}{R^3\left((2a-R).(2a+R)\right)^2}$$

Introducing the shortest distance between the spheres d, $R=2.a+d$ and $H=\pi^2.\lambda.n^2$ the Hamaker coefficient, the expression becomes:

$$f_{spheres}^{equal} = H.\frac{32}{3}.\frac{a^6}{d^2.(2a+d)^3(4a+d)^2}$$

Now assuming $d<<a$, the expression reduces to

$$f_{spheres}^{close} = \frac{H.a}{12.d^2}$$

That corresponds to an attractive potential whose expression is:

$$E_{spheres}^{close} = -\frac{H.a}{12.d}$$

APPENDIX B: Publications

Chaumeil, F. and M. Crapper, *DEM simulations of initial deposition of colloidal particles around non-woven membrane spacers.* Journal of Membrane Science. **442**(2013): p. 254-263. http://www.sciencedirect.com/science/article/pii/S0376738813003116 [145]

Journal of Membrane Science 442 (2013) 254–263

Contents lists available at SciVerse ScienceDirect

Journal of Membrane Science

journal homepage: www.elsevier.com/locate/memsci

DEM simulations of initial deposition of colloidal particles around non-woven membrane spacers

Florian Chaumeil, Martin Crapper*

School of Engineering, The University of Edinburgh, Edinburgh EH9 3JL, United Kingdom

ARTICLE INFO

Article history:
Received 15 February 2013
Received in revised form
12 April 2013
Accepted 13 April 2013
Available online 25 April 2013

Keywords:
Discrete Element Method
Fouling
Spacers
Deposition
Colloid
Simulation

ABSTRACT

The modelling of the initial deposition on membrane spacers of colloidal size particles immersed in a liquid is investigated using the Discrete Element Method (DEM) coupled to Computational Fluid Dynamics (CFD). The ability of this method to model surface interactions allows the modelling of aggregation and deposition at the particle scale. The numerical model adopts a mechanistic approach to represent the forces involved in colloidal suspension by including near wall drag retardation, surface interaction and Brownian forces. The model is implemented using commercially available software, so that results can be replicated in a standard and user-friendly framework. The effect of different spacer orientation with respect to feed direction is examined and results show that deposition of particles is increased around the spacer joints when feed orientation bisects the spacers' angle; when one of the spacer filaments is aligned with the feed inflow deposition occurs exclusively and uniformly on it. Simulation results demonstrate the validity of the method to describe the small-scale behaviour of micro-particles around spacers. The incipient fouling of particles in this size range is analogous to incipient bio-fouling of membrane spacers.

1. Introduction

Spiral-wound modules (SWM) are used in many types of filtration processes like desalination, water purification and food processing since their spiral configuration offers high specific membrane area. However, they are restricted in their performance by concentration polarisation and fouling, like any membrane process. This fouling results in increased capital and operating costs, for example in the installation of redundant modules, the replacement of used modules and in filtration efficiency drop. The spiral configuration also requires membrane spacers to keep each layer of the spiral separated and provide sufficient room for the water inflow.

Spacers play an important role in membrane systems [1]. They support and separate membrane sheets, or layers, in SWMs, which is why they are also found in electro-dialysis stacks. They can have beneficial effects on mass transfer, homogenizing and mixing behaviour, hence reducing fouling [2]. Spacers are usually composed of a net of inter-locking filaments as shown in Fig. 1 or more rarely of extrusions of membrane surface [3]. Feed spacers can be designed for enhancing re-suspension of the rejected species to the bulk of the feed flow and thus lowering concentration polarisation in spiral wound membrane modules. However, one adverse effect is that they induce pressure drop along the membrane module; this can lead to higher power consumption as illustrated by Da Costa et al. [4], who showed that hydrodynamic angles (α, β), Fig. 1, are critical parameters in designing spacer-filled membrane channels. Pressure drop is dominated by the drag force on spacer strands and Darcy–Weisbach friction-like kinetic losses due to changes in flow direction [5].

In order to optimize the trade-off between enhanced mass transfer and increased cross-flow power consumption, CFD modelling [6–15] has been used extensively. However, computational techniques have rarely been used to investigate another issue of SWM, bio-fouling, which arises from their extensive use in municipal water treatment plants and in industrial food processing. Spacer bio-fouling has been observed in industrial SWM autopsies, which are laborious. It can also be studied using direct observation through membrane (DOTM), requiring expensive optical instrumentation. For this reason, numerical modelling can provide precious insight.

Bio-fouling occurs via the formation of a bio-film that is initiated by the adhesion of primary colonizing organisms like microbes and bacteria, whose adhesion is a controlled at first by long-range forces such as attractive Van-Der-Waals forces and repulsive electrostatic forces [16]. They form micro-colonies composed initially of organisms of the same species. They later combine and form other types of bio-film structures composed of different microbial strains including algae, fungi and protozoa.

* Corresponding author. Tel./fax: +44 131 650 5727.
E-mail address: Martin.Crapper@ed.ac.uk (M. Crapper).

0376-7388/$ - see front matter © 2013 Elsevier B.V. All rights reserved.
http://dx.doi.org/10.1016/j.memsci.2013.04.031

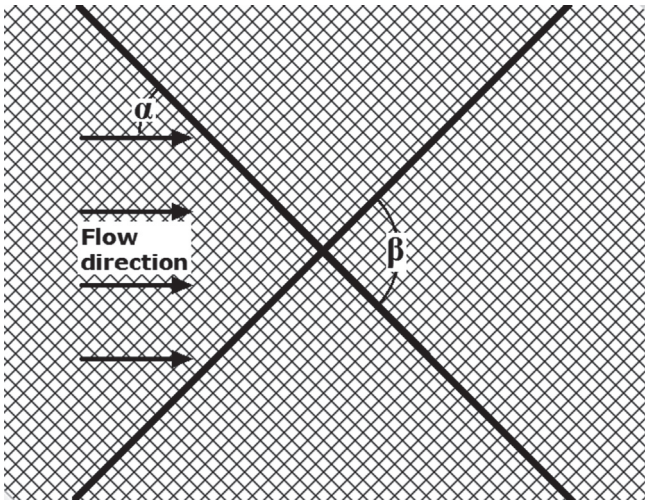

Fig. 1. Sketch of net-type spacer's structure.

These find energy and organic material (nutrients) for growth from dissolved feed-water organic material [17].

The critical flux of a membrane system is defined as the flux at which the relation between the trans-membrane pressure (TMP) and flux is no longer linear, due to matter deposition. Neal et al. [18] used the DOTM technique to determine the effect of spacer orientation on this critical flux. They found that spacers significantly increase critical flux for a flow laden with 6.4 μm latex beads. The degree of enhancement depended on spacer orientation, which means that spacer orientation has an effect on how particle deposit on the membrane. A similar observation technique was used by Vrouwenvelder et al. [19] in order to observe the onset of bio-film formation on the spacer itself and showed that deposition initiates upstream of the spacer, in front of the filament junctions, and to a lesser extent on the filament body after a long time. These results were later extended using the multi-physics package COMSOL and a cellular automata algorithm to model numerically the fluid dynamics and bio-fouling of feed channels [20]. It was shown that bio-fouling is a problem of initial deposition and bio-film growth and not a deposition effect due to filtration pressure. They confirmed that initial deposition occurs upstream of the spacers, but demonstrated that the biomass volume increase, which reduces filtration efficiency, corresponds to microorganism multiplication occurring mainly downstream of the spacer. Experimental work from Ngene [3] on a structured membrane, which is essentially a membrane with protrusions that play the same hydraulic role as SWM spacers, confirmed that there is initially a predominance of bio-film formation upstream of the structures, with a downstream formation of filamentous bio-film attached to the back of the structure at a later stage. Bio-film formation on micro-obstacles of the structured membrane was observed to be following a mechanism comparable to that on woven spacers [3].

Calculations made by Bacchin et al. [21] suggested that critical flux depends strongly on particle size. For particles over 1 μm, the shear-induced diffusion that lifts particles away from the membrane surface becomes significant and competes with surface charge effects which retain them. A lower amount of fouling is observed with such particles, in comparison to the effects of bio-fouling, where extra-cellular polymeric substance (EPS) adherence and growth also contribute. In addition, for particulate fouling, there is a limited mass of particles which can be deposited on the surface of the structures, after which there is equilibrium between the deposition and detachment of particles from the structure surface. However, the mechanisms of initial particle deposition strongly correlate with observations on primary bio-fouling [22].

It is therefore hypothesised that simulations of particulates as described in this work can predict initial deposition patterns which are applicable both to particulate fouling and to bio-fouling, meaning much can be learned about bio-fouling without the need to model the impact of EPS mediation and growth, which would be computationally expensive.

This work describes a novel and easy method to investigate initial particulate and bio-film deposition corresponding to flowing particles being captured by the membrane. It evaluates the role of aggregation, which is the mechanism by which individual, free-flowing particles or clusters are captured by previously deposited particles or cluster of particles. The later stages of microbial growth and colonisation are considered, as it would require more extensive computational resources. Simulations considered 2 μm diameter size micro-particles (which is about the same size as common microbes such as *Escherichia coli* [23]) around the joints of non-woven net type spacers, these being the most commonly used in SWMs. Simulations will consider low inlet velocity, corresponding to typical laboratory scale setups rather than industrial applications. This is because the effects of turbulence–particle interaction encountered at higher velocities remain an unresolved subject of ongoing research.

Particle scale modelling of aggregation, cluster scouring and particle re-suspension as flocs are simulated using coupled Discrete Element Method (DEM)–Computational Fluid Dynamics (CFD) [24], with the CFD computation being used to determine the flow field and corresponding hydrodynamic forces, which are then used in the DEM calculations to model the motion of individual particles and clusters. The coupled DEM–CFD technique allows the simulation of particle–particle, particle–spacer, particle–membrane and particle–flow interactions. The overarching aim of the study is to demonstrate the usefulness of the DEM–CFD technique for the investigation of particulate fouling, including incipient bio-fouling, of SWM spacers.

2. Definition of spacer geometry

Spacer geometry has been chosen to match the commercial range of spacers NALTEX-51 as this has already been subject to published studies, both experimental [4,8], and computational [8], and has therefore a well defined geometry, with specifications readily available. Many studies [2,10,11,25] use artificial, generalized dimensions in order to evaluate qualitatively spacers' mitigating effect on filtration. However, the present study seeks to evaluate the modelling method against previous results. Therefore, it has been chosen to model commonly cited configurations. There is a wide range of commercial spacers from which to choose, but only a few particle deposition studies that poorly communicate the dimensions of their models. The Naltex series were the best documented ones at the time of this study, although no particle deposition study has been found with their exact geometry. It is however believed that deposition numbers and morphologies follow similar enough trends to be compared. Naltex basic geometry is shown in Fig. 2.

Each product in the range is merely a rotation of the others by various angles, indicated by α and β in the figure. This readily enables the modelling of how the feed flow direction influences particle deposition on the spacer filaments.

The three-dimensional model was built using GAMBIT 2.1® with dimensions provided in Table 1, and the fluid velocity field was computed with FLUENT 12.0® with a 1 mm/s inlet velocity in order for the flow to remain laminar [12]. A particle-tracking model, implemented through the DEM software EDEM 2.3®, was used to simulate the particle deposition under the influence of

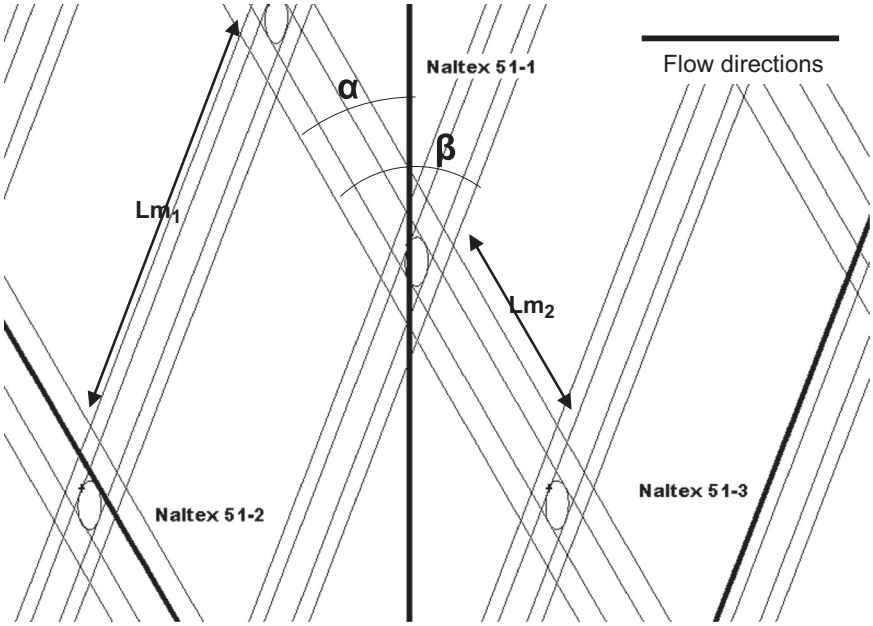

Fig.2. Naltex spacer parameters definition.

Table 1
Geometrical parameters of the Naltex-51 spacers.

Spacers parameters	Value
α	30°
β	51°
R_S (small filament radius)	0.25 mm
R_B (big filament radius)	0.35 mm
Lm_1	5.37 mm
Lm_2	2.89 mm
Filament overlap	0.03 mm

both fluid drag and Van der Waals attraction, as described in the next section.

3. Force model

3.1. Definition of the mechanistic model

Both the shape of the computational domain and the inlet condition (flow rate, inlet velocity distribution) define the flow field inside the SWM tube. The trajectories of immersed particles within the flow field are integrated for different particle sizes, particle concentrations and fluid flow rates, following the method described below.

The Lagrangian method determines the trajectory of each particle under the effect of colloidal and external forces, and the governing equation of particle transport is the stochastic Langevin equation, including particle Brownian motion. Particle trajectory and particle deposition are controlled by the combined influence of colloidal and hydrodynamic interactions, as is described by the force balance equation (1) [26]

$$m\frac{du_p}{dt} = F_D + F_G + F_L + F_{EDL} + F_{LVdW} + F_B, \quad (1)$$

here m is the particle mass and u_p is the particle velocity vector. F_D is the fluid drag, F_G the force due to gravity, F_L the shear lift, F_{EDL} the electrostatic repulsion, F_{LVdW} the van der Waals attraction, and F_B the Brownian forces. Particle rotation is considered in the DEM computation, but its effect on hydraulic interactions are not included in this study, although the DEM technique would allow this in cases where they are thought to be significant.

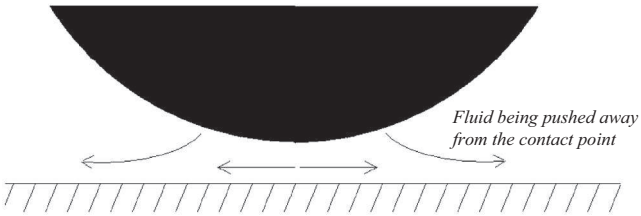

Fig. 3. Fluid behaviour between a wall and an approaching particle.

It is to be noted, however, that DEM is not commonly used to simulate processes involving very small finite particles, like colloids. The following paragraphs describe the models and equations required to model the flow of a dilute colloidal suspension.

3.2. Near the wall hydraulic retardation

In the vicinity of a wall boundary, the displacement of the fluid between the particle and the wall becomes increasingly difficult because of the fluid between the particle and the wall needing to be accelerated (see Fig. 3).

This causes the particle to bear an additional hydrodynamic drag over the Stokes drag on the particle. Hence, near a channel wall, particle motion is retarded due to the presence of the wall. Similarly, the presence of neighbouring particles causes the mutual retardation of the particles.

In order to consider this phenomenon we express the 3D-vector of the particle velocity in the wall's local reference frame as defined by the vector normal to the surface and two vectors normal to each other in the plane tangential to the surface. Any motion of the particle relative to the wall can therefore be expressed as the sum of a velocity vector orthogonal to the wall with a velocity vector parallel to the wall.

Then, for a particle impinging orthogonally on a rigid wall, the hydrodynamic force applied to a sphere with radius, a, orthogonally approaching a plane wall can be described by the modified

Stokes' equation [26]:

$$F_{D\perp} = F_1 + F_2 = -6\pi\mu \cdot aV \cdot \lambda_\perp + 6\pi\mu \cdot aU \cdot f_2 \quad (2)$$

In Eq. (2), the drag is composed of the sum of term, F_1, corresponding to the case where the particle with velocity V normal to the wall moves in a zero velocity field and therefore experiences a drag in the opposite direction of its velocity, and term F_2 corresponding to the case of a stationary particle within a liquid flow field with velocity U at the location of the centre of the particle. The particle therefore experiences a drag in the same direction of the fluid velocity.

Eq. (2) deviates from Stokes' law by the introduction of λ_t and f_2, correction factors which take into account the presence of a nearby wall. They are functions of the inter-surface separation distance, assuming a non-slip boundary condition applies to both the particle and solid surfaces. These factors tend to unity at large distances from the wall.

For the situation in which the sphere radius is small compared to the separation distance, Lorentz [27] found that the resistance of the particle is greater than would be predicted by Stokes' law by a factor $\lambda_\perp$. Independently of the ratio of radius to distance, Brenner [28] calculated the general analytical expression for $\lambda_\perp$, the first two terms of the Taylor expansion of $\lambda_\perp$ being the Lorentz formula. The exact and approximate expressions for resistance coefficients of a motionless colloidal sphere approaching a solid surface were derived by Nguyen and Evans [29]. For greater computational efficiency, analytical retardation functions are approximated by simpler expressions. For a solid particle approaching a much larger solid surface with non-slip boundary conditions at local supporting flow Reynolds numbers lower than 50, the approximate solution is [29]:

$$f_2 = \frac{2.022 + h/a}{0.626 + h/a} \text{ and}$$

$$\lambda_\perp = [1 + (a/h)^p]^{1/p} \text{ with } p = 0.89 \quad (3)$$

h and a are as shown in Fig. 4.

For the translational and rotational motion of a sphere parallel to a rigid wall, Goldman et al. [30,31] developed asymptotic solutions for the near-wall hydrodynamic forces when a particle flows past an obstacle:

$$\frac{1}{\mu}\overline{\nabla} p = \overline{\nabla}^2 v, \quad \overline{\nabla}.\overline{v} = 0 \quad (4)$$

for a non-rotating sphere near a plane in a quiescent fluid, they computed the asymptotic drag function:

$$F_{D\|}^{t*} \approx \frac{8}{15}\ln(\delta/a) - 0.9588 \quad (5)$$

where δ is as shown in Fig. 4. Considering the linearity of Stokes' equations [31], they then superimposed the force induced by a linear shearing flow past an immobilized sphere near a rigid wall:

$$F_{D\|}^{s} = 6\pi\mu aSh\left(1 + \frac{9}{16}\frac{a}{h}\right) \text{ with the fluid velocity } U_f = Sh \quad (6)$$

Finally the drag force acting on a sphere flowing closely along a wall is computed as the sum of all contributions:

$$F_{D\|} = 6\pi\mu a\left(UF_{D\|}^{t*} + a\Omega F_{D\|}^{r*} + Sh\left(1 + \frac{9}{16}\frac{a}{h}\right)\right) \quad (7)$$

In the current work, the size of the particle (of radius 10 μm) is very small compared with the size of the membrane spacer filaments (of mean radius 0.3 mm), so the assumption that the filament represents a plane wall is reasonable and the above models can be applied. Where the spacers join, or join the membrane surface, retardation from all boundaries close to the particle are considered. The curvature of the walls remains insignificant relative to the particle size.

Retardation due to other particles has not been included. This is a complex issue, subject to ongoing work [32], and the number of particle collisions was sufficiently small to render it irrelevant in this study.

3.3. Brownian motion and diffusion

For sub-micron sized particles, Brownian motion must be considered and the local Stokes drag force is corrected by a Cunningham factor [33]. The drag force expression is then given by:

$$F_D^{sub} = F_D^{ret}/C_C \text{ where } C_C = 1 + \frac{2\lambda}{d}(1.2571 + 0.4e^{-0.55d/\lambda}) \quad (8)$$

F_D^{ret} is the usual drag force (including the hydraulic retardation) and λ is the molecular mean free path of the surrounding medium [26,34].

$$\lambda\frac{\sqrt{mk_BT}}{\xi} \text{ [26] in a fluid and } \lambda = \frac{\mu}{\sqrt{2P\rho/\pi}} \text{ in a gas [34]} \quad (9)$$

ξ is the drag or friction coefficient ($\xi = 6\pi\cdot\mu\cdot r_P$), k_B is the Boltzmann constant and T is the temperature in Kelvin. Following the method used by Ounis et al. [33], the Brownian force components are independent white noise processes. At every time step, three independent Gaussian random numbers (G_i) of zero mean and unit variances are generated and are related to the Brownian force (F_B) in the momentum conservation equation (Eq. (1)), by

$$\overrightarrow{F_B} = \sum_{i=1}^{3} N_i \overrightarrow{e_i} \quad (10)$$

N_i is the amplitude of the ith component of the Brownian force expressed as:

$$N_i = G_i\sqrt{\frac{\pi S}{\Delta t}} \text{ where } S = \frac{2k_BTf}{\pi};\ f = \frac{6\pi\mu r_p}{C_c} \text{ so } N_i = G_i\sqrt{\frac{6\pi\mu r_p \cdot 2k_BT}{\Delta t.C_C}} \quad (11)$$

3.4. DLVO forces

The interaction between two charged solute particles is generally expressed by the DLVO potential, which comprises an attractive Lifshitz–Van der Waals (LVdW) and a repulsive electrostatic double layer (EDL) interaction [35].

The repulsive role of the electrical double layer and its correlation with particle roughness is still under investigation [26,36]. This work therefore focuses on deposition under favourable conditions, with only attractive Van-Der-Waals interaction. Between two

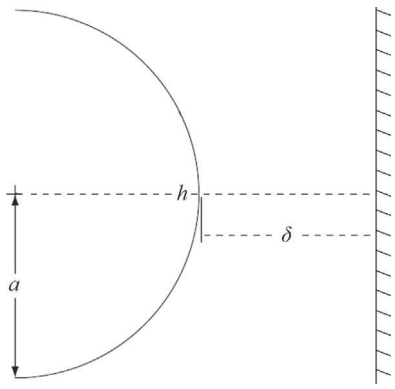

Fig. 4. Fluid behaviour between a wall and an approaching particle.

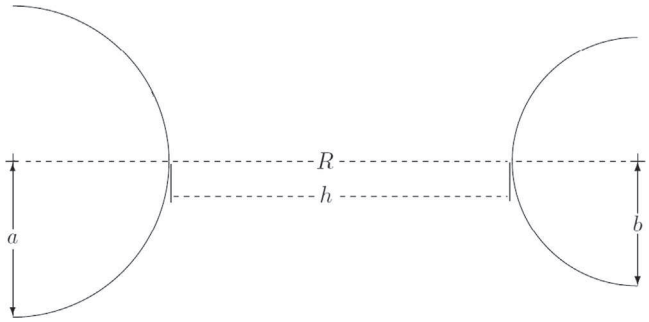

Fig. 5. Interaction between two spherical particles.

spherical surfaces immersed in a fluid medium, this expressed as:

$$F_{LVDW} = \frac{32}{3} n^2 \lambda \pi^2 R \frac{b^3 a^3}{(((R+a)^2 - b^2)((R-a)^2 - b^2))^2} \quad (12)$$

(See Fig. 5 for definitions of symbols.) for two spheres of same radius and positioned very close to each other ($h \ll a$):

$$F_{LVDW} = \frac{Ha}{6h^2} \text{ with } R = 2a + h$$

The effects of magnetic retardation also need to be included as a factor in the Van der Waals force expression [37]:

$$f_m = \frac{\lambda(\lambda + 22.24h)}{(\lambda + 11.12h)^2} \quad (13)$$

the term λ is the characteristic wavelength of interaction, which can be taken to be 10^{-7}.

The VdW interaction between a particle and a solid wall is derived from Eq. (12) when $b \gg a$, in which case

$$F_{LVDW} = \frac{32Ha^3}{3(h \cdot (2 \cdot a + h))^2} \quad (14)$$

3.5. Summary of model forces

Forces common to all the simulations in this work are summarized in Table 2.

The simulation parameters common to all tested configurations are presented in Table 3.

4. Model implementation

4.1. CFD method description

Due to the complexity of the spacer-filled channel to be modelled, an unstructured mesh was used for the CFD calculations (Fig. 6).

The commercial software FLUENT 12.1 was used to solve the steady-state Navier–Stokes equations under laminar flow

Table 2
Summary of forces to be considered in the momentum conservation equation.

Force	Expression	Ref
Van der Waals	$F_{lvdw} = \frac{32}{3} n^2 \lambda \pi^2 R \frac{b^3 a^3}{(((R+a)^2 - b^2)((R-a)^2 - b^2))^2}$	[26,35]
Drag	$F_{D\perp} = -6\pi\mu R V . \lambda_\perp + 6\pi\mu R U . f_2$ $F_{D\parallel} = 6\pi\mu a \left(U F^{t*}_{D//} + Sh \left(1 + \frac{9}{16} \frac{a}{h} \right) \right)$	[30,31]
Brownian	$\overrightarrow{F_B} = \sum_{i=1}^{3} N_i \overrightarrow{e_i}$ with $N_i = G_i \sqrt{\frac{\pi S}{\Delta t}}$	[33]
Shear lift	$F_{SL} = 0.25 \cdot C \cdot D_p^2 \cdot \rho_f (u_f - u_p) \sqrt{\nu \frac{\partial u_f}{\partial n}}$	[38]

Table 3
Simulation parameters.

Universal constant	Value
Boltzmann constant k_B	1.381e−23 J/K
Temperature T	300 K
characteristic wave length λ	1e−7 m
Hamaker constant $H = n^2 \lambda \pi^2$	1.5e−20 J
Water dynamic viscosity μ	1e−3 kg s/m
Density of particle ρ_P	1e3 kg/m^3

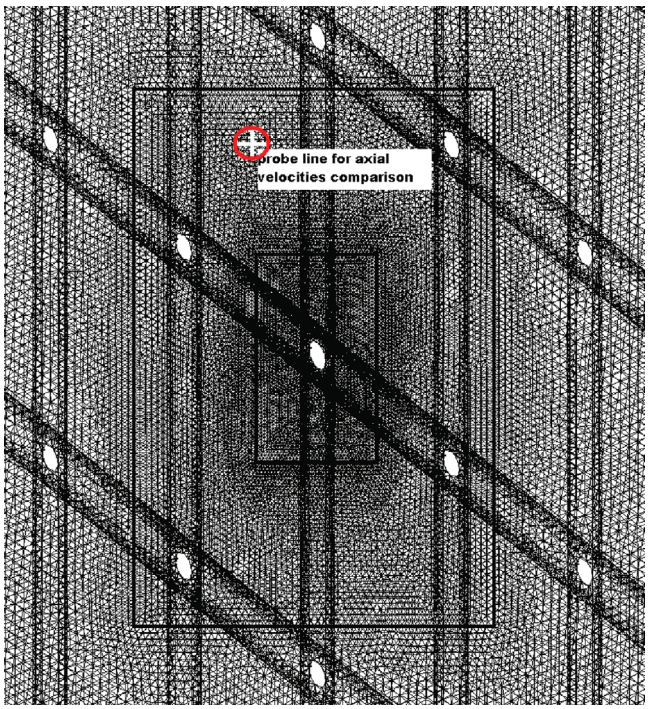

Fig. 6. Unstructured mesh around spacer filaments joint.

hydrodynamics, using the SIMPLE algorithm [39]. The mesh was created with tetrahedral elements to ensure residual convergence and stability as well as independence of the solution.

Boundary conditions for the model include no-slip boundaries at the spacer-wall surface and a no-slip condition at the membrane surface; permeate flow is considered slow enough to be neglected [40], and a predefined inlet velocity of 1 mm/s was used at the cell entry.

Velocity magnitudes have been extracted from CFD results along a probe-line perpendicular to the viewing plane of Fig. 6 at the location highlighted by the circle at the centre of the spacer cells (Fig. 6) in a similar manner to Karode and Kumar [8] (Fig. 7). Velocity profiles are close to parabolic, which is to be expected for a laminar flow between two plates. CFD results are also consistent with Wardeh and Morvan work [12], although their test feed channel geometry was slightly wider.

4.2. DEM implementation description

DEM Mechanistic principles as described by Cundall [41] and Van der Hoef [24] are implemented via the EDEM 2.3 software, which allows the consideration of particle collisions through elastic Hertzian contact models, and enables coupling with CFD data. The coupling method used in this work is called one-way

DEM–CFD coupling. It only allows the fluid to influence particles while particle loading has no influence on the fluid. This applies to low level of particle concentration as in this work. API programming was used to add required force models which are not standard to the software.

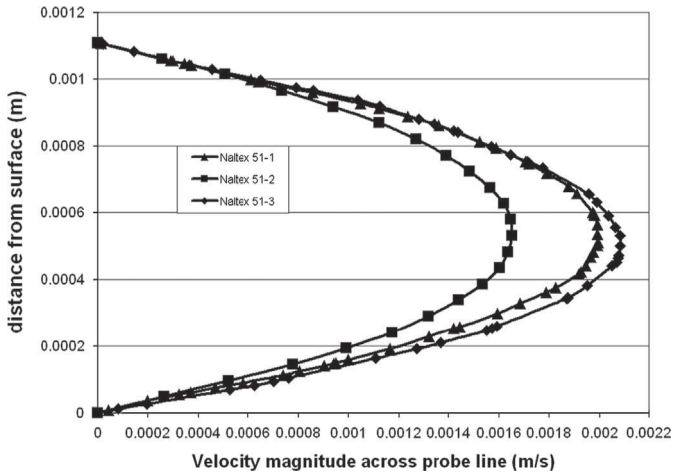

Fig. 7. Axial fluid velocities comparison.

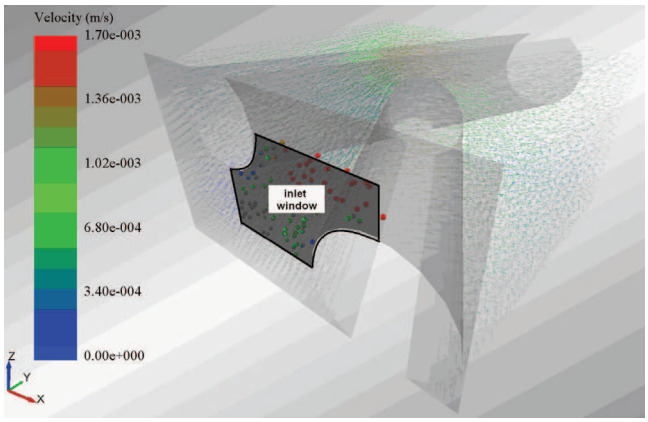

Fig. 8. Particle inlet window.

For each spacer configuration, particles were created within an inlet control window (Fig. 8), which surrounds the spacer filaments. Following the limiting trajectory principle [42], particles injected further way from the wall would not contribute to the deposition process.

Particles were randomly created one by one following a uniform law over the control window surface, meaning that at each time step, the probability of particle creation was equal and uniform at each point of the inlet window. The particle creation

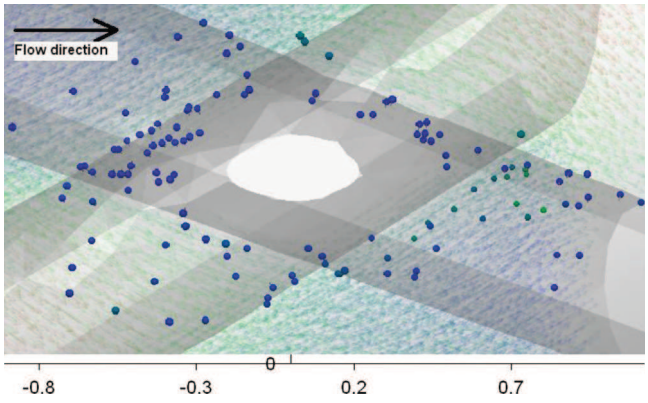

Fig. 10. Deposition around Naltex 51-1 spacer joint (with distance scale in mm).

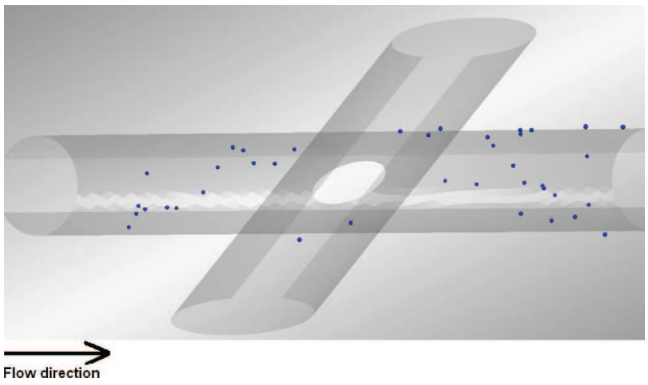

Fig. 11. Deposition around Naltex 51-2 spacer joint.

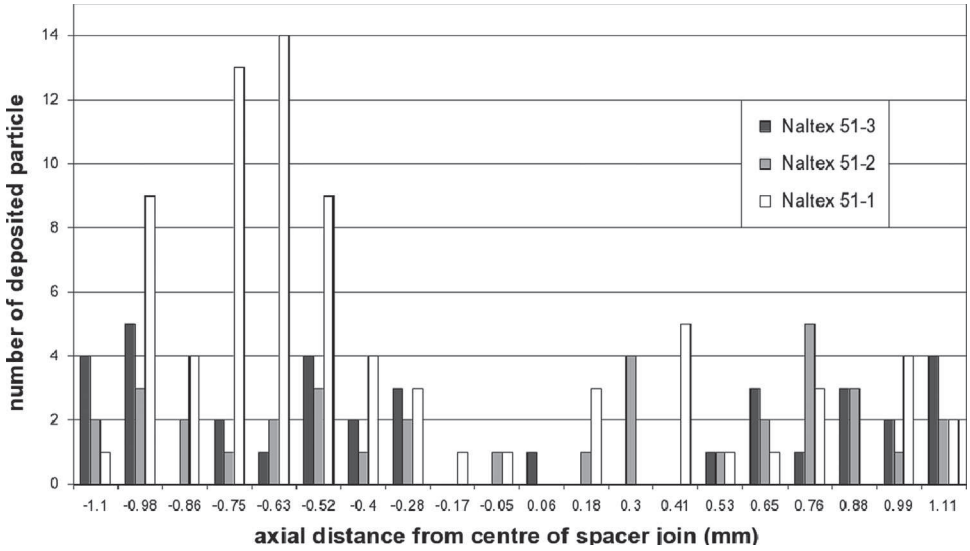

Fig. 9. Number of deposited particles for each configuration.

rate was set to 10E5particles/s in order to allow a high enough concentration of particles in the computational volume and favour particle-to-particle collisions and cluster formation.

For each single simulation, the computation was left running until the suspended particles escaped entirely. On a 3 GHz Core2 Quad CPU desktop computer with 3GB RAM, it took 6.5 days to run each of the three simulations. Once each simulation finished, only deposited particles remained in the computational domain, which provided a way to quantify the number of deposited particles for each configuration.

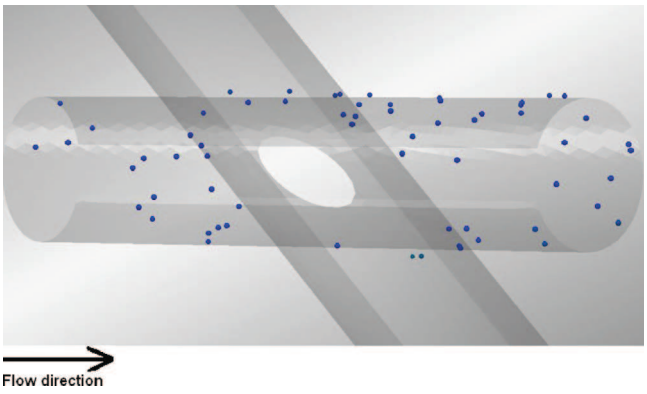

Fig. 12. Deposition around Naltex 51-3 spacer joint.

5. Results and discussion

The number of particles deposited in each Naltex 51 spacer configuration obtained from the simulations is given in Fig. 9. Results display the number of particles deposited as a function of the axial distance from the spacer joint, in the direction of the inlet flow.

For configuration 51-1, Fig. 9 and 10 show there is a preferred deposition location in front of the spacer joint, which does not appear for configuration 51-2 or 51-3 where a constant deposition on the filament parallel to flow regardless of the position of the joint is exhibited. After the joint, 51-1 seems to display a similar deposition pattern as 51-2, Fig. 11, and 51-3, Fig. 12, i.e. a uniform deposition along the filament. For configurations 51-2 and 51-3, no deposition was observed on the transverse filament. This may be because in these configurations, the orientation of the transverse filament relative to the flow increases the velocity gradient around

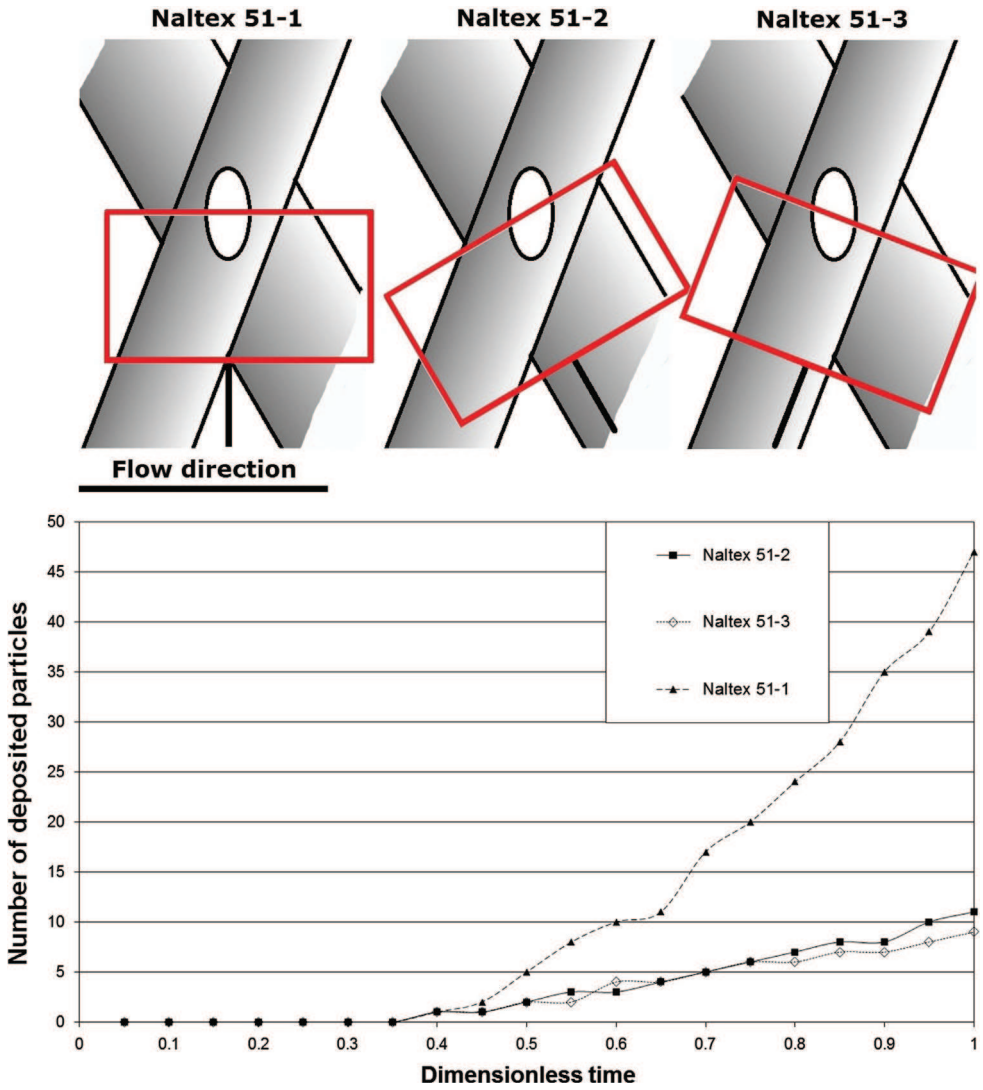

Fig. 13. Evolution with time of deposited particles around spacer join.

it, and therefore also the shear rate, which prevents particles depositing.

Although the spacer types are different, results show the same orientation sensitivity as experimental findings from Neal et al. [18], who studied not the particle deposition on spacers but particle deposition in the gaps between them using square nets of equal sized filaments. Results from the present work are in agreement with Neal's work; both results show that deposition numbers depend on spacer orientation. In the current study, with the filaments arranged symmetrically around the flow direction, deposition occurred particularly at the filament junction, whilst in configurations with filaments parallel to the flow (51-2 and 51-3), deposition occurs across the entire longitudinal filament, parallel to flow. Neal also observed a zone of no deposition at the back of the transverse filament; this does not appear in our simulations. However, in Neal et al.'s work this applied when filaments are at a 90° angle, which is not the case for Naltex 51 spacer configuration used in this work.

Fig. 13 displays the numbers of deposited particles around the spacer joint with respect to simulation time, which has been normalised for comparison purposes as each simulation had a slightly different duration to allow free-flowing particles to escape the domain. The data represents the number of particle-to-wall contacts in the zone displayed in red on the upper part of the figure. It can be seen that after the first wall-to-particle contact in the boxed zone at around 0.3, Naltex 51-1 displays a much greater rate of deposition than the other two spacer geometries. This is attributable to the fact that for the simulations of Naltex 51-2 and 51-3, particles deposit upon impact and stay relatively immobile, due to low velocity gradients. On the other hand, for Naltex 51-1, particles depositing at any location on a spacer are subject to the velocity gradient resulting from the flow area restriction imposed by various filaments and subsequently move and collect at the joint, which makes the deposited particle count around the junction increase significantly.

Vrouwenvelder's [43] experiments (Fig. 14) show deposition patterns similar to our simulation results with initial deposition occurring upstream of the spacer and a preferred deposition location at the spacer joint. This confirms that before growth, propagation and colonisation occur (all of which depend on nutrient availability) the initiation of bio-fouling is comparable to the initial particulate deposition as simulated in the current study.

The observed fouling at the spacer junction in our simulations agrees with some reports regarding microorganism deposition on

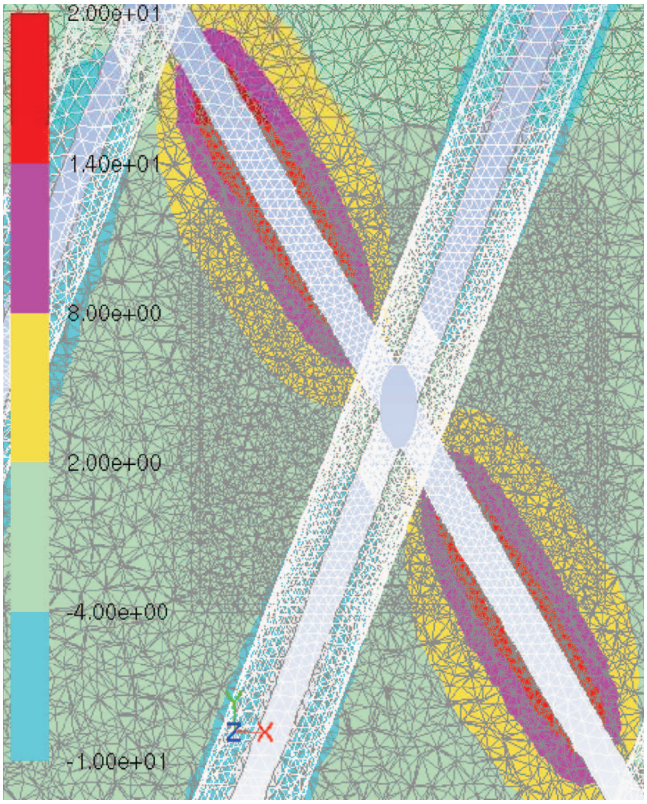

Fig. 15. Shear rate contour around Naltex 51-1 spacer joint. (For interpretation of the references to colour in this figure legend, the reader is referred to the web version of this article.)

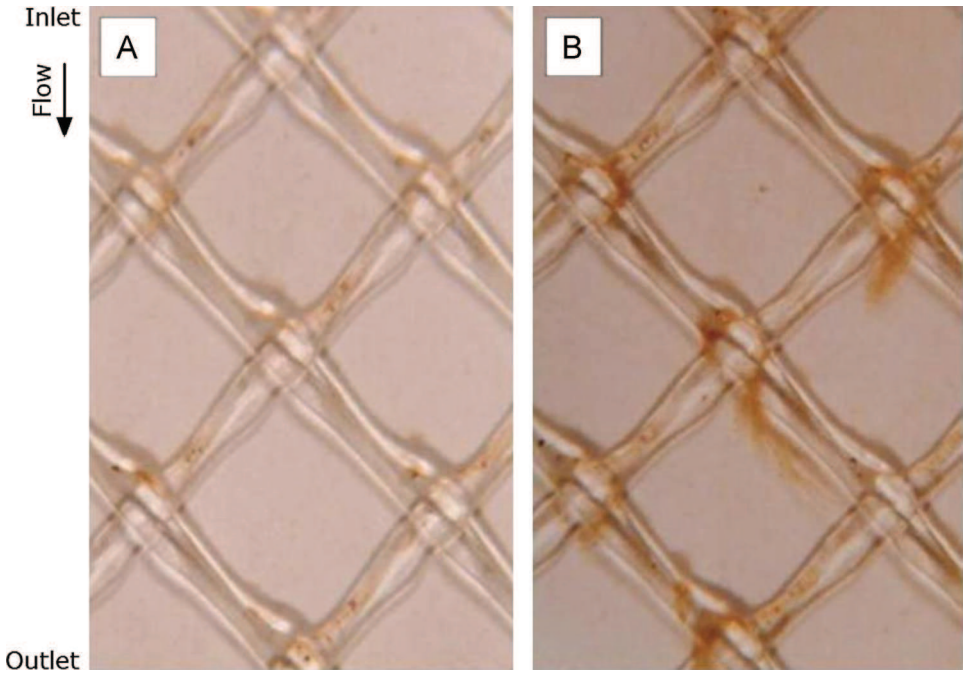

Fig. 14. In-situ visual observations of the feed spacer and membrane without and with nutrient [44].

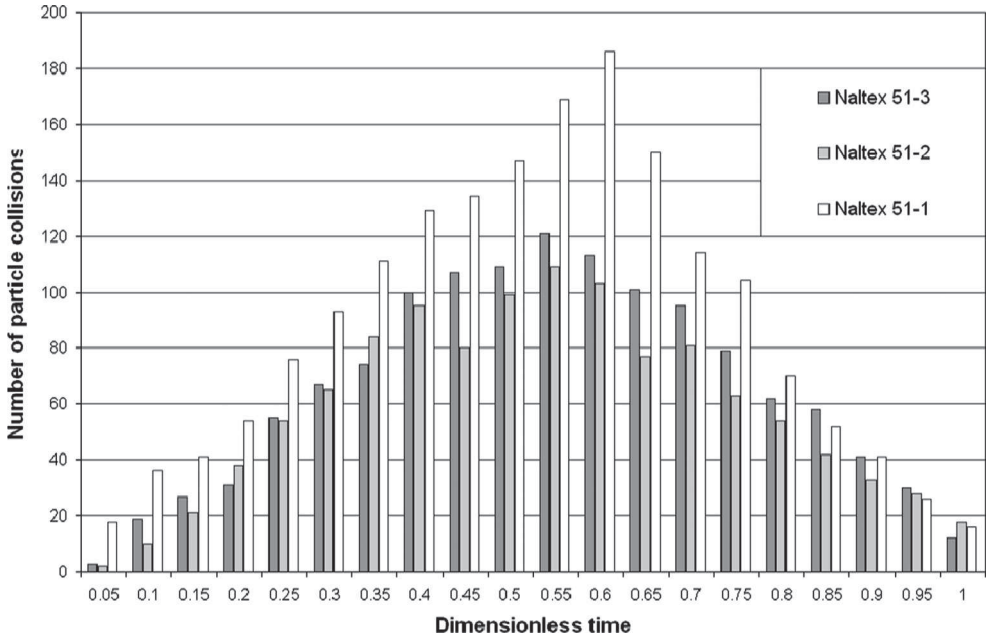

Fig. 16. Comparison of particle collision around spacers.

spacers, which state that the chance of attachment increases for decreasing values of shear stress around the obstacle [44,45]. This would (unsurprisingly) suggest increased deposition at regions of relatively low shear stress. The lowest shear is observed around the filament junction and away from spacer structures in between filament gaps, as shown in Fig. 15.

This means that during initial deposition, adhesion simply occurs where the particles contact the filament, as observed in this work. The increase of biomass due to organism growth that occurs later (shown in Fig. 14B) then develops in areas of lower shear strain (light green region between $-4\ s^{-1}$ and $2\ s^{-1}$ in Fig. 15), toward the gaps between filaments.

Fig. 15 shows that the magnitude of shear stresses is twice higher on the bigger filament, which explains that particle deposition past the junction in Fig. 10 is higher on the smaller filament.

Under the flow, concentration and particle size conditions described in this work, very little particle-to-particle collision (Fig. 16) could be observed. In the spacer feed channel, the ratio of particle volume to total volume was extremely small, mitigating against bulk or surface cluster formation. Fig. 16 shows a linear increase of inter-particle collision up to 0.45 of the total simulation time, which corresponds to the injected particles colliding amongst themselves up until they reach the filament junction. Then numbers drop as the un-deposited particles flow toward the outlet. That suggests that in these simulations, particle-to-particle collisions were not a significant factor for deposition.

6. Further work

This study represents an initial investigation into the use of DEM–CFD to simulate membrane fouling processes; there is much scope for further work. In particular, many different spacer geometries and operating conditions could be simulated. Additionally, the versatility of DEM would allow the modification of particle properties including adhesive properties, and the multiplication of particles so that later bio-fouling process including the establishment and growth of colonies could potentially be simulated.

7. Conclusion

This work reports a study of incipient colloidal fouling around feed channel spacers typical of a spiral wound membrane, demonstrating how deposition morphology changes with spacer filament orientation. Incipient colloidal fouling is found to be similar to incipient bio-fouling. DEM has been used with a one-way CFD coupling, in order to simulate the initial deposition on the commercial membrane spacer Naltex 51. It has been found that the initial deposition pattern appears in regions of low shear stresses, which agrees with reported experiments and simulations. The deposition pattern was found to be dependent on spacer orientation with particle accumulation around the filament junction in Naltex 51-1 being simulated, which also coherent with reported observations.

References

[1] A. Pak, T. Mohammadi, S.M. Hosseinalipour, V. Allahdini, CFD modeling of porous membranes, Desalination 222 (1–3) (2008) 482–488.
[2] C.C. Zimmerer, V. Kottke, Effects of spacer geometry on pressure drop, mass transfer, mixing behavior, and residence time distribution, Desalination 104 (1–2) (1996) 129–134.
[3] I.S. Ngene, R.G.H. Lammertink, M. Wessling, W.G.J. Van der Meer, Particle deposition and biofilm formation on microstructured membranes, J. Memb. Sci. 364 (2010) 43–51.
[4] A.R. Da Costa, A.G. Fane, D.E. Wiley, Spacer characterization and pressure drop modelling in spacer-filled channels for ultrafiltration, J. Memb. Sci. 87 (1–2) (1994) 79–98.
[5] S. Maharudrayya, S. Jayanti, A.P. Deshpande, Pressure losses in laminar flow through serpentine channels in fuel cell stacks, J. Power Sources 138 (2004) 1–13.
[6] F. Li, W. Meindersma, A.B. de Haan, T. Reith, Optimization of commercial net spacers in spiral wound membrane modules, J. Memb. Sci. 208 (1–2) (2002) 289–302.
[7] F. Li, W. Meindersma, A.B. de Haan, T. Reith, Experimental validation of CFD mass transfer simulations in flat channels with non-woven net spacers, J. Memb. Sci. 232 (1–2) (2004) 19–30.
[8] S.K. Karode, A. Kumar, Flow visualization through spacer filled channels by computational fluid dynamics I.: pressure drop and shear rate calculations for flat sheet geometry, J. Memb. Sci. 193 (1) (2001) 69–84.
[9] D.E. Wiley, D.F. Fletcher, Techniques for computational fluid dynamics modelling of flow in membrane channels, J. Memb. Sci. 211 (1) (2003) 127–137.
[10] M. Shakaib, S.M.F. Hasani, M. Mahmood, CFD modeling for flow and mass transfer in spacer-obstructed membrane feed channels, J. Memb. Sci. 326 (2) (2009) 270–284.

[11] M. Shakaib, S.M.F. Hasani, M. Mahmood, Study on the effects of spacer geometry in membrane feed channels using three-dimensional computational flow modeling, J. Memb. Sci. 297 (1–2) (2007) 74–89.
[12] S. Wardeh, H.P. Morvan, CFD simulations of flow and concentration polarization in spacer-filled channels for application to water desalination, Chem. Eng. Res. Des. 86 (10) (2008) 1107–1116.
[13] Z. Cao, D.E. Wiley, A.G. Fane, CFD simulations of net-type turbulence promoters in a narrow channel, J. Memb. Sci. 185 (2) (2001) 157–176.
[14] A.L. Ahmad, K.K. Lau, Impact of different spacer filaments geometries on 2D unsteady hydrodynamics and concentration polarization in spiral wound membrane channel, J. Memb. Sci. 286 (1–2) (2006) 77–92.
[15] A.L. Ahmad, K.K. Lau, M.Z. Abu Bakar, S.R. Abd Shukor, Integrated CFD simulation of concentration polarization in narrow membrane channel, Comput. Chem. Eng. 29 (10) (2005) 2087–2095.
[16] R. Bos, H.C. van der Mei, H.J. Busscher, Physico-chemistry of initial microbial adhesive interactions—its mechanisms and methods for study, FEMS Microbiol. Rev. 23 (2) (1999) 179–230.
[17] A.I. Schäfer, A.G. Fane, T.D. Waite, Nanofiltration: Principles and Application, Elsevier Advanced Technology, Kidlington, Oxford, UK, 2005.
[18] P.R. Neal, H. Li, A.G. Fane, D.E. Wiley, The effect of filament orientation on critical flux and particle deposition in spacer-filled channels, J. Memb. Sci. 214 (2) (2003) 165–178.
[19] J.S. Vrouwenvelder, J.A.M. van Paassen, J.M.C. van Agtmaal, M.C.M. van Loosdrecht, J.C. Kruithof, A critical flux to avoid biofouling of spiral wound nanofiltration and reverse osmosis membranes: fact or fiction? J. Memb. Sci. 326 (1) (2009) 36–44.
[20] J.S. Vrouwenvelder, C. Picioreanu, J.C. Kruithof, M.C.M. van Loosdrecht, Biofouling in spiral wound membrane systems: three-dimensional CFD model based evaluation of experimental data. J. Memb. Sci. 346 (1) (2010) 71–85.
[21] P. Bacchin, P. Aimar, V. Sanchez, Model for colloidal fouling of membranes, AIChE J. 41 (2) (1995) 368–376.
[22] J.W. Costerton, P.S. Stewart, E.P. Greenberg, Bacterial biofilms: a common cause of persistent infections, Science 284 (5418) (1999) 1318–1322.
[23] G. Tchobanoglous, F.L. Burton, H. David Stensel, Wastewater Engineering Treatment and Reuse, 4th Edition/Metcalf and Eddy, Inc. McGraw Hill, New York, 2003.
[24] M.A. van der Hoef, M. Ye, M. van Sint Annaland, A.T. Andrews, S. Sundaresan, J.A.M. Kuipers, B.M. Guy, Multiscale modeling of gas-fluidized beds, Advances in Chemical Engineering, Editor in chief Guy B. Marin, Editorial Board David H. West and Pratim Biswas, Academic Press is an imprint of Elsevier, London, UK, 65–149.
[25] Y.-L. Li, K.-L. Tung, CFD simulation of fluid flow through spacer-filled membrane module: selecting suitable cell types for periodic boundary conditions, Desalination 233 (2008) 351–358.
[26] H. Ma, J. Pedel, P. Fife, W.P. Johnson, Hemispheres-in-cell geometry to predict colloid deposition in porous media, Environ. Sci. Technol. 43 (22) (2009) 8573–8579.
[27] H.A. Lorentz, Abh. Theor. Phys. 1 (1907) 23.
[28] H. Brenner, The slow motion of a sphere through a viscous fluid towards a plane surface, Chem. Eng. Sci. 16 (3–4) (1961) 242–251.
[29] A.V. Nguyen, G.M. Evans, Exact and approximate expressions for resistance coefficients of a colloidal sphere approaching a solid surface at intermediate Reynolds numbers, Appl. Math. Model. 31 (4) (2007) 763–769.
[30] A.J. Goldman, R.G. Cox, H. Brenner, Slow viscous motion of a sphere parallel to a plane wall—I motion through a quiescent fluid, Chem. Eng. Sci. 22 (4) (1967) 637–651.
[31] A.J. Goldman, R.G. Cox, H. Brenner, Slow viscous motion of a sphere parallel to a plane wall—II Couette flow, Chem. Eng. Sci. 22 (4) (1967) 653–660.
[32] A.S. Sangani, G.B. Mo, An O(N) algorithm for Stokes and Laplace interactions of particles, Physics of Fluids 8(1), 1996, 1990–2010.
[33] H. Ounis, G. Ahmadi, J.B. McLaughlin, Brownian diffusion of submicrometer particles in the viscous sublayer, J. Colloid Interface Sci. 143 (1) (1991) 266–277.
[34] C. Tien, B.V. Ramarao, The process of particle deposition in granular media: description and formulation, Granular Filtration of Aerosols and Hydrosols-Butterworth-Heinemann, Oxford 337–403 second edition.
[35] E.J.W.V.a.J.T.G. Overbeek, Theory of the Stability of Lyophobic Colloids, 1948.
[36] G. Duursma, M. Crapper, S. Whitelaw, W.S. Wong, DEM–CFD modelling of voidage and heat transfer in fluidized beds, in: Proceedings of 8th World Congress on Chemical Engineering, Montreal, Canada, 2009.
[37] J. Gregory, Approximate expressions for retarded van der waals interaction, J. Colloid Interface Sci. 83 (1) (1981) 138–145.
[38] V.A. Naumov, Influence of Saffman's lift force on the motion of a particle in a Couette layer, J. Eng. Phys. Thermophys. 68 (5) (1995) 683–686.
[39] H.K. Versteeg, W. Malalasekera, An Introduction to Computational Fluid Dynamics, The finite Volume Method, Longman Scientific and Technical, Harlow, Essex, UK, 1995.
[40] M. Rahimi, S.S. Madaeni, K. Abbasi, CFD modeling of permeate flux in cross-flow microfiltration membrane, J. Memb. Sci. 255 (1–2) (2005) 23–31.
[41] P.A. Cundall, Formulation of a three-dimensional distinct element model—part I. a scheme to detect and represent contacts in a system composed of many polyhedral blocks, Int. J. Rock Mech. Min. Sci. Geomech. Abstr. 25 (3) (1988) 107–116.
[42] R. Rajagopalan, C. Tien, Trajectory analysis of deep-bed filtration with the sphere-in-cell porous media model, AIChE J. 22 (3) (1976) 523–533.
[43] J.S. Vrouwenvelder, D.A. Graf von der Schulenburg, J.C. Kruithof, M.L. Johns, M.C.M. van Loosdrecht, Biofouling of spiral-wound nanofiltration and reverse osmosis membranes: a feed spacer problem, Water Res. 43 (3) (2009) 583–594.
[44] J.S. Knutsen, R.H. Davis, Deposition of foulant particles during tangential flow filtration, J. Memb. Sci. 271 (1–2) (2006) 101–113.
[45] M. Rahimi, S.S. Madaeni, M. Abolhasani, A.A. Alsairafi, CFD and experimental studies of fouling of a microfiltration membrane, Chem. Eng. Processing: Process Intensification 48 (9) (2009) 1405–1413.